UC Irvine

UC Irvine Electronic Theses and Dissertations

Title

Dynamic Finite Element Analysis of Quantitative Percussion Diagnostics for Microgap Defects Detection in Teeth

Permalink

https://escholarship.org/uc/item/05m40375

Author

Shen, Jie

Publication Date

2023

Copyright Information

Peer reviewed|Thesis/dissertation

UNIVERSITY OF CALIFORNIA,
IRVINE

Dynamic Finite Element Analysis of Quantitative Percussion Diagnostics for Microgap Defects
Detection in Teeth

DISSERTATION

Submitted in partial satisfaction of the requirements
for the degree of

DOCTOR OF PHILOSOPHY

in Materials Science and Engineering

by

Jie Shen

Dissertation Committee:
Professor James C. Earthman, Chair
Professor Emeritus William C. Tang
Professor Lorenzo Valdevit

2023

DEDICATION

I dedicate this dissertation to my wife, my family, my cat, and my dog, who have supported me through every step of this academic journey. Their love, companionship and encouragement are the driving force behind my completion of my PhD program.

To My Wife,

Your faith and your love have supported me through the most challenging times throughout my PhD program. I appreciate your patience and sacrifices that allows me to dedicate my time to my research. I also appreciate your scientific contribution to fulfill QPD clinical results of teeth for my research and future publications.

To My Cat Garfield and My Dog Terra,

Your enthusiasm and optimism for life have provided solace during my difficult and stressed time. I appreciate your companionship and your unspoken encouragement. Your unconditional love and enjoyable greeting provided me needed breaks from the intense academia vibe.

To My Family,

Your financial support from the earliest days of my academic journey in the United States to this moment is the foundation for me to chase my dreams. Your encouragement and advice have guided me to overcome challenges in my life. The unforgettable love from the family has supported me and reminded me of the significance and importance of my academic journey. I want to make my PhD accomplishment as a testament to the evidence of love, support, companionship, and dedication in my journey of personal growth and academic progress.

TABLE OF CONTENTS

Page

LIST OF FIGURES

LIST OF TABLES

ACKNOWLEDGMENTS

VITA

Jie Shen

Education

Ph.D. in Materials Science and Engineering, University of California, Irvine	2023
M.S. in Materials Science and Engineering, University of California, Irvine	2019
B.S. in Materials Science Engineering, University of California, Irvine	2018

Academic Experience

Graduate Student Researcher   2018 - 2023
Professor James Earthman's Group, University of California, Irvine

Teaching Assistant   2021 - 2022
Undergraduate Senior Design, Biomedical Engineering and Materials Science
University of California, Irvine

Lab Researcher
Professor Martha Mecartney, University of California, Irvine   2016 - 2018

Presentation

University of California Systemwide Bioengineering Symposium	2021
The Mineral, Metals & Materials Society (TMS) 2022 Annual Meeting	2022
Materials Research Society (MRS) 2022 Annual Meeting	2022
The Mineral, Metals & Materials Society (TMS) 2023 Annual Meeting	2023

Industry Experience

Field Service Engineer Intern   2023
Carl Zeiss Microscopy, LLC

Publication

Mapar, A., Taheri-Nassaj, N., Shen, J., Komari, O., Sheets, C. G., & Earthman, J. C. (2022). Finite Element Study of Periodontal Ligament Properties for a Maxillary Central Incisor and a Mandibular Second Molar Under Percussion Conditions. *Journal of Medical and Biological Engineering*, *42*(5), 681–691. https://doi.org/10.1007/s40846-022-00724-5

ABSTRACT OF THE DISSERTATION

Dynamic Finite Element Analysis of Quantitative Percussion Diagnostics for Microgap Defects Detection in Teeth

by

Jie Shen

Doctor of Philosophy in Materials Science and Engineering

University of California, Irvine, 2023

Professor James C. Earthman, Chair

Microgap defects (MGDs), including cracks and fractures in teeth, can lead to irreversible damage, potentially leading to tooth extraction. Early detection of MGDs is very important in avoiding permanent defects through appropriate treatments. Quantitative percussion diagnostics (QPD) is a non-destructive method that has been shown to detect MGDs in teeth. The goal of is the present research was to use finite element analysis (FEA) models to better understand the behavior of various MGDs in different tooth geometries and the patterns of QPD force responses generated for teeth with MGDs. This present research analyzed the shape of force versus time plots of QPD results and how they are affected by different MGD types and conditions in both single rooted premolars and double rooted molars.

FEA models were constructed based on scanned, converted, and meshed 3D tooth geometries, and by implementing various MGD types, such as vertical cracks, oblique cracks, apical root cracks, damaged PDL and PDL lesions. FEA models were also exercised with different MGD conditions, including crack lengths and gap spaces. A percussion rod contains a force sensor, which was also included in all FEA models to simulate the clinical QPD measurements, capturing percussion force as a function of time. The simulated QPD measurements are analyzed, validated, and discussed in the present work.

The results of FEA models are consistent with observed in vivo clinical results and confirm the capability of QPD for detecting MGDs in teeth. These FEA results not only provide insights into the distinctive characteristics of results corresponding to various MGD types and conditions but also explain the reasons contributing to shape changes in percussion force versus time results. Furthermore, a novel approach involving 3D printed replica teeth was also developed to address the limitation of obtaining in vivo conformational data. This innovative method enhances the foundation of the study by using replica teeth to support the understanding gained from FEA simulations.

INTRODUCTION AND BACKGROUND

Tooth Anatomy
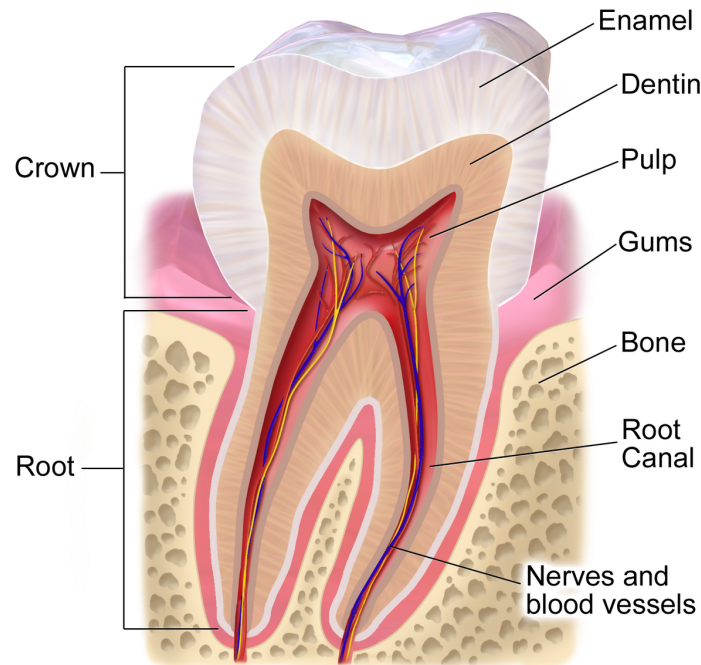
Figure 1: Tooth anatomy. [1]

Understanding tooth anatomy is important for comprehending the basics of this research. This research study revolves the application of Finite Element Analysis (FEA) to identify cracks and defects in human teeth using Quantitative Percussion Diagnostics (QPD). The tooth anatomy provides fundamental insights about tooth components and general geometries of various tooth structures. As shown in Figure 1, a human tooth contains several key components, including enamel, dentin, pulp chamber embedded within the dentin, surrounding gum tissues, bone, root canal and nerves. Enamel is a very tough material, acting as protective outer layer, protecting the tooth during the mechanical process of biting and grinding. Dentin is the main core structure of the tooth. There is pulp chamber and root canal inside the dentin structure to allow the blood circulation and accommodates nerves. The bone is the foundation support of the tooth, ensuring the tooth stability. The thin layer of gum tissue, also known as periodontal ligament (PDL),

1

surrounds the tooth in between dentin and bone. In this research, various tooth models are analyzed, and main components of the tooth are created and included in the FEA simulations. Main components of tooth include enamel, dentin with pulp chamber, bone and PDL.

One can also differentiate the tooth as two sections. The part that is visible in the mouth is called crown, and the portion below the gum tissues is referred to as the root. In this research, cracks and defects were modeled in both crown and root sections. For instance, it was common to find vertical and oblique cracks in the crown because these cracks typically originate from the top occlusal surface. On the other hand, apical root cracks are typically in the root section because they originate from the bottom of the dentin apex region. There are various types of cracks and defects, which will be discussed in the following section.

Current Diagnostic Methods

Current diagnostic tools for detecting cracks or fractures in human teeth include visual inspection, transillumination, optical microscopic examination, micro-computed tomography (Micro-CT) and dye penetration. Figure 2 shows how a cracked tooth is examined during clinical procedures. First, the dentist visually inspects the tooth. They may discover an unclear crack indication on the right side of the tooth as shown by the yellow arrow in Figure 2 (a). Next, they use transillumination method, a method that uses the blockage of light transmission, indicates a significant crack on the left side of the tooth where the red arrow points to shown in Figure 2 (b). To examine the cracks in this tooth further, dentist uses the micro-CT, which provides a detailed view of the crack shown in the Figure 2 (c). Another common method is dye penetration, where a dye is used to enter and fill the crack gaps. However, all these diagnostic methods rely on visibility to diagnose cracks, and they all have their limitations.

For instance, even though transillumination is able to indicate cracks, but according to an in vitro study, it shows only 40% agreement between the transillumination findings and disassembly results. [2] It is also limited in its ability to detect cracks located beneath the bone. Optical microscopic examination can magnify the tooth's surface, but it is limited to the maximum magnification about 20 times and depends on good lighting conditions. This is typically used as a complement to transillumination. Micro-CT has constraints related to resolution and radiation. The special resolution is about 40 μm in vitro. [2] In vivo oral setting, where patient safety is a concern under radiation, it is not very practical, so micro-CT is better suited for studies involving extracted teeth. Dye penetration method can lead to false crack detection because dye can easily fill into grooves and surface irregularities on the tooth's occlusal surface. Therefore, given these limitations in current diagnostic methods, it is essential to explore new ways to detect cracks that do not solely rely on what is visible.
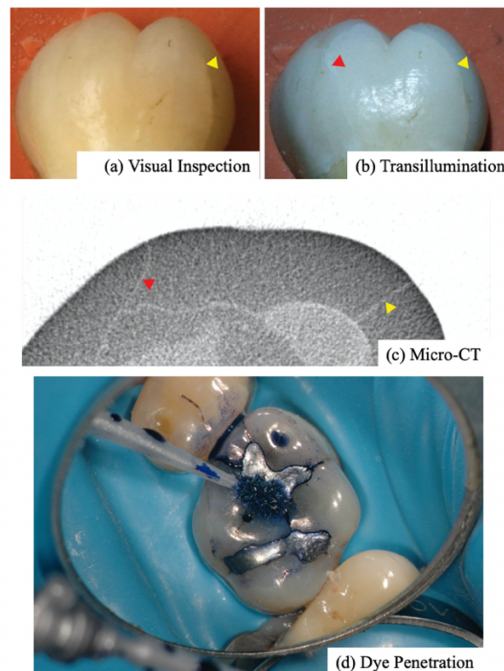
Figure 2: (a) Visual inspection, (b) Transillumination, (c) Micro-CT, (d) Dye penetration. [3], [4]

QPD Description

In 2002, a tool known as the Periometer® (Perimetrics, LLC, Los Angeles, CA) was introduced and is shown in Figure 4. Overtime, it has been demonstrated that this quantitative percussion diagnostic tool can significantly reduce risks by periodically assessing the mechanical stability of human teeth and implants, identifying cracks and defects, and the mechanical integrity of the underlying bone. [2], [5]–[8] The QPD device employs a handheld probe housing a percussion rod with an embedded force sensor. This probe gently taps on the tooth while measuring the resultant force during the percussion over time. Just before impact, a stainless-steel rod in the probe which contains a force sensor, is accelerated to a predetermined velocity. [2], [5], [7] In dentistry, percussion diagnosis has been In use for many years as it is shown in Figure 3. Traditionally, dentists employed the handle of the dental mirror to tap teeth and detect sensitivity, mobility, auditory sound differentials. This helped dentist determine cracks based on their experience. However, this traditional percussion diagnosis using dental mirror lacks quantifiability.
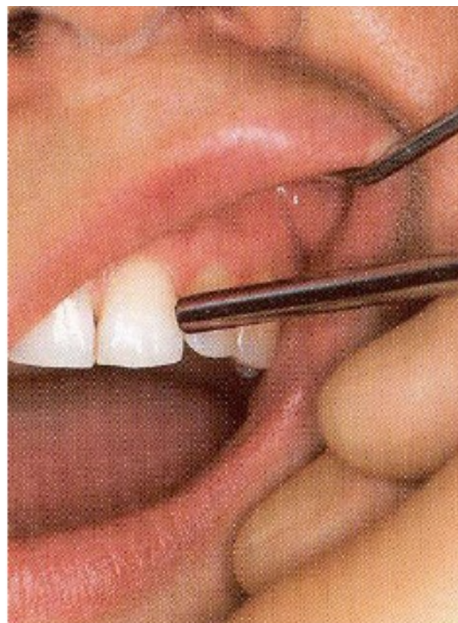
Figure 3: Percussion diagnosis using handle of dental mirror. [9]

The objective and goal of the present study is to create and develop finite element models that simulate the interaction between the QPD device and human teeth, allowing better understanding of how the QPD detects oblique and vertical cracks in human natural teeth. In addition, the goal is to design, build and execute finite element models to simulate quantitative percussion diagnostics (QPD), in order to enhance our understanding of how QPD identifies oblique and vertical cracks in natural teeth.

Figure 4: Percussion probe for the Periometer® (Perimetrics, LLC, Los Angeles, CA).

Teeth can experience fatigue and failure due to repeated dynamic loading. This can lead to the formation and growth of cracks that are often challenging to detect. During clinical assessments, detecting a crack is occasionally possible, especially when dealing with advanced defects. Signs may include the change in color, or the presence of a shadow in the area of the fracture. Various nondestructive methods have been explored for crack detection, including transillumination, magnification, dye penetrants, radiographs, occluding tests, and ultrasonography. Previous research has demonstrated that the QPD outperforms these methods when it comes to identifying cracks and fractures in natural teeth. [2], [7] In fact, the QPD demonstrated exceptional accuracy in identifying cracks and fractures when compared to

observations made during destructive tooth disassembly procedures performed under an optical microscope. The agreement between the QPD and disassembly results was as high as 98%. In contrast, transillumination was only able to detect 42 % of the cracks that were observed under the microscope during destructive tooth disassembly. QPD's proficiency in crack detection can be attributed to its ability to measure the percussion loading as a function of time. In intact teeth, this measurement shows a nearly symmetric single peak. However, when a crack is present, the response shifts to multiple peaks. This distinctive pattern makes the QPD highly effective at identifying the presence of cracks in teeth. [2]

FEA Description

Biomedical research has widely embraced computational EM those as they offer a cost effective and time effective alternative to live experiments and clinical trials. One such computational tool is Finite Element Analysis (FEA), which has been used to simulate the actual physical processes of real-world problems using numerical techniques.

FEA consists of three main steps. The first step is preprocessing. [10] In this step, a model to be simulated is constructed. In this research, this model is assembly of the tooth model and percussion rod system, including major tooth components of enamel, dentin with the pulp chamber and root canal, bone and PDL according to tooth anatomy in Figure 1. Tooth models are created as CAD in SOLIDWORKS. Procedures are described in detail in later section of modeling method. After the CAD model is created, the model geometry is divided into a finite number of discrete subregions called elements, and each element is connected at discrete points called nodes. Modern commercial codes employ user-friendly graphical preprocessors to assist users. Commercial software like MSC provides user-friendly tools to assist in this stage.

The second step of FEA is analysis where the dataset prepared by the preprocessor is applied as input to the FEA code itself. [10] In this step, the MSC software solves linear or nonlinear equations to determine various parameters like force, displacement, velocity, contact interaction status, stress and strain data. The advantage of FEA is that many problems can be addressed in the same commercial software code. The time required for this FEA analysis depends on the complexity of the model. Normally, the present FEA simulations would finish within 24 hours.

The third step of the FEA is postprocessing. [10] After the FEA simulation is finished, the MSC software can present all the recorded data. For instance, the postprocessor is able to use graphical displays to aid in visualization of contact interaction status and show user the touching and glue interaction between contact bodies. This is especially important when analyzing cracked teeth, as crack faces often come into contact during percussion loading. Another important postprocessing result is percussion resultant force and relative velocity between crack surfaces. The percussion resultant force and relative velocity are plotted and analyzed in the following chapter.

Even though the FEA simulation tool is great for analyzing different tooth models, FEA still has some disadvantages. FEA do not necessary reveal how the QPD test data are influenced by important problem variables such as material properties and geometrical features. [10] For example, material properties for each tooth components are not always well defined in the literature, because they are organic and vary among patients. The same idea applies to tooth geometries in that one person can have slightly different tooth geometry than another. Another disadvantage of FEA is that errors in input data can produce substantially incorrect results. [10] For instance, input data including touching tolerance or damage zone implementation can provide

very different results. To mitigate these limitations, different input data can be conducted in numerous simulations, however. This strategy will be described and analyzed in the following chapter.

Despite its limitations, there are many critical advantages using FEA. The first advantage is easy modeling. FEA allows easier modeling for complex geometries and irregular shapes. In this study, it is easy to model different thicknesses of the PDL to simulate different PDL health. It is easy to implement different crack length and crack gap size to simulate different crack level. The second advantage is good adaptability. FEA allows specific accuracy to decrease the time and budget for physical prototypes in the product design processes. In this study, we have limitations to acquire actual experimental sample of cracked tooth from patients. Even though we are able to find cracked tooth in patients, it is hard to determine the corresponding crack conditions based on current diagnostic methods. Therefore, it saves a lot of time and money to research in cracked tooth using FEA. The third advantage is good accuracy. Modeling by hand or 3D printing and then doing the QPD testing can be practical but lack of accuracy, and the computational FEA can solve the same problem with a high degree of accuracy. In this research, we utilized 3D printing technology to model cracked teeth and intact teeth, but the accuracy still needs to be validated by FEA simulations. The fourth advantage is visualization. FEA is a great tool to help researchers visualize details of FEA procedures. In the present research, it is easy to visualize the crack surface closures under percussion loading, and it is easy to visualize the displacement of the percussion rod and the tooth. This has greatly help me understand the theory and tooth behaviors underlying the FEA result.

Many researchers have utilized FEA simulations to study human teeth. For example, MinSeock Seo and his collogues study maxillary central incisors restored with various post and

core applications using FEA. They can analyze stress distribution on the rigidity post core system in the tooth. [11] Another example is that Roberto Elias Campos studies fracture load and fracture pattern of ceramic crowns using FEA. It can implement occlusal loading points and occlusal force in the FEA model and find fracture origination. [12] In addition, Ioana-Andreea Sioustis studies mandibular anterior teeth with healthy but reduced periodontium. He found the stress in bone, PDL, teeth and displacement in the bone by using FEA. [13]

Furthermore, many other researchers utilize FEA to study mechanical structure related problems in human teeth. The present five-year research is using FEA to simulate the QPD tests on different kinds of cracks and defects. By utilizing FEA tool, it can reduce the number of clinical experiments, which means it is not required to find patients with different tooth cracks and run the QPD. Previous studies have conducted finite element analysis (FEA) to simulate and study the mechanical responses of mandibular second molars and maxillary central incisors under percussion loading in order to analyze the mechanical response of the tooth under percussion conditions consistent with the QPD. [14] The results of those studies validate the results of the FEA models with the clinical QPD experimental data with compatible measurements of the force as a function of time. The previous studies also established the guidelines for FEA modeling the cracked teeth under the QPD conditions. For instance, it was discovered that implementing Rayleigh damping is important for the periodontal ligament (PDL) to have a significant effect on the predicted percussion forces. [14] It was also discovered the damping partitions for PDL, bone, and dentin based on their relative values of volume fraction and elastic modulus for a Reuss model of the tooth-bond complex, and these damping partitions are detailed described in the section of modeling methods. Besides the material properties for PDL, some other important material properties are also implemented in FEA simulations, including elastic moduli, Poisson's ratios,

and densities for enamel, dentin, PDL, cortical bone, and stainless steel. Reported values of these important material properties have been exercised in the FEA models. [15]–[17]

Problems and Goals

Figure 5 displays QPD results in the form of normalized energy return plot for an intact tooth. The data represent the outcomes of 10 percussion responses recorded during the QPD test. The horizontal axis represents time in milliseconds, while the vertical axis displays normalized energy return, a unitless measure normalized by percussion resultant force, which is measured in Newtons. It is worth noting that the results are typically presented as force versus time, rather than normalized energy return versus time. However, the crucial aspect of interest is in the shape of the curve, and this shape remains identical between two presentations. The plot shows only one bell shaped curve in Figure 5, and this curve represents how an intact tooth responds to percussion loading. This consistent bell-shaped curve serves as a reference for any intact teeth without cracks or defects.
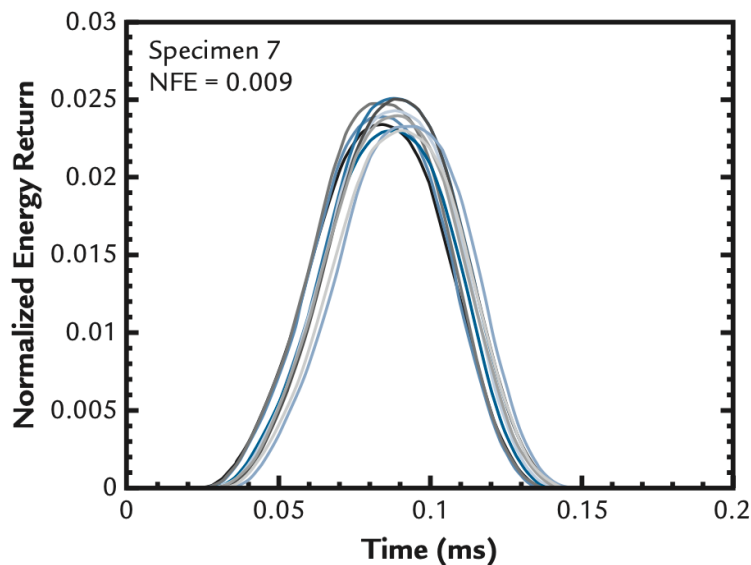
Figure 5: Normalized energy return results for intact tooth. Data corresponding to 10 percussion responses are shown. [2]

On the other hand, when a tooth has crack in it, the QPD result displayed in Figure 6 (a) reveal multiple peaks, notably a second peak following the first peak. The Figure 6 (a) represents the QPD findings for a severely cracked tooth before treatment or restoration. In contrast, the Figure 6 (b) illustrates the QPD results for the same cracked tooth after restoration. Interestingly, the curve's shape begins to change, resembling the single bell shape seen in intact QPD results. The second peak is no longer as closely matched to the first peak. In addition, the maximum value of the normalized energy return is higher after treatment than before treatment. This finding aligns with findings in FEA models of cracked teeth, and it will be discussed in later chapters.
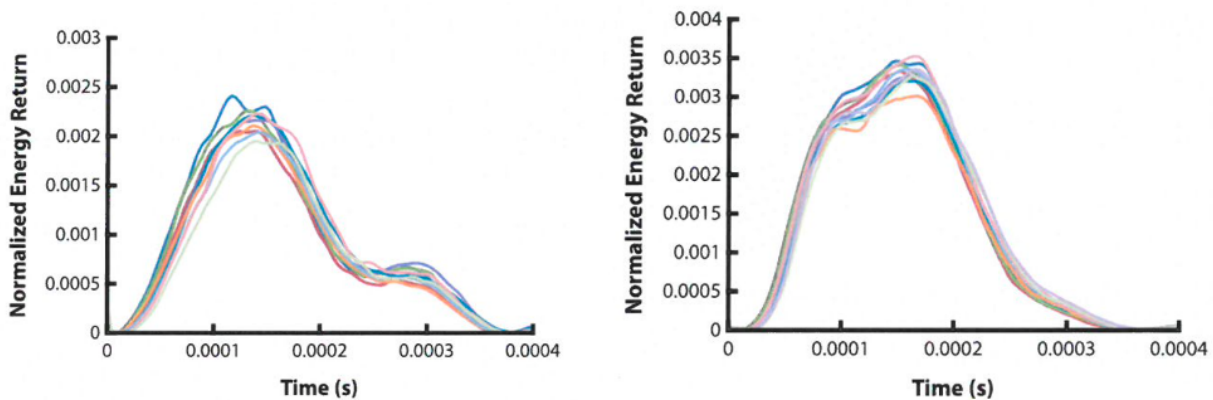
Figure 6: (a) Normalized energy return results for cracked tooth (before treatment). (b) Normalized energy return results for cracked tooth (after treatment). [2]

Based on above clinical QPD data comparison, several critical questions arise. Why does the normalized energy return versus time plot show the bell-shaped curve when the tooth does not contain cracks, and why does the plot exhibit multiple peaks with lower maximum energy return when the tooth contains cracks. What is the underlying theory behind those plots, and what is going on during the QPD percussion loading upon the tooth? How does the tooth respond to the loading, both with and without cracks in teeth? What insights can a dentist gathered from these plots and how can they determine the nature of cracks or defects within a tooth? How can a dentist

predict factors like crack length, location and orientation in the tooth based on the plot's appearance? These are complex questions behind these plots and the goal of this research is using FEA models and simulations to understand the complexity and patterns of force – time plots generated by the QPD, mainly how these peaks are formed and how they are different among various crack types. Ultimately, the goal is to gain a deeper comprehension of the conditions associated with teeth defects.

Research Topics

Cracked and fractured teeth can result from various factors like teeth grinding, intense biting, gum disease and fatigue. These cracks may only have subtle symptoms or no symptoms, if any, such as occasional discomfort and intermittent pain when eating or exposure to temperature extremes. Thus, these cracks may go unnoticed until they progress to the point where the tooth requires extraction. Therefore, it is important to identify cracks in teeth at early stage, even when patients do not have any symptoms. This dissertation will explore some common types of tooth cracks and defects, utilizing the QPD alongside FEA simulations to detect these issues. Each chapter within this dissertation will delve into specific cracks or defects topic.

One prevalent condition in clinical practice is tooth cracks and fractures occurring along the tooth's vertical plane that, which aligns with the long axis of the crown and root. These are often referred to as "longitudinal fracture" due to their tendency to extend vertically over time and distance. The review paper by Eric explained some causes of the vertical cracks, apical root crack, and provides clinical cracked tooth images to help understanding crack conditions and common crack propagations in the tooth. [18] Author stated that vertical crack and fracture pose a particular challenge because, in many cases, tooth extraction becomes necessary as the crack progresses over time. These vertical cracks are typically caused by occlusal forces and dental procedures. Author

mentioned some important considerations regarding the vertical crack formation. They are challenging to visualize and often remain undetectable until they grow and expand. [18] The progression of a vertical crack is illustrated in Figure 7. The direction of the vertical crack is usually mesial-distal on the crown. The crack is initiated at the centered on the top of the crown but the depth on the root varies. Overtime, the vertical crack extends, reaching the enamel dentin junction as shown in the middle figure. It can then propagate further into the root, potentially culminating in the final vertical fracture toward the facial or lingual root surface. Occasionally, cracks initiate from the crown of the tooth but do not follow a perfectly vertical path toward the tooth's root. Instead, they may propagate toward the side of the crown, leading to what is often termed as "oblique crack". Oblique cracks tend to result in crown fracture because the crack propagation pathway is shorter compared to vertical crack. The oblique crack example is shown in Figure 8. Therefore, the first chapter of this dissertation focuses on vertical crack and oblique cracks in the maxillary second bicuspid. Models of the maxillary second bicuspid, featuring both vertical cracks and oblique cracks with two crack lengths are simulated for the QPD test using FEA. The results are then compared to an actual clinical extracted maxillary second bicuspid that exhibited a vertical crack originating from the crown, extending crack length approximately 7 mm below the enamel-dentin junction, similar to the middle figure in Figure 7. The oblique crack FEA models are likewise tested, with the crack initiating in the same crown region and extending toward the side of the tooth. Both of vertical and oblique crack models are in mesial distal orientation, and they align with the characteristics of the real cracked and extracted bicuspid. Further details will be provided in Chapter 1.

Figure 7: Vertical crack progression to split tooth. [18]

Figure 8: Example of an oblique crack.

The second chapter of this dissertation extends the investigation of vertical cracks, this time focusing on a different tooth model known as the mandibular second molar. In Chapter 2, we explore vertical crack conditions, gaining insights from an actual clinically extracted mandibular

second molar containing a vertical crack illustrated in Figure 9. Then, the study proceeds to validate the QPD results of the extracted tooth by comparing them with those obtained from FEA simulations of a cracked tooth. Chapter 2 provides a more in-depth exploration of these aspects.

Figure 9: Extracted mandibular second molar with a vertical crack.

As a vertical crack progresses and extends below the level of the PDL, it provides a pathway for various irritants to infiltrate the crack gap space and adjacent canals. This includes the presence of bacteria, sealer partials, and amorphous materials that tend to accumulate around the crack. Consequently, the PDL tissues adjacent to the long vertical crack experience chronic inflammation. [18] If this inflammation persists over an extended period, it can result in servers damage to the PDL, exacerbating the condition associated with the long vertical crack. In this chapter, I aim to explore this specific scenario shown in Figure 10 where a damaged PDL coexists with FEA models of long vertical crack, particularly when the vertical crack extends deep enough

to reach below the PDL level. Chapter 3 will demonstrate the simulation of this damaged PDL condition, examine the impact of a lower modulus of the PDL.

Figure 10: The proximal view of the extracted tooth shows a vertical crack that extends deeply to the root with infiltration of granulomatous tissue. [18]

Vertical cracks in mandibular second molar are future exploited using replica 3D printed tooth models. These replica tooth models, crafted through 3D printing, serve as realistic simulations of actual teeth and are capable of undergoing the QPD tests. This approach allows for the easy modeling and 3D printing of various crack lengths and crack gap sizes. However, it is important to point out that there are certain limitations associated with 3D Printing technology. A comprehensive discussion of this replica teeth research can be found in Chapter 4.

Chapter 5 focuses on FEA simulations involving molar teeth with apical root cracks, also known as vertical root fractures (VRFs), which typically originate at the root of the tooth and extend towards the tooth's upper portion. As shown in Figure 11, these cracks follow a facto-lingual direction on the root and are often the result of condensation forces during root-filled procedures or forces from the placement of posts. [18] VRFs are particularly challenging to diagnose in a dental office due to their origination within the root. Researching in VRFs through FEA simulations provides a practical approach, detailed research is presented in Chapter 5.
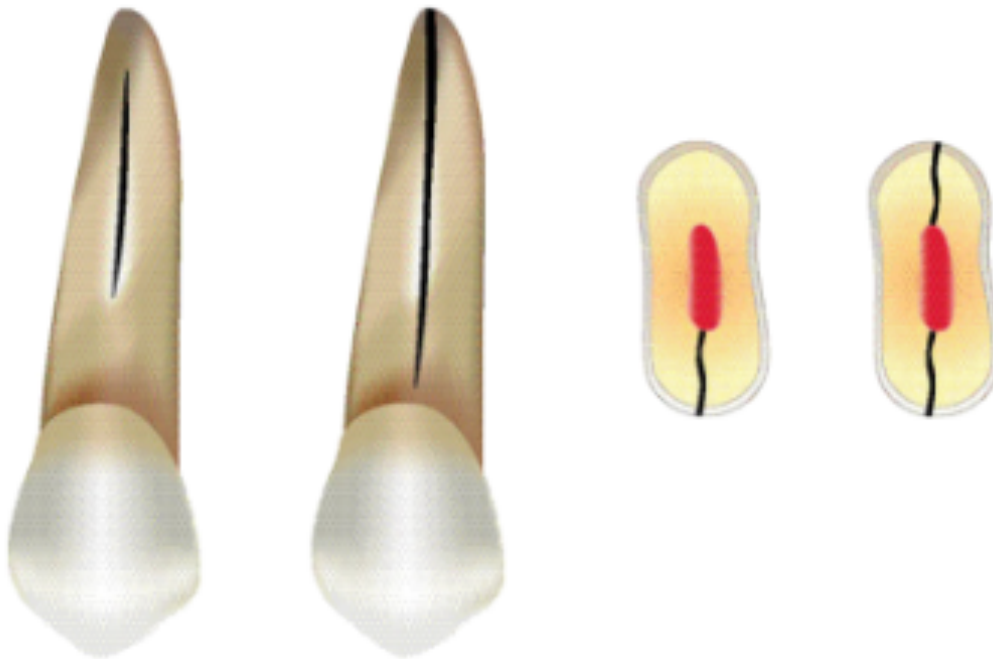
Figure 11: Apical root crack also known as vertical root crack. [18]

In Chapter 6, the research topic is FEA simulations involving a damaged PDL even when the tooth itself remains structurally intact. This clinical scenario arises due to periodontal and endodontic lesions. [19] Figure 12 shows an X-ray image which discovering an example of clinical condition of endodontic lesions on the distal side of the molar tooth. In this X-ray image, the left side of the tooth's root exhibits missing PDL and along with bone loss. Therefore, Chapter 6 delves

into the study of damaged PDL, particularly focusing on J-shape PDL damage and PDL lesions occurring at the intact tooth. Detailed insights into this topic can be found in Chapter 6.
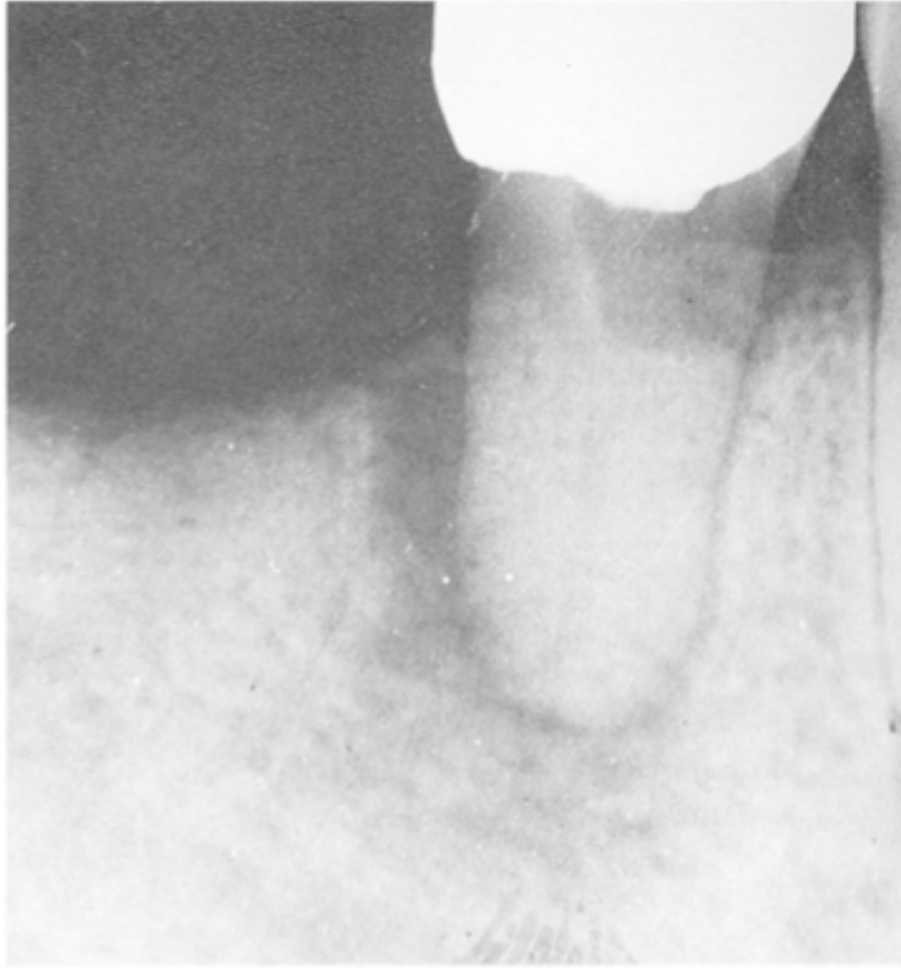
Figure 12: Radiographic appearance of the endodontic lesion. [19]

Modeling Methods

The present finite element model represents the structure of a single tooth complex, consisting of multiple layers, an external layer, known as enamel, possesses a high degree of mineralization and lacks collagen. Within the tooth's internal region, known as dentin, is a tougher substance composed of living cells containing a hard mineral substance. Situated within the dentin is the pulp chamber, a region containing blood vessels and nerves. There is tissue called PDL fitting in between dentin and bone.

Finite element analysis (FEA) allows for the simulation of the QPD testing through processes like modeling, meshing, and simulating. This ultimately generates mechanical response data for teeth with cracks under percussion loading conditions. First, SOLIDWORKS (Dassault Systèmes SolidWorks Corp., Waltham, MA) is used to construct the 3D model of a particular tooth's geometry. This is based on computer tomography data, which include tooth geometries and sizes provided by eHuman, Inc. (Fremont, CA). In all tooth models, there are a six SOLIDWORKS components in one model: enamel, dentin with empty pulp chamber, periodontal ligament (PDL), bone, and percussion rod. The PDL is not only strongly binds the tooth root to the supporting bone but also absorbs occlusal loads and distributes the resulting stress over the hard tissues. [20] Bone can have two distinct forms, cortical bone, and trabecular bone. However, the present models only contain the cortical bone since that bone type provides the greatest amount of support for teeth. [5]

CAD Modeling

SOLIDWORKS serves as the software employed for crafting the CAD models of teeth for finite element analysis. It boasts several valuable features, including surface lofts, boundary surfaces, filled surfaces, combination, deformation, and trim. The following are some general steps that was used to create teeth CAD models.

1. Importing eHuman file into SOLIDWORKS

   The initial step involves importing eHuman file into SOLIDWORKS. Opt for the "dxf" eHuman file format and open it in SOLIDWORKS, Choose "import to a new part as 3D curves or model". Ensure the model is imported in inches and select layers bearing the name "object" exclusively. Following the import, verify all components and assess the tooth's size using the measuring tool. This action initializes the creation of tooth sketches within SOLIDWORKS.

2. Creating Enamel and Lower Dentin

Each tooth model contains five major parts: enamel, dentin, pulp chamber, PDL, and bone. Since the eHuman file only provides sketches for the bottom part of the dentin, so generating the top part of the dentin becomes a supplemental step. Thus, the second step involves creating the enamel and lower part of the dentin. Surfaces are crafted by features like the surface lost to connect the original spline lines. It is important to consider the sequence, beginning from top to bottom or vice versa, and select closed spline lines as profiles. For guidance, employ open loop sketch lines if available. The selection manager can be a valuable tool. If the eHuman file lacks guidelines, consider using a 3D sketch to create open loop guidelines. Ensure these guidelines connect with each closed loop splines used for surface loft. To seal the very bottom of the dentin, often use the "fill surface" feature. When comparing options like contact, tangent and curvature, it is typically found that the curvature option works best in terms of the shape of the tooth's surface. When surface lofts are complete, various solution can be applied if issues arise. These include reducing the number of spine lines in the profile section or using the boundary surface feature. Sometimes, redrawing the spline line sketches may be necessary. Once all surface lofts for lower dentin and enamel are created, use the knit feature to merge them into a solid, resulting in the completion of the enamel and lower dentin.

3. Creating the Entire Dentin Body:

The third step is complete in the entire dentin body. Since the eHuman file does not come with the upper part of the dentin's sketch lines, the deform feature is used to generate this section. Begin by combining enamel and lower dentin into a single entity to start deformation. Use the deform command, place the deform pinpoint on the upper enamel,

regulate the deform distance and region, and designate the fixed body as the lower dentin portion, as the upper dentin section is created by deforming the enamel. It is advisable to consult dental literature to acquire a reference for the dentin section view. It takes approximately six to eight deformations to generate the upper dentin part to match the shape of the dentin based on the literature. In instances where the deform feature causes the enamel of fragment, attempt deformation at an alternative pinpoint, use reduced deform distance and region area, and adjust the deformation shape accordingly. Following all deformations, the final dentin structure is completely crafted. Produce a copy of the enamel and integrate the finished dentin with it, transforming the enamel solid into an actual enamel shell covering the dentin.

4. Creating the PDL:

In this step, select the lower part of the dentin surface and use the offset surface feature to complete this model. Input the offset distance and direction. If offsetting proves problematic, consider decreasing the bottom layers of dentin loft surfaces. After surface offsetting, apply the fill surface function to seal the bottom of the PDL, then converting the untrimmed PDL into a solid using the fill surface feature on the PDL's top surface. Next, create a horizontal trim plane based on the top view plane, adjust the trim plane's position to a distance approximately 2mm below the lowest buccal side enamel. Generate a copy of the untrimmed PDL surface and designate the trim plane as the trimming tool to eliminate the upper part of the PDL surface. Finally, use the fill surface feature to solidify the entire PDL. Integrate the PDL solid with the dentin and use a 3D sketch to create a rectangular shape on the circular surface at the top of the PDL. Use extrudes boss feature to generate the bone. Finally, combine the untrimmed PDL solid with the bone. At this stage, all

components, including bone, PDL, dentin and enamel. To assemble the tooth model with the percussion rod, establish a ketch point on the buccal side of the enamel to serve as a mate reference point.

5. Creating the Assembly of Tooth CAD Model and Percussion Rod:

In this final step, build an assembly for the tooth CAD model with the percussion rod. When opening SOLIDWORKS, select assembly mode and import both percussion rod assembly and the tooth part. Use the mate function to select surfaces of the enamel and rod tip for mating. Additionally, choose the mate reference point on the enamel and percussion tip point to finalize the mating of the percussion rod assembly with the tooth model. Finish up the process by saving the entire assembly and saving it as a ".xb" Paragould Binary file type for future meshing.

6. Creating CAD Models for Replica Teeth:

Replica teeth CAD models are simplified, excluding components like the percussion rod, PDL and bone. Instead, they focus only on enamel and dentin, forming the core of the replica teeth. To introduce vertical notches, the SOLIDWORKS software employs the "Extrude Cut" function. This involves defining the notch through two vertical planes parallel to crack planes, creating the desired vertical notch feature. For optimal printing, a recommended gap of around 350 μm between vertical notches is suggested. This precaution accounts for the tendency of the vertical notch to seal during 3D printing due to surface tension. However, the ideal gap size depends on factors like the printer, resin, and tooth geometries. Determining the precise vertical notch gap involves testing multiple print batches. The length of the vertical notch can be controlled using the horizontal split plane

in SOLIDWORKS. The final step is saving the tooth part as an "stl" file type, ready for 3D printing.

Meshing

Meshing is the essential process of converting CAD models into finite elements and nodes. For the creation of 3D CAD tooth models in the present study, MSC Apex software is used to generate the meshes. Here is a breakdown of the meshing procedures, specifying the mesh sizes and element types used for each component:

- PDL Meshing: The PDL is meshed using second-order isoperimetric three-dimensional ten-node tetrahedron elements with a mesh size of 0.1mm. Since the PDL thickness is 0.2mm, using 0.1mm mesh size on PDL would create at least two layers of elements for PDL.

- Percussion Rod Meshing: The percussion rod is subjected to meshing, use eight-node, isoperimetric, arbitrary hexahedral elements with a mesh size of 0.5mm.

- Percussion Tip Meshing: The percussion tip undergoes meshing with the same element type as percussion rod (eight-node, isoperimetric, arbitrary hexahedral), but with a finer mesh size of 0.3mm, for more accurate contact conditions with the tooth's enamel.

- Enamel, Dentin, and Bone Meshing: These tooth components are meshed with linear isoperimetric three-dimensional tetrahedron elements, with a mesh size of 0.2mm.

With the MSC Apex software, several critical tools are available, including solid mesh, 2.5D mesh and the split tool. The meshing process for the CAD models follows these steps:

1. Importing Geometry: Initiate the process by importing the geometry using the saved CAD ".xb" file. The model tree located at the top left corner of the interface, is expandable, enabling the naming and differentiation of individual contact bodies through distinct colors.

Use the solid mesh option with a linear element type to mesh enamel, dentin and bone. For the PDL, use the quadratic solid mesh element type. The mesh size can be adjusted to suit the tooth type and specific simulation requirements. Typically, it is advisable to maintain an element/geometry deviation ration of 0.10 and an element min/element global length ratio of 0.20.

2. Splitting the Percussion Rod: To facilitate 2.5D meshing on both the rod and tip of the percussion rod, use the geometry edit tools. Select for the "split tool" and use plane splitting by clicking once on the percussion rod and tip inter-junction. Position the red arrow the junction of the percussion rod by clicking the middle button on the mouse to establish the coordinates. Subsequently, select the plane's location indicated by the red arrow and click the middle button of the mouse again to execute the split.

3. Meshing the Percussion Rod: Access the meshing tools and select 2.5D meshing for the percussion rod. Apply a mesh size of 0.5mm for the rod and 0.3mm for the percussion tip. Use linear hex elements for both the rod and tip. Finally, ensure that all components undergo proper meshing, and export the APEX file in ".bdf" format with the unit set to mm-t-s-N for further analysis and simulation.

FEA Simulations Setup

The FEA simulations in this study are executed using MSC Marc/Mentat (MSC Software, Newport Beach, CA). The following steps outline the simulation process:

1. Importing Meshed Bodies: The previously meshed bodies are imported into MSC Marc. Initially, these meshed bodies are recognized as contact bodies, with their type defined as "meshed" (deformable).

2. Material Property Setup: Material properties are established for six different tooth components using in the FEA simulations, including dentin, dentin damage zone, bone, enamel, enamel damage zone, PDL and stainless steel. Each material is configured individually, with mass density determined according to Table 1. Other properties are set to elastic-plastic isotopic with a single network model. Young's modulus and Poisson's ratio are specified for each tooth material within references. Damping properties are applied to bone, dentin and PDL materials with detailed damping values discussed in dedicated section.

3. Defining Contact Interactions: Contact interactions are defined using two types "meshed (deformable) vs meshed (deformable) glue contact" and "meshed (deformable) vs meshed (deformable) touching contact". For glue contact interactions, contact tolerance is set at 0.01, with a contact tolerance bias factor of 0.95. The stress-free projection onto the contact surface option is enabled. As for touching contact interactions, the same tolerance values apply, and the contact type is set to touching.

4. Creating Contact Table: A contact table is generated to apply both glue and touching interactions to all contact bodies. Glue contact interactions are assigned to various pairs such as percussion rod and tip, bone and PDL, dentin and enamel, and PDL and dentin. Touching contact interactions are assigned to pairs like percussion tip and enamel, dentin buccal and dentin lingual (for cracked model), enamel buccal and enamel lingual (for cracked model).

5. Initial Condition Properties: Initial conditions are defined in terms of velocity, applied to all elements, including percussion rod and percussion tip. The velocity in the x-direction is set at 60 mm/s, while other directional velocities and rotational velocities are set to zero.

6. Boundary Condition Properties: Two structural fixed displacement boundary conditions are used. The first applies to percussion rod and tip nodes, permitting displacement only in the x-direction. The second is assigned to bone, imposing fixed displacement in all directions for nodes on the outer surfaces, while inner surface nodes remain free to displace. A face flood method with a default limit angle of 60 degrees is used to select all outer surface nodes of the bone. A structural dynamic transient loadcase is established. The load menu includes selections for "fixed in x only" and "fixed bone" boundary conditions.

7. Setting Loadcase: The total loadcase time is set to 0.0004 seconds, which records all necessary time steps within a total simulation time of 0.4 milliseconds. A constant time step is automatically generated, resulting in 200 steps within 0.4ms, corresponding to a time step of 2×10^{-6} seconds.

8. Setting the QPD Job: The job type is configured as "structure" named the QPD. In the loadcase section, the boundary condition applied in the previous step is selected. The initial loads menus includes both boundary condition and initial condition. In analysis option, large strain should be checked, selecting the "Lanczos buckle" and "Lanczos model" solution methods, and specifying parameters for the implicit dynamic transient operator. Advanced options use the "updated Lagrange" approach and permit switching to total language. In the job results menu, various output parameters including displacement, velocity, contact status, and contact normal force are selected. Other menus maintain default settings. With these configurations, the FEA simulation is prepared for execution. MSC Marc, showed for its capacity to model nonlinear material behaviors and transient environmental contagions, ensure accurate simulations under dynamic loading conditions.

Table 1: Materials properties of all components. [17], [21]–[24]

	Mass Density (kg/m³)	Young's Modulus (MPa)	Poisson's Ratio	Mass Matrix Multiplier α	Stiffness Matrix Multiplier β
Dentin	2140	14700	0.31	0.0907	0.00003
Cortical-Bone	1300	14700	0.3	0.0907	0.00003
Enamel	2970	84100	0.33	0	0
PDL	1200	0.1	0.45	1814	0.6
Enamel Damage Zone	2970	8410	0.33	0	0
Dentin Damage Zone	2140	1470	0.31	0.0907	0.00003
Steel	7850	207000	0.3	0	0

CHAPTER 1

FEA of Vertical Crack and Oblique Crack Detection for Single Rooted

Maxillary Second Bicuspid

Introduction

Cracked tooth syndrome is a term used to diagnose incomplete tooth fracture, characterized by common symptoms like pain during biting and temperature sensitivity especially to cold temperature. [25] Talim and Gohill's research has categorized incomplete fractured posterior teeth into two types: horizontal/oblique cracks and vertical cracks. [26] Their findings indicate that nearly all incomplete vertical fractures are situated along the central groove, extending both medially and distally. Initially, a vertical crack limited to the enamel is symptomless, only becoming noticeable when it extends into the dentin and the crack surfaces separate slightly. This progression is often accompanied by severe pain, particularly with cold stimuli during eating or pressure on the lingual or buccal surfaces. [26] A crack may propagate to the point where a tooth needs to be extracted by the time a reliable diagnosis is made. [27]

Talim and Gohill also identified predisposing factors contributing to tooth cracks, noting that most occur in the middle and advanced age group due to increased forces acting on cusps, resulting in weakened resistance to masticatory forces – a phenomenon known as fatigue cracking.[26] Chewing habits or ingesting hard particles from food can lead to occlusal wear, reducing the tooth's ability to resist biting forces. Occlusal fissures and grooves are common areas to crack initiation. Trauma or accidental biting on hard object, such as betel nuts, cherry stones, or bones, can cause sudden load concentration on tooth, initially cracks. [26] Notably, high school football players have been found to have unnoticed cracks in their teeth, easily included by trauma according to the clinical QPD tests.

Current dentistry faces challenges in detecting symptomless vertical or oblique cracks, especially during the early stages of the crack cycle, with limitations and disadvantages discussed in "Current Diagnostic Methods" section. This is also the case for other microgap defects (MGDs) such as failing crown cement seals resulting in microleakage and gaps along the implant-bone interface. [28] [29] Fortunately, the QPD has demonstrated potential in recent years for detecting and characterizing tooth cracks. [2] Clinically, the QPD tests have been applied to patient's teeth before extraction, revealing multiple peaks on the plot indicative of cracks. However, the QPD results alone do not provide detailed information about the vertical crack's condition, including length and gap. Figure 21 displays the QPD result of a bicuspid eventually extracted; post-extraction disassembly determined the vertical crack's presence. Yet, conditions may change during extraction due to undefined forces. Disassembly following extraction, while revealing the crack, does not necessary reflect its pre-extraction state. Similar situations arise with oblique crack, as seen in Figure 8, which is a post-extraction, disassembled tooth revealed a complete fracture, but the condition of the oblique crack before extraction remained unknown.

The purpose of the current work was to design and develop FEA models that replicate the percussion responses of premolars with oblique and vertical cracks when interrogated using the QPD. The goal is understanding the crack condition, especially crack orientation, length and gap space, through the QPD results. This understanding enables dentists to administer appropriate treatment and potentially save the tooth. This chapter utilized FEA simulation tools to address this issue by modeling various crack conditions – both oblique and vertical in a one rooted maxillary second bicuspid. In addition, the clinical QPD results will be compared with FEA findings for validation.

Modeling Methods

In this present research, two types of cracks were explored, oblique cracks that extend from the occlusal groove to the buccal surface of the tooth, and vertical cracks from the same occlusal groove. The oblique cracks had length of 5 mm and 7 mm as shown in Figure 13. These crack lengths are consistent with micro-Computed Tomography (CT) observations of cracked teeth during experimental studies. When the crack length is 5 mm, the crack tip is still above the enamel dentin margin and hence the enamel is not fully fractured. On the other hand, when the crack length is 7 mm, the crack tip is slightly above the PDL and below the enamel dentin margin, and therefore, the enamel is fully fractured into two pieces but is still attached to the cracked dentin. The crack opening displacement (gap space) was set to 5 μm between the buccal crack face and the lingual crack face for all models. This gap space is consistent with SEM observations and infrared thermography of cracked teeth. [30], [31] The average thickness of the PDL is approximately 0.2 mm, which is also consistent with reported in silico FEA as well as in vivo findings. [32] The percussion rod, shown in Figure 13, impacts on the buccal side of the tooth on the enamel.

The maxillary second bicuspid vertical crack models with crack lengths of 5 mm and 7 mm are shown in the Figure 14. The model on the left has a crack length of 5 mm, with the crack tip is above the enamel dentin margin. The model on the right shows the crack length of 7 mm, with the crack tip located below the enamel dentin margin and above PDL.

Literature review showed that the majority of previous studies considered linear elastic and isotropic for tooth components when analyzing their behaviors with relevant constitutive laws. For this present study, we also considered the tooth, periodontal ligament, and neighboring bone as isotropic linear elastic materials albeit with additional behavioral characteristics associated with Rayleigh damping. The basic properties of dental system components including elastic moduli,

Poisson's ratios, and mass densities used in this research paper are listed in Table 1. The mass matrix multiplier and stiffness matrix multiplier are assigned to dentin, bone and PDL, and they are acquired by the Modal analysis and damping partition according to previous research. [14]
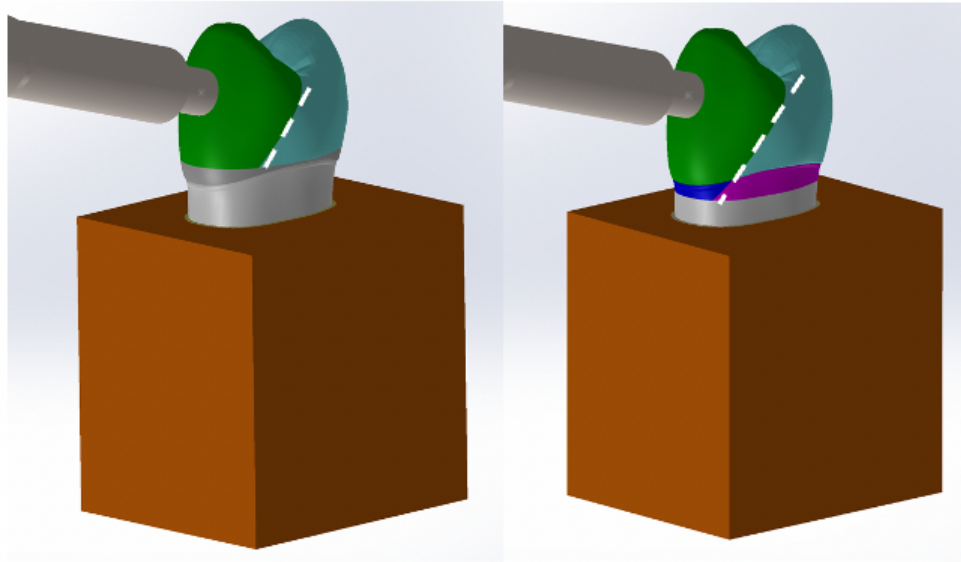
Figure 13: CAD assemblies of 5 mm and 7mm oblique cracks of a maxillary second bicuspid within the SOLIDWORKS software.
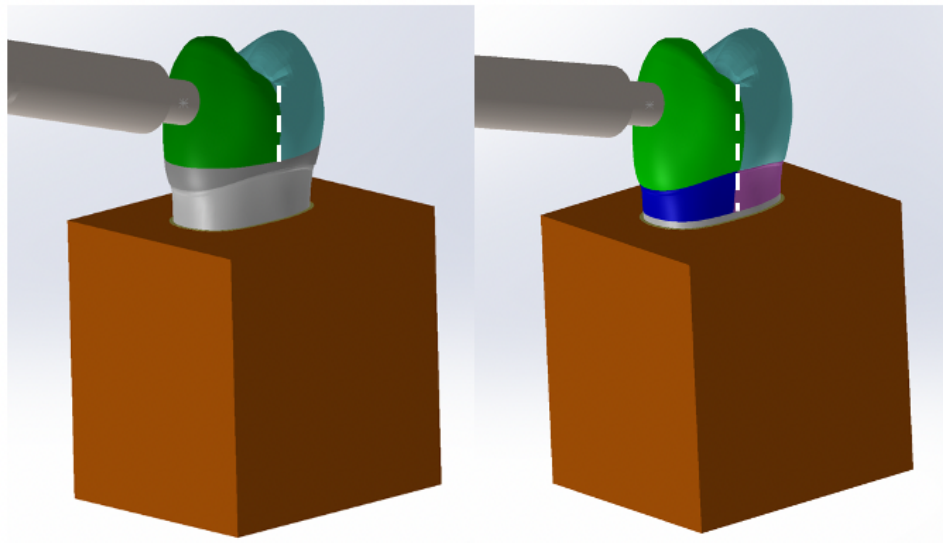
Figure 14: CAD assemblies of the 5 mm and 7 mm long vertical cracks within the SOLIDWORKS software.

A significant feature of the present FEA simulations is a damage zone at the crack tip. This damage zone corresponds to microstructural damage in the form of localized microcrack accumulation ahead of the crack tip. This damage constitutes a localized reduction of mechanical integrity that can be characterized by a reduction in stiffness. Accordingly, the elastic modulus in the crack tip damage zone was investigated using the present FEA simulation. A value corresponding to 10% of Young's modulus of the undamaged region was ultimately assigned to the damaged zone for both enamel and dentin components, listed in Table 1.

Two aspects of the crack were monitored for the present models to better understand how the presence of a crack leads to the multiple peaks observed in the measured force as a function of time. One aspect was the area of contact between the crack surfaces, which starts as zero and can increase and then decrease back to zero during the percussion. This contact could result in multiple peaks since there is an abrupt change in effective mass as both sides of the crack effectively combine during contact. Another aspect was relative acceleration between the two crack surfaces where the mass on each side of the crack could produce an additional force at the crack tip. The force produced would be related to the effective mass of tooth tissues on each side of the crack, so that the acceleration is equal to force divide by effective mass.

Results and Discussion

The percussion force response for an intact maxillary second bicuspid model as a function of time is plotted in Figure 15. The FEA simulation shows the maximum resultant force of approximately 10 N for a single bell-shaped curve. The shape of this single-peak response in percussion generated force is typically observed in vivo for intact teeth that contain no microgap defects. [33] This response is also consistent with impact force as a function of time for two elastic plastic defect-free bodies.[34] When there are no defects in the corresponding tooth, the force-time

32

plot shows a symmetrical bell-shaped curve with only one peak. Comparing the results shown in Figure 15 and Figure 16, the force-time response clearly exhibits multiple peaks a when crack is present in the tooth rather than resulting in only one peak as observed by the intact tooth. In addition, the maximum force reduces when the crack presents, due to the energy loss from closing the crack gap under percussion loading.
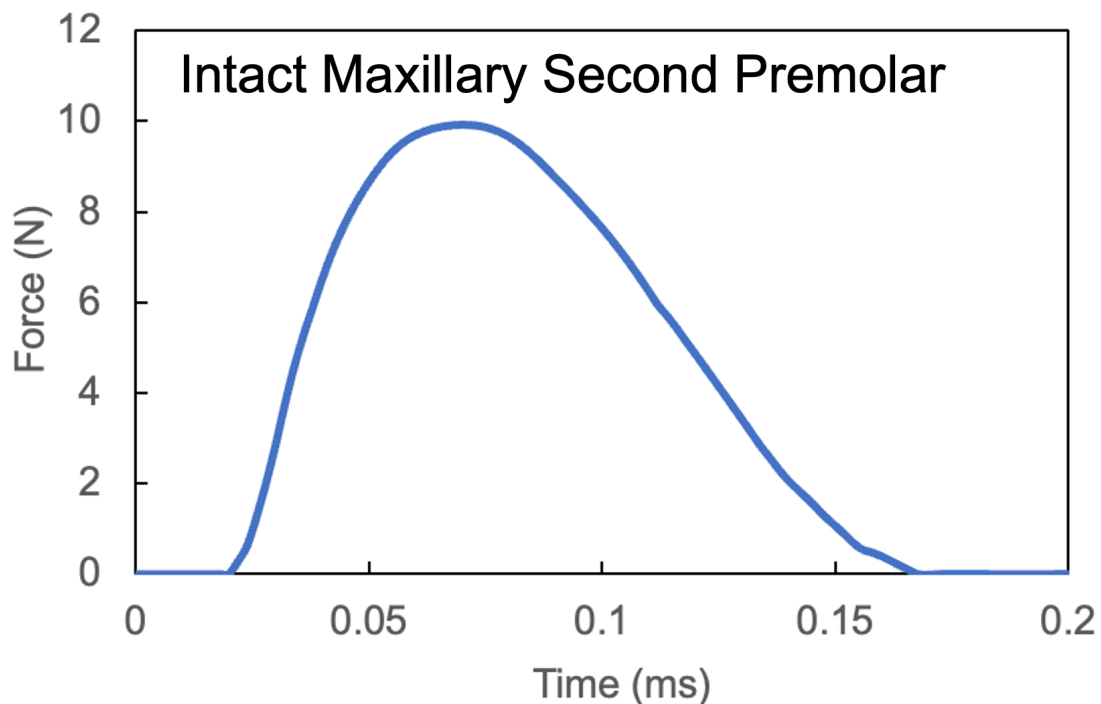
Figure 15: Force-time plot for an intact maxillary second bicuspid with no defects, damping partitions of 20 in the PDL and 0.001 in the bone and dentin, and a PDL static modulus of 0.1 MPa. Time increments are numbered along the force-time data curve.

Figure 15 and Figure 16, the force-time response clearly exhibits multiple peaks when a crack is present in the tooth rather than resulting in only one peak as observed by the intact tooth. In addition, the maximum force reduces when the crack presents, due to the energy loss from closing the crack gap under percussion loading.

Both percussion force at the rod sensor and area of contact between the crack surfaces are plotted in Figure 16 as a function of time for an oblique crack length of 5 mm. This FEA simulation

predicted a maximum resultant force of 7.3 N, notably lower than that for the intact bicuspid in Figure 15. This reduction in maximum percussion force is to be expected since the presence of a crack should reduce the overall stiffness of the tooth structure. The force versus time curve also exhibits multiple peaks as opposed to the single peak for an intact tooth as shown in Figure 15. This difference in response shape is consistent with the clinical QPD findings for intact and cracked teeth. [5], [27], [29]

Meshing drawings of sectional views of the oblique crack surface on the buccal side are also shown in Figure 16 for different time steps. The variations in colors along the edge of this face indicate the position of the interfacial contact between the enamel and dentin. The red region at the bottom of each of these drawings corresponds to the remaining intact ligament ahead of the crack tip. As shown in Figure 16, there is no contact between the cack surfaces at time equal to zero when the resultant force and contact area are initially at zero. At time equal to 0.038 ms (b), a small amount of contact is observed at the top right corner of the crack surfaces, where the change of color representing the contact appears. The contact area increases until 0.134 ms, where the crack surfaces are in maximum closure. Subsequently, the crack surfaces separate and contact area decreases until, at 0.252 ms, the two crack surfaces are completely separated as indicated by a contact area of zero. Overall, it does not appear from this figure that the peaks in force correspond to contact or contact area. In addition, we note from a comparison of Figure 16 and Figure 17 that the relative acceleration of the crack surfaces goes to zero while the area in contact is the highest.
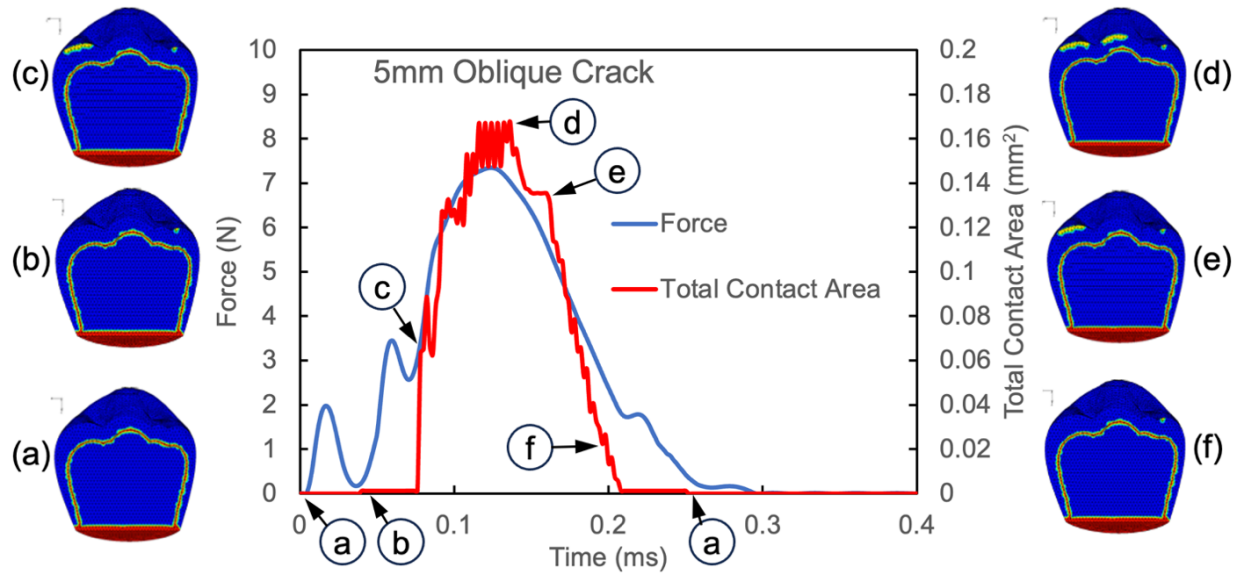
Figure 16: Resultant percussion force and crack surface contact area versus time for a 5 mm oblique crack in a bicuspid. Contact status contours on the buccal crack surface are also shown at 0 ms and 0.252 ms where there is no contact (a), 0.038 ms (b), 0.076 ms (c), 0.134 ms (d), 0.164 ms (e), and 0.198 ms (f).

Percussion force and relative acceleration of crack surfaces as a function of time for the maxillary second bicuspid with an oblique crack length of 5 mm are plotted in Figure 17. Relative acceleration is defined as the acceleration of the buccal surface of the crack subtracted from the acceleration of the lingual surface of the crack surface. It can be discovered in Figure 17 that the first two peaks in relative acceleration track with the first two peaks in force after a delay of about 2 µs. This time delay is due to the mechanical waves travel through dentin and enamel from crack tip to the rod force sensor. Multiple peaks on the force-time plot are correlated to the relative acceleration plot in Figure 17. The first peak on the relative acceleration corresponds to the first peak of the force-time plot. This is due to the force increasing as the percussion tip being in contact with the tooth, so the buccal side of the cracked surface moves toward the lingual side of the cracked face. Following that, the force decreases as the buccal side of the cracked face slows down, which causes the first peak on relative acceleration plot. Therefore, the first peak on the force-time

plot is caused by crack oscillation under percussion loading. Similar to the first peak of the relative

acceleration curve, the second, third and fourth peaks of this curve are correlated to the second,

third and fourth peaks on the force-time curve including that the oscillation of the crack surfaces

is sufficiently impactful on the force response of the tooth that it can be picked up by the sensor in

the percussion rod.
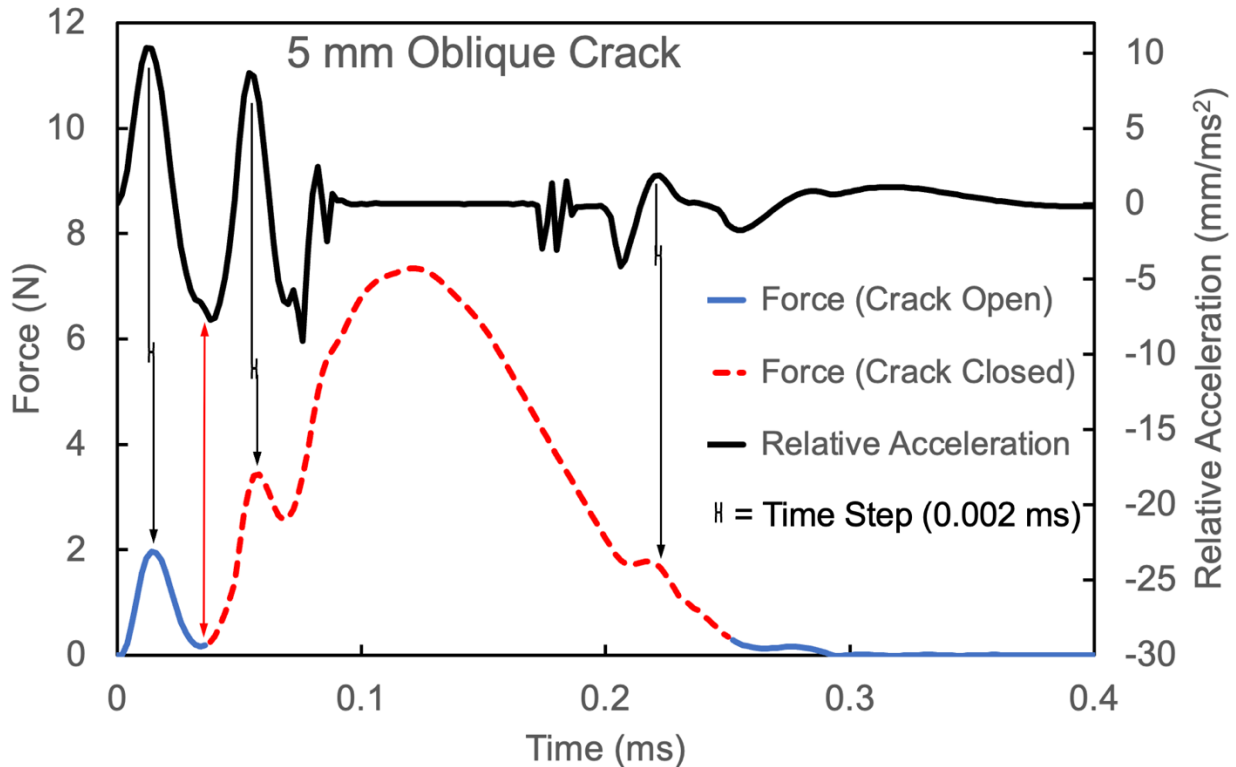
Figure 17: Force versus time for an oblique crack inclined toward the buccal side of a maxillary second bicuspid with an oblique crack with a length of 5 mm. The blue line corresponds to percussion force while the crack was open, and the dashed red line refers to when there was contact between the crack surfaces. Relative acceleration of the crack surfaces as a function of time is also plotted in black.

Percussion force as a function of time for a maxillary second bicuspid model with an

oblique 7 mm long crack toward buccal is plotted in Figure 18. These model results exhibit a

maximum resultant force of about 7 N, with multiple peaks present. The relative acceleration

between the crack surfaces is again plotted in this figure. Contact status results for the crack

surfaces are also indicated in Figure 18, where the blue part of the curve represents where the crack

is open (no contact) and red dashed line represents where the crack is closed (contact between the crack surfaces). This 7 mm crack goes beyond the enamel dentin junction, so the enamel is fully fractured although the two enamel sections are still attached to dentin. Black arrows in this figure demonstrate that multiple peaks in force vs. time again correlated to slightly earlier peaks in relative acceleration of the crack surfaces regardless of whether there is contact between the crack surfaces. A red arrow also shows that the onset of crack closure corresponds to a sudden change in relative acceleration. Similar to the results of 5 mm oblique crack shown in Figure 17, this 7 mm oblique crack FEA result also shows the correlation between relative acceleration of the crack surfaces and the peaks in the force-time plot. The first peak on the relative acceleration plot correlates to the first peak of the force-time plot, due to the crack oscillation that makes the first contact of the percussion tip on the tooth and separation of the tip as force goes back to zero. The following peaks on the relative acceleration curve also correlates to the following peak on the force-time plot, which further validates that the peaks on the force-time plot are caused by crack oscillation.

Unlike the short oblique crack FEA results, the longer oblique crack FEA results exhibit one isolated peak at the beginning. It seems that the isolated peak results from the instability caused by the longer oblique crack. When the percussion rod hits the tooth, the buccal side of the tooth moves faster than the percussion rod immediately after impact. Therefore, the first individual peak corresponds to the initial contact between the tooth and percussion tip.
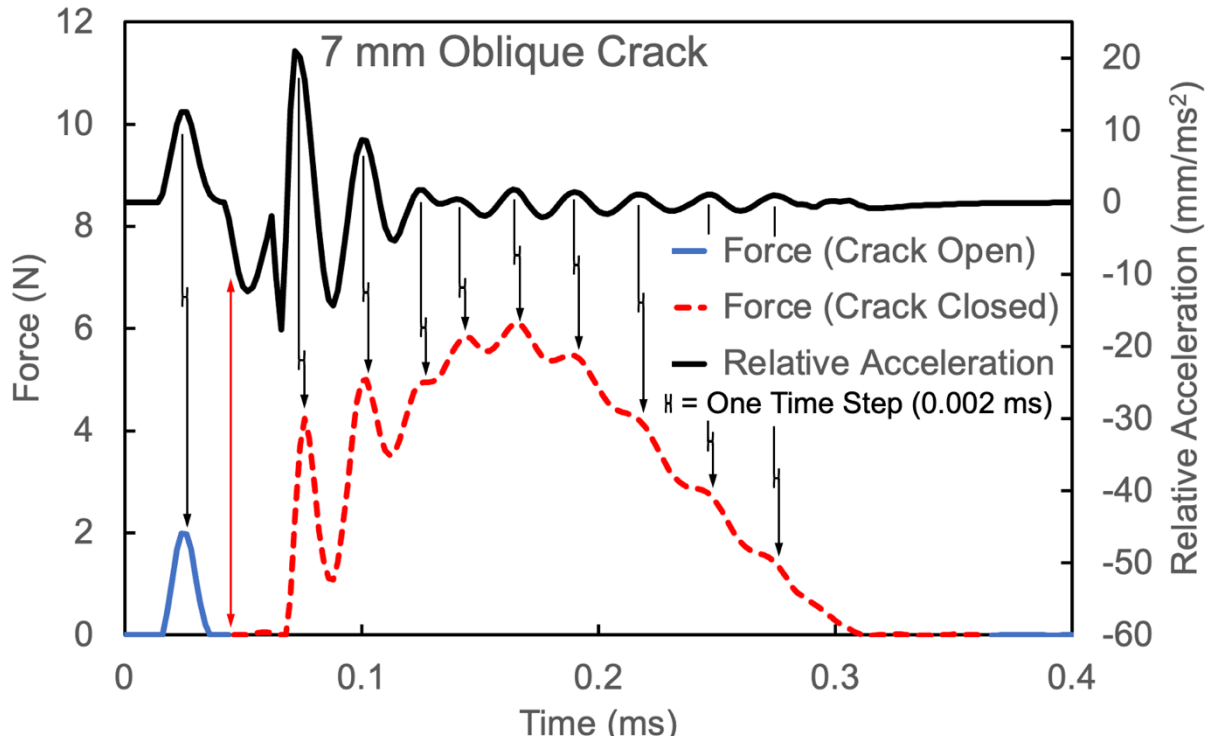
Figure 18: Force versus time for an oblique crack inclined toward the buccal side of a maxillary second bicuspid with an oblique crack with a length of 7 mm. The blue line corresponds to percussion force while the crack was open, and the dashed red line refers to when there was contact between the crack surfaces. Relative acceleration of the crack surfaces as a function of time is also plotted in black.

Percussion force vs. time for a vertical crack in a maxillary second bicuspid with a length of 5 mm is illustrated in Figure 19. The blue curve in this figure indicates the part of the predicted measured force-time response where the crack surfaces are not in closure status, and the dashed red curve indicated the force vs. time plot where the crack surfaces are closed in contact. There are multiple peaks in the force trend observed in this plot, some during contact as indicated in red, but others while there is no contact between the crack surfaces. The solid black line indicates the relative acceleration between the two crack surfaces. Similar to Figure 18, the peaks in the force response at the rod sensor region have one-to-one corresponding peaks in relative acceleration of the crack surfaces with the time for force to propagate from the crack tip to the force sensor in the percussion rod, approximately 2 μs taken into account. A red arrow shows that the onset of crack

closure also corresponds to a sudden change in relative acceleration for the crack surfaces. We note that this acceleration change is not reflected in the force-time data. The first and second peaks on the force-time plot in Figure 19 are not due to crack closure, but they are force oscillations caused by the change of relative acceleration of crack surfaces. When the percussion tip contacts the buccal side of the cracked tooth, the relative acceleration increases dramatically because the buccal side of the cracked tooth moves quickly toward the lingual side of the cracked tooth, while the lingual side does not move as fast as the buccal side. After a short period of time, the buccal side of the tooth starts to slow down due to the resistance from the intact dentin. As the first peak of relative acceleration starts to decay, the lingual side of the tooth starts to move at a higher rate of acceleration, which results in decreasing the relative acceleration. This phenomenon would lead to the first peak in black curve. This first peak in the relative acceleration plot has correlation to the force-time first peak on the blue curve, with the same time delay of 2 μs. The force starts to increase again when the acceleration of the lingual side starts to increase. The relative acceleration is close to zero during the crack closure at the region of dashed red line, because the buccal side of the crack tooth moves at nearly the same rate as the lingual side of the cracked tooth following being in contact. At 0.15 ms, the crack surfaces start to sperate as the relative acceleration becomes positive, because both the buccal and lingual sides of the cracked tooth move in the opposite direction relative to the percussion loading. In addition, the buccal side of the cracked tooth still moves faster than the lingual side of the cracked tooth.
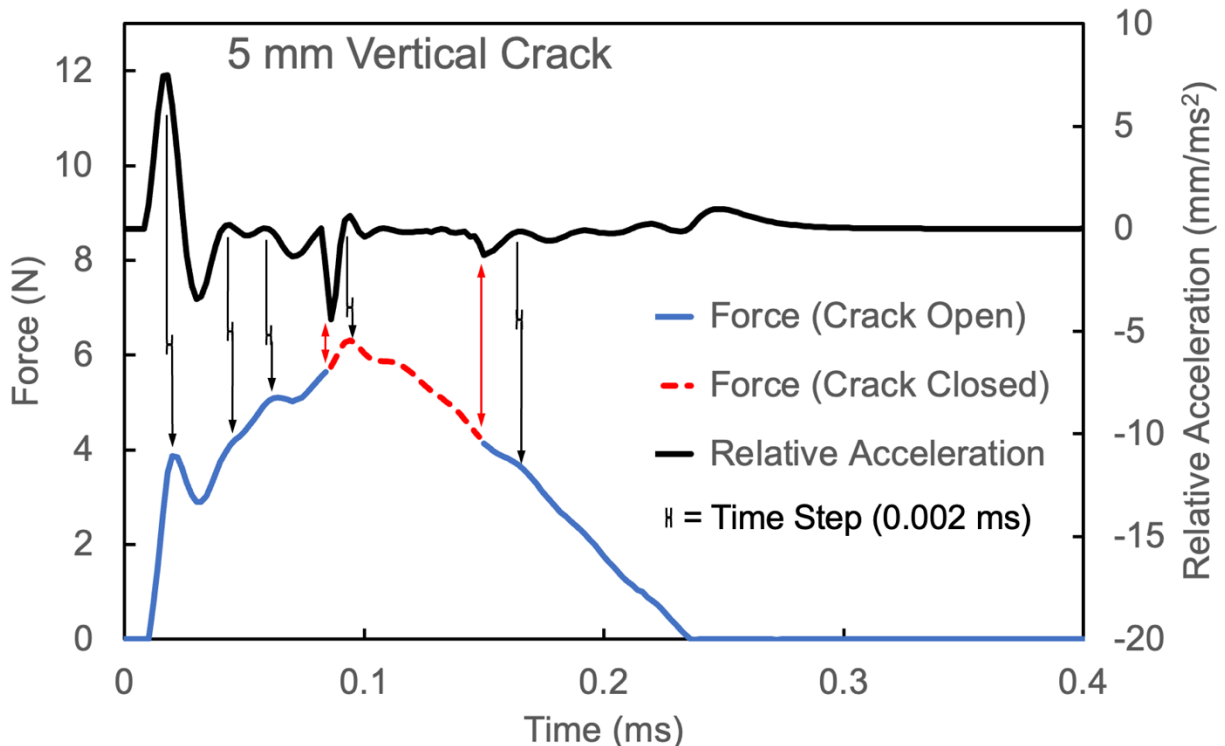
Figure 19: Force versus time for a vertical crack of a maxillary second bicuspid with a crack length of 5 mm. The blue line corresponds to percussion force while the crack was open, and the dashed red line refers to when there was contact between crack surfaces. Relative acceleration of the crack surfaces as a function of time is also plotted in black.

Percussion force versus time for a vertical crack for a maxillary second bicuspid with a crack length of 7 mm is shown in Figure 20. The crack tip is beyond the enamel dentin junction for this model, but not past the PDL conjunction. This percussion loading response exhibits multiple peaks, and the red dashed curve corresponds to when there is partial contact between the crack surfaces. This longer vertical crack exhibits a longer period of crack closure from 0.06 ms to 0.29 ms. Like the previous results, the first peak on the force-time plot is not during crack closure, rather it as well as the other peaks in percussion force corresponds to peaks in relative acceleration of the crack surfaces. A red arrow in Figure 20 also indicates a sudden negative change in relative acceleration of the crack surfaces occurs once the surface come into partial contact. The first peak on the force-time plot in Figure 20 is not due to the crack closure as with the previous results but

more likely it is due to the force oscillation resulted from the relative acceleration. In Figure 20, it is also shown that the peaks on the relative acceleration correlate to the peak on the force-time plot with the same time delay of 2 μs as previous results. In addition, the relative acceleration is also close to zero when the crack closure happens.
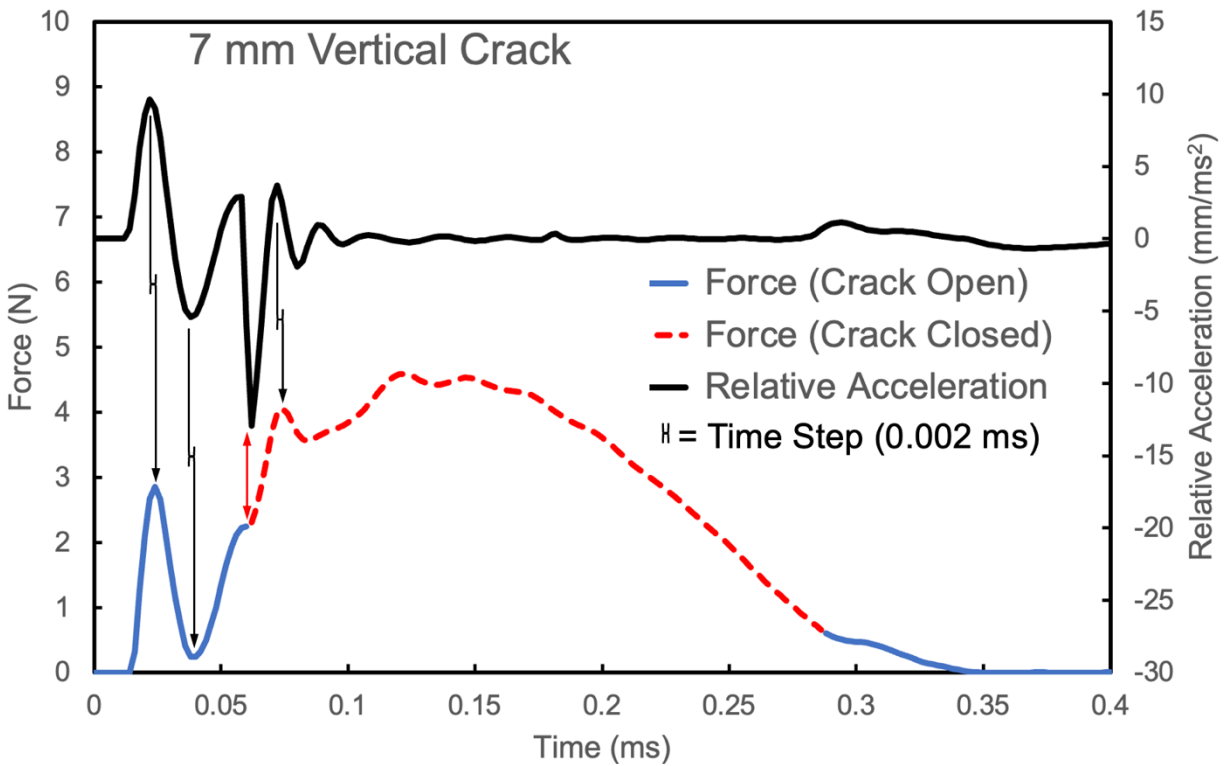
Figure 20: Force versus time for a vertical crack of a maxillary second bicuspid with a crack length of 7 mm. The blue line corresponds to percussion force while the crack was open, and the dashed red line refers to when there was contact between the crack surfaces. Relative acceleration of the crack surfaces as a function of time is also plotted in black.

The clinical QPD normalized force time response is plotted in Figure 21. The FEA vertical crack results are persistent with clinical results which also exhibit multiple peaks and deeper valley between peaks. Particularly, the shape of the first, second and third peaks are similar to the shape of the peaks of 7 mm vertical crack. Furthermore, the clinical QPD time duration is also comparable to the 7 mm vertical crack FEA results. Therefore, this clinical QPD result is in good agreement with the FEA results, which indicate the length of the actual vertical crack in the

41

bicuspid is close to 7 mm. Small observed difference between the clinical QPD and FEA result may be due to the tooth condition, such as pre-restoration, actual PDL conditions, tooth tomography, and crack conditions.
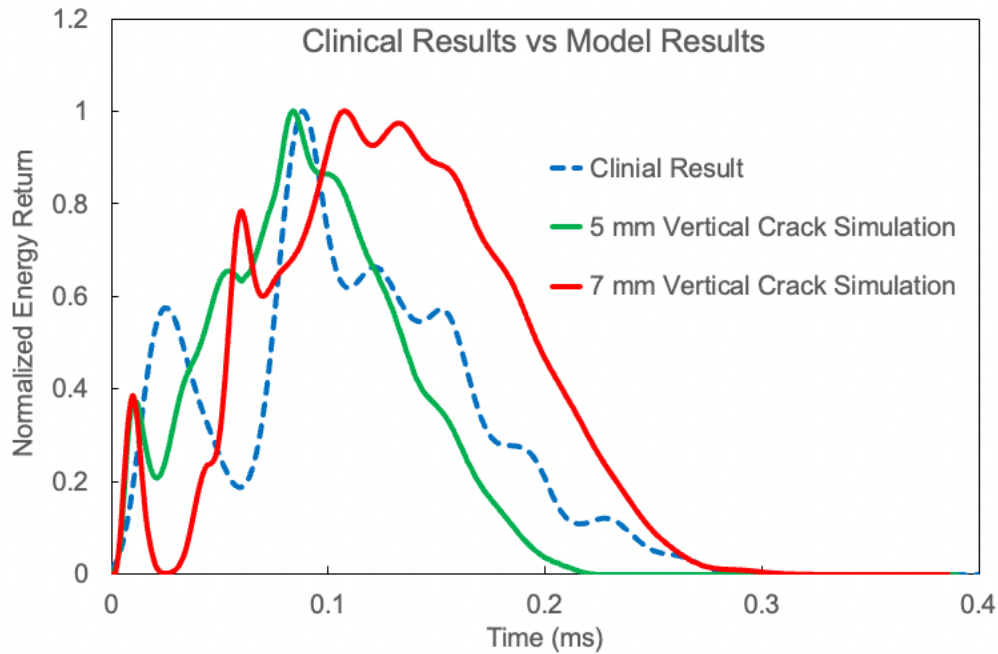
Figure 21: Experimental clinical and FEA generated QPD normalized energy return responses for a vertical crack in a maxillary second bicuspid.

Conclusion

The effects of oblique cracks and vertical cracks with short and long crack lengths on the QPD responses for a maxillary second bicuspid were investigated using FEA simulations. FEA results for oblique cracks inclined toward the buccal side of the tooth for a maxillary second bicuspid show multiple peaks on the force-time plot for both short and long crack lengths. An FEA result for a long oblique crack exhibits a greater number of peaks compared to that for a short oblique crack model. Contact status combined with relative acceleration of the crack surfaces indicated that the perks in the force-time response corresponding to a crack are a result of crack surface oscillation as opposed to contact between the crack surfaces. FEA models of vertical cracks

in a maxillary second bicuspid exhibit less prominent peaks compared to models of oblique cracks of similar crack length. The difference is likely position of the oblique crack top is closer to the side of the tooth resulting in more instability and higher amplitude crack oscillations, and therefore a greater number of peaks.

CHAPTER 2

FEA of Vertical Crack for Double Rooted Mandibular Second Molar

Introduction

Chapter 1 delved into the exploration of the vertical crack and oblique cracks in a single rooted maxillary second bicuspid, specifically examining variations in short and long crack lengths. In this chapter, we extend this investigation to focus on vertical cracks in a different tooth, the double rooted mandibular second molar, while comparing crack gap spaces. Existing studies have revealed that molars are highly prone to incomplete fractures, possibly attributed to sustained maximum masticatory forces exerted on these teeth over time. [26] Notably, mandibular second molar exhibit a significantly higher likelihood of fractures, nearly double that of maxillary molars. [35] Figure 9 illustrates a clinical finding of a vertical crack in a patient's mandibular second molar, recorded during disassembly. The QPD test was conducted, and the tooth was subsequently extracted for further examination. The vertical crack in this instance is oriented in mesial-distal, extending into the dentin structure below the level of PDL, with an estimated length of approximately 10 mm.

The QPD is a nondestructive method designed to assess the mechanical integrity of human teeth and implants, along with the underlying bone, while identifying the presence of cracks. This research focuses on virtual testing using a physiologically accurate 3D mode of a human mandibular second molar tooth (site 18), encompassing the surrounding tissues. The aim is to comprehend the dynamic behavior of the tooth under conditions consistent with the QPD. Employing a FEA approach, we studied the force response of dental structure to transient dynamic loading conditions simulating the QPD. Three models were employed: an intact tooth model, a 10 mm vertical crack model with 10 µm crack gap space and the same 10 mm vertical crack model

but with 20 μm crack gap space. This simulation mirrors the clinical case presented in Figure 9. The FEA results demonstrated noteworthy alignment with experimental data obtained from the patient's mandibular second molar, considering the identical crack length, orientation, and location. Furthermore, the crack surface contacts, and relative acceleration shows the crack oscillations and closure of the crack in response to percussion, and results for different crack gap spaces were compared. This research introduces an innovative approach to studying the dynamic behaviors of dental structures by analyzing their response to the QPD. Additionally, it highlights the computational power of the QPD in nondestructively assessing the presence of cracks.

Modeling Methods

The selected tooth model for this FEA study in this chapter is a representative human mandibular second molar, denoted as tooth number eighteen. Mandibular second molars are categorized as permanent molars, constituting the largest and most robust teeth in each dental arch. Their loss can have detrimental effects on arch continuity and the patient's ability to effectively chew on food. These molars, characterized by two roots – a lengthy mesial root and a shorter distal root, possess the longest roots relative to crown length among all human teeth. [36] Figure 22 (a) provides a cross-sectional view of the tooth model, revealing the distinct structure including enamel, dentin, an empty pulp chamber with root canal, the PDL, and the surrounding bone. In Figure 22 (b) and (c), the buccal and distal views of the tooth model are depicted, with a 10 mm vertical crack highlighted by the red in Figure 22 (d). This vertical crack originates from the occlusal surface groove region, extending vertically downward beneath the enamel dentin junction and reaching a level below the PDL.
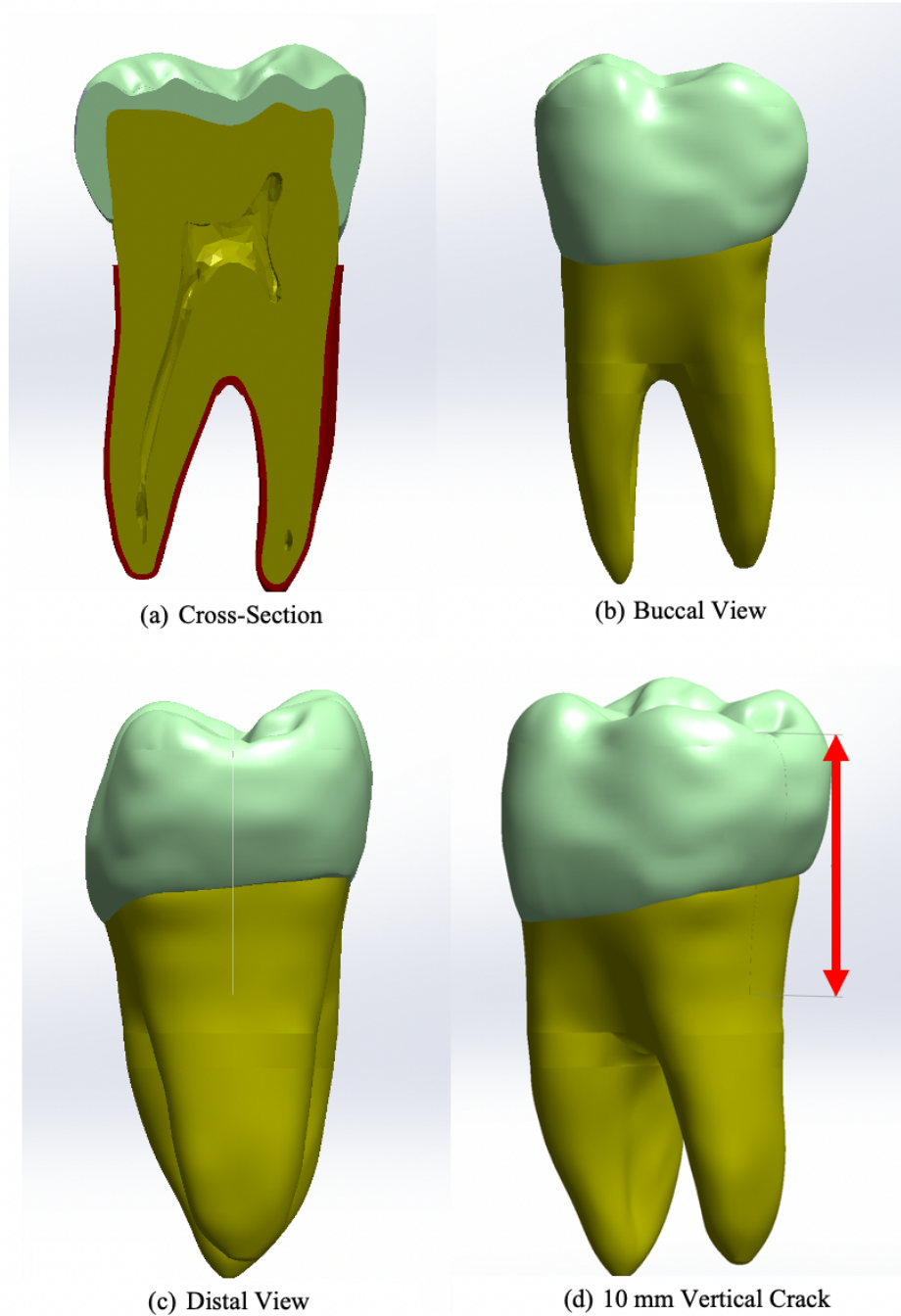
Figure 22: Different views of the tooth geometry: (a) cross-section of molar embedded in periodontal ligament, (b) buccal view of the molar, (c) distal view of the molar with a 10 mm vertical crack, (d) buccal- distal view of the molar with a 10 mm vertical crack.

The anatomical accuracy of the 3D model ensures a faithful representation of a typical

human mandibular second molar with a vertical crack. The model contains approximately 200,000

elements as shown in Figure 23. Employing conventional meshing and FEA setups, I conducted simulations mirroring an in vivo molar with a 10 mm vertical crack extending from the occlusal surface vertically into the dentin as shown in Figure 9. The crack features a specified gap space between crack surfaces, ranging from 10 μm and 20 μm.
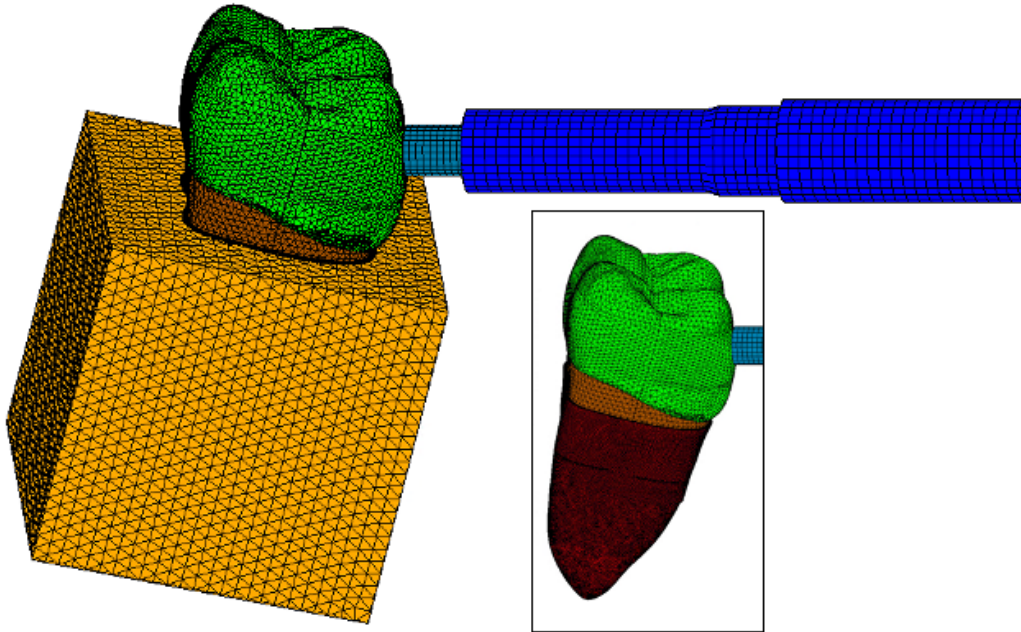
Figure 23: Complete finite element model used in the present study in MSC Marc/Mentat software environment.

Throughout this investigation, we consistently employed key material properties such as Young's modulus, Poisson's ratio, density, and damping properties. The concept of a damage zone, the same as mentioned in previous chapter, becomes an integral aspect of this chapter. Specifically, within this chapter, a proportion equivalent to 10% of the Young's modulus of the undamaged region was allocated to the damaged zone for both enamel and dentin components, as detailed in Table 1.

Results and Discussion

The mechanical responses to the applied percussion loading were presented through plots depicting the resultant force versus time increments, specifically at the sensor position in the QPD percussion rod. In Figure 24, a comparison is drawn, showing the resultant force-time plots for both intact and cracked teeth, each with two different crack openings, all scaled equivalently in time. This visual representation reveals a noteworthy reduction in the force resulting from percussion on both cracked teeth modeled results, in contrast to the intact tooth. In addition, Figure 24 confirms that the response of an intact tooth to the percussion is a smooth pulse, whereas irregularities are observed in the percussion force response when a crack is present. Examining Figure 27, a noteworthy concordance in the shape of the curve and the QPD time duration is observed between the simulated results and the in vivo experiment, specifically within the percussion event time. It is essential to note that the well-matched FEA model results were simulated with reduced elastic moduli for PDL, enamel and dentin. This adjustment mirrors the clinical condition of the tooth depicted in Figure 9, where the tooth has a history of restoration resulting in damaged enamel and detin, and the crack extends beyond the PDL level resulting in damaged PDL.

Based on the obtained results, the presence of multiple peaks is evident when a vertical crack exists in the molar. An intriguing question arises that how these peaks be interpreted. A postulated hypothesis suggests that these peaks arise from the crack oscillation and potential crack closure similar to the concepts discussed in Chapter 1. When the crack opening is sufficiently small, as indicated by a 10 μm crack gap space, the force applied by the percussion probe gradually closes the gap. The resultant force demonstrates a direct correlation with the contact between the crack

surfaces on the crack-plane. In other words, larger contact areas correspond to more substantial force oscillation.
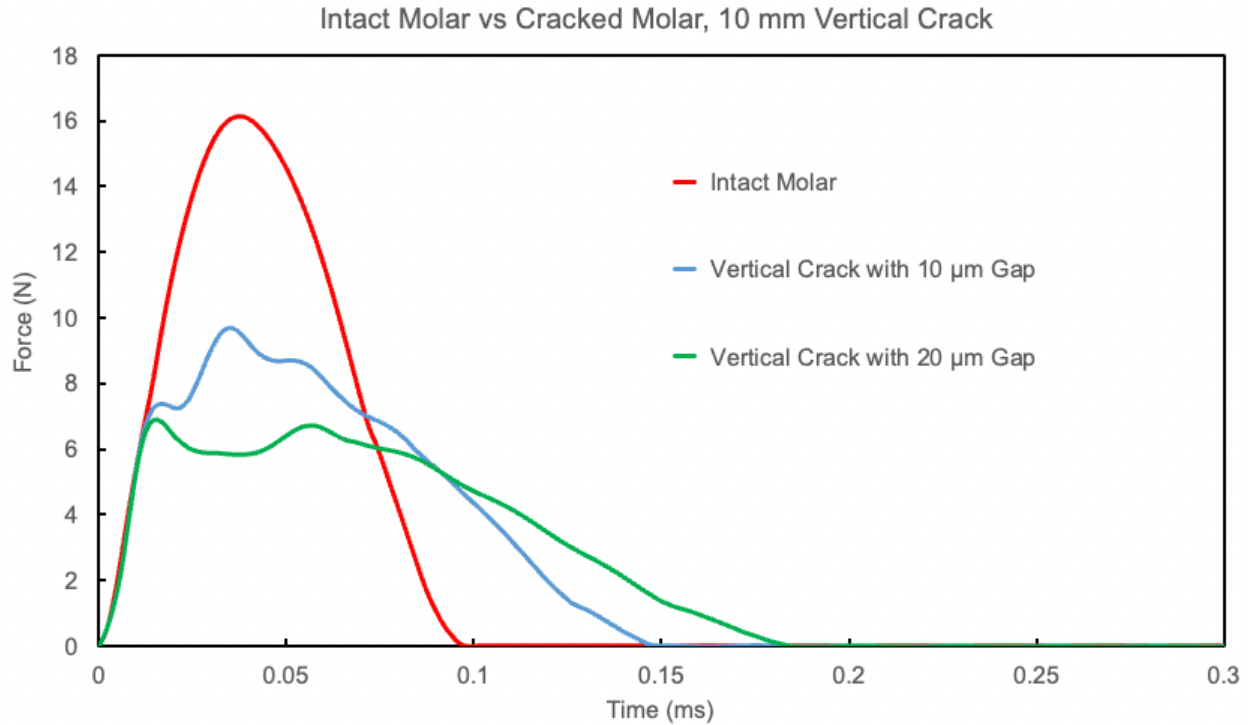
Figure 24: Resultant force versus time for (a) an intact second molar and (b) the same tooth containing a crack.

However, it is crucial to note that multiple peaks may not solely result from crack closure, they are also be attributed crack oscillation. In fact, crack oscillation may result in crack closure when the crack gap space is sufficiently small. While crack oscillation generates multiple peaks, the shape of the curve differs when compared with scenarios where crack closure occurs. According to Figure 24, the peak height and maximum force are higher when crack closure takes place in the molar with a 10 μm crack gap space. To investigate into the phenomena of crack oscillation and crack closure, we examined the contact status and relative acceleration between crack surfaces shown in Figure 25 and Figure 26. The contact status formed during the percussion

loading in the tooth is represented by the red dashed line in Figure 25, corresponding to the force vs time increments when crack closure occurs.
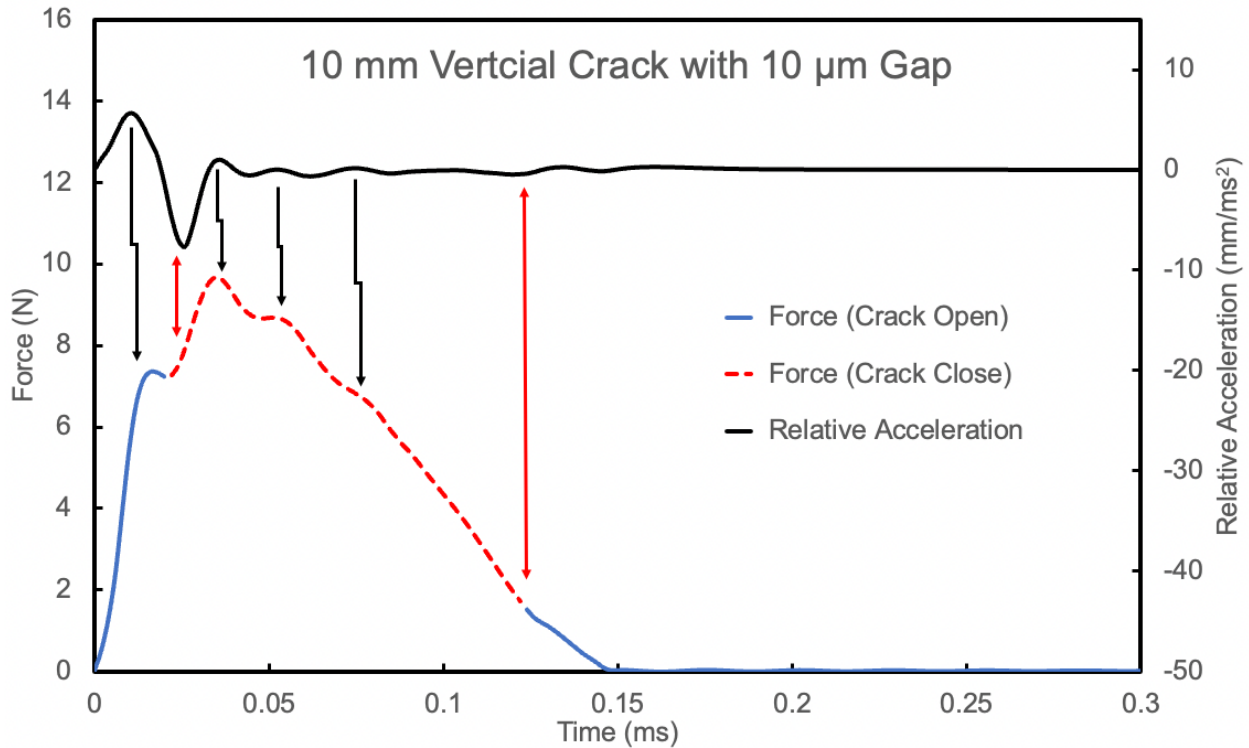
Figure 25: Force vs time plot and relative acceleration plot for 10 mm vertical crack with 10 μm crack opening.

In Figure 25, the FEA results depict a molar with a 10 mm vertical crack and a 10 μm crack gap space. The force versus time plot is represented by the red and blue curves, indicating crack open and close status, while the relative acceleration of crack surfaces is plotted in black curve. As shown in Figure 25, three peaks are discernible on the force versus time plot when the crack opening measures 10 μm. These peaks arise from a combination of crack oscillation and crack closure phenomena.

Upon contact with the tooth enamel, the force experiences a rapid increase, as indicated by the blue solid line, signifying that the crack surfaces are not yet in contact. Around 0.014 ms, the crack surfaces come into contact, as indicated by the onset of the red curve, persisting until 0.128

ms when the crack surfaces start to separate, leading to the reopening of the crack. The cracked body continues its movement until the percussion rod is no longer in contact with the tooth around 0.15 ms, causing the resultant force to return to zero.

The black curve representing relative acceleration between crack surfaces provides insights into force fluctuating during the percussion loading upon the cracked tooth. The first peak in the force versus time plot corresponds to the first peak in the relative acceleration, with a time delay around 2 μs, a correlation discussed in Chapter 1. The second peak on the force versus time plot is notable for its highest peak amplitude, increasing after the first peak when the relative acceleration shows the second peak. This occurrence is attributed to the ongoing closure of the crack opening and the ensuring oscillation, indicating a direct impact on the force versus time plot. Red arrows indicate the initiation and ending of the crack closure, aligning with sudden slope changes in relative acceleration at the peak valley. When the resultant force reaches its maximum, signifying the dissipation of total kinetic energy, a subsequent decrease in force is observed. Additionally, during crack closure, the relative acceleration approaches zero, reflecting synchronized movement between the buccal and lingual sides of the cracked body.
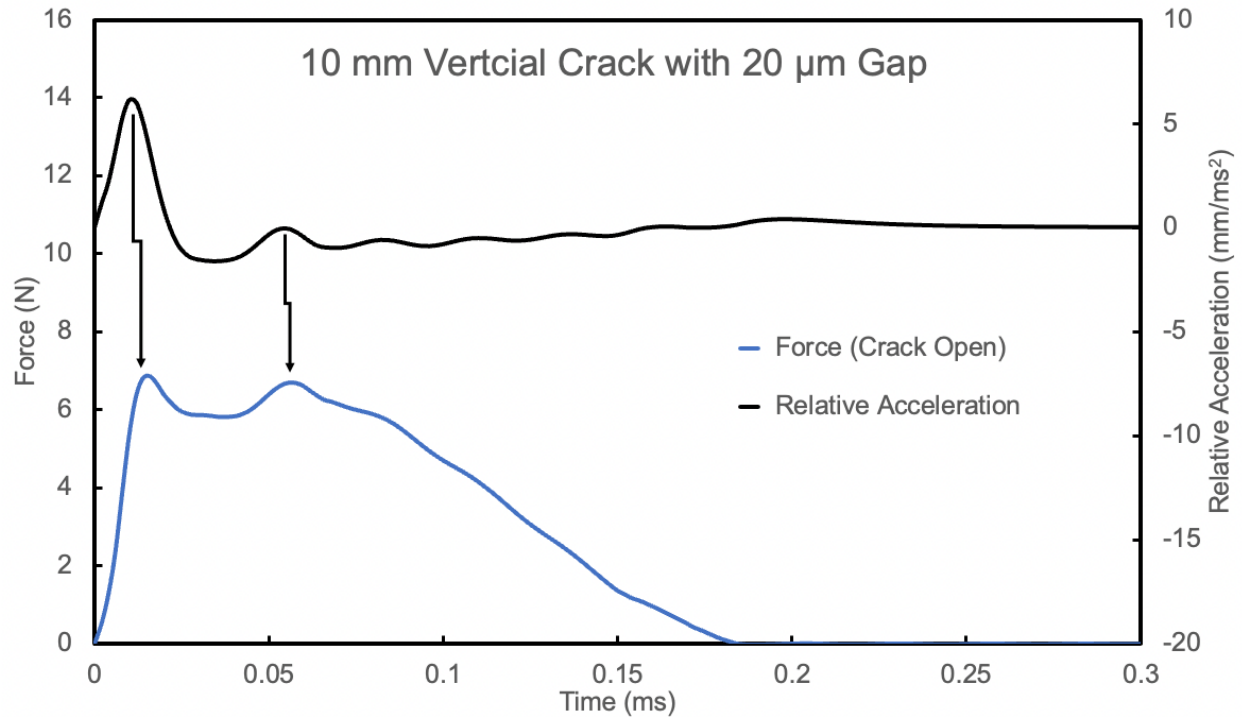
Figure 26: Force vs time plot and relative acceleration plot for 10 mm vertical crack with 20 μm crack opening.

Figure 26 presents the FEA result for a molar featuring a 10 mm vertical crack with a 20 μm crack gap space. The force versus time plot is depicted by the blue curve and the relative acceleration of crack surfaces is shown in black curve. When the crack gap space increases to 20 μm, two peaks emerge on the force versus time plot, as evident in Figure 26. Similar to the previous FEA results with a 10 μm crack gap space, the force response is intricately tied to crack oscillation between the crack surfaces. A key distinction lies in the fact that with a 20 μm crack gap space, the opening is sufficiently large, precluding any crack closure throughout the QPD test. Consequently, the shape of the curve on the force versus time plot is solely caused by crack oscillation. In Figure 26, the relative acceleration plot is also provided to scrutinize the characteristics of the force versus time plot. Remarkably, it was observed that the first peak on the relative acceleration plot aligns with the first peak on the force versus time plot, introducing a time delay of 2 μs. As crack surfaces oscillate again, the second peak manifests on both the relative

acceleration plot and the force versus time plot. This correlation underscores that these two peaks are intricately correlated to crack oscillation, a relationship further substantiated by the evidence presented in the relative acceleration plot.
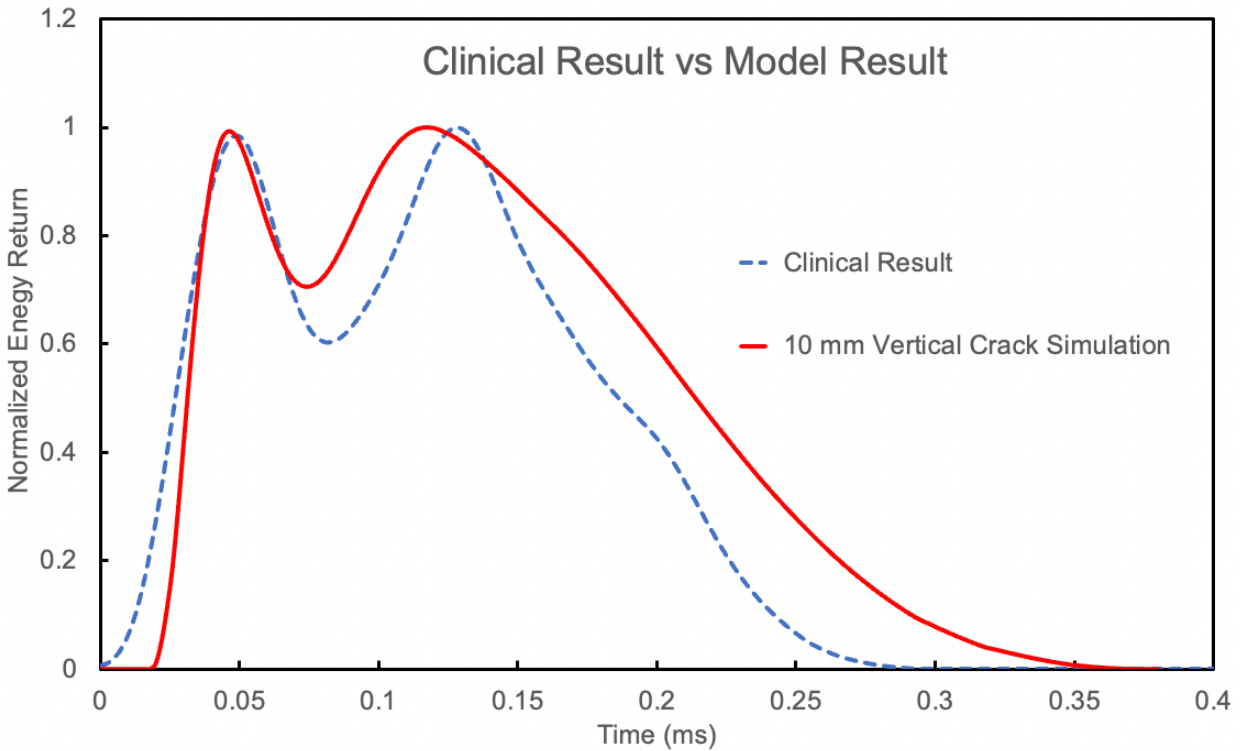
Figure 27: Comparison of normalized energy return versus time for clinical result and FEA model result.

The comparison between the QPD clinical results and FEA model results of force versus time is presented in Figure 27. The blue dashed line represents the clinically tested QPD on a molar with an estimated 10 mm vertical crack, while the red curve represents the FEA model result with predicted reduced moduli in PDL, dentin and enamel to emulate the pre-restored tooth condition in this molar. The clinical result distinctly exhibits two peaks with a total time duration of 0.3 ms.

The force versus time result generated by the vertical cracked FEA model with a 20 μm crack gap space demonstrates good agreement with the QPD experimental results, with both results displaying two peaks. Nevertheless, the FEA result exhibits a wider second peak and longer time

duration, although the first peak width remains relatively consistent. The overall shape of the FEA model result closely aligns with the clinical result. However, differences in shape of the curves may be attributed to various factors.

Firstly, the crack conditions and locations are not precisely identical to the extracted tooth. Discrepancies in crack length and crack opening size may exist. Even though the FEA model employs the same mandibular second molar, variations in tooth size and geometry could impact the results. Secondly, the kinetic energy exerted by the percussion rod may differ between the FEA model and the experimental QPD testing. The initial velocity defined in the FEA model was 60 mm/s, but real-world initial velocity of the QPD testing could vary. In general, a larger initial velocity would increase kinetic energy, resulting in an elevated overall peak amplitude and a longer time duration, as cracks take more time to dissipate the kinetic energy.

Observations in Chapter 1 and 2 reveal that the force time plot of a double rooted molar containing a vertical crack exhibits fewer peaks compared to the outcome observed in a single rooted bicuspid with similar vertical crack discusses in Chapter 1. This discrepancy is attribute to the inherent stability of double rooted molars, leading to reduced mobility under percussion loading and consequently yielding diminished crack oscillation.

The rationale behind this phenomenon lies in the enhanced structural stability of double-rooted molars in comparison to their single rooted bicuspid. The increased root support in molars result in a more secure tooth assembly, so minimizing the degree of movement experienced during loading. This reduced mobility contributes to a reduction in crack oscillation, translating into a force time plot characterized by a fewer number of peaks.

Conclusion

The dynamic response of a second mandibular molar (site 18), in intact and vertical crack states, were thoroughly examined using a finite element approach. FEA simulation results demonstrated a commendable agreement with quantitative percussion diagnostic results within the percussion event time. This agreement persisted between the virtual model and an in vivo cracked tooth, even though the crack dimensions and location were not precisely replicated. The force-time response of the cracked tooth proved to be considerably lower than the intact tooth, indicating resistance encountered by the stress wave due to the presence of the crack (gap) in the tooth. The existence of the crack resulted in energy dissipation. The relative acceleration plots demonstrated that the peaks are correlated to crack oscillation, and crack closure could alter the shape of the force versus time plot. When the crack opening is sufficiently small at 10 μm, contact occurs between tooth crack surfaces due to the percussion rod impact, resulting in the maximum possible closure of the crack and a higher resultant force. This is represented by the multiple peaks on the force-time plot. Conversely, when the crack opening is large than 20 μm, the peaks on the force versus time plot are purely associated with the crack oscillation. In conclusion, our study's simulation results confirmed that the QPD is a reliable method capable of swiftly and accurately assessing the presence of a vertical crack in a molar.

CHAPTER 3

FEA of Vertical Crack with Damaged PDL for Mandibular Second Molar

Introduction

This research builds upon the investigation of mandibular second molar vertical cracks outlined in Chapter 2. The current study utilizes FEA to simulate the dynamic behavior of a human mandibular second molar tooth under percussion loading conditions. This chapter's focus is on both a defect-free intact molar and multiple cracked molars with damaged PDL, aiming to analyze the mechanical responses aligned with the QPD. During the FEA simulations in this chapter, a thorough consideration of conditions associated with cracked molars is undertaken. Specifically, the likelihood of complete enamel fractures in the presence of a vertical crack in the molar is explored. Regardless of the vertical crack's length, enamel is prone to full fracture due to its brittleness relative to dentin. The enamel dentin junction acts as a barrier resisting crack propagation into the dentin from the occlusal surface. Such crack conditions, exclusive to enamel, are commonly referred to craze lines. These non-serious longitudinal fractures, prevalent in adults, extend over marginal ridges, buccal and lingual surfaces in posterior teeth, as depicted by long vertical cracks in Figure 28. Craze lines are confined to enamel and arising from natural causes, are a frequent occurrence. [18] Consequently, when modeling cracked molars in FEA, both fully fractured enamel models and those with short vertical cracks are considered.

Another clinical condition that considered in the FEA simulation was presences of damaged PDL. PDL commonly undergoes damage when a longer when a long vertical crack is present in the tooth, typically extending beneath the PDL level. Infections are a frequent cause of damage PDL, leading to a significant reduction in modulus compared to healthy PDL. In severe cases of cracked teeth, the PDL might become loose. Literature supports the presence of

granulomatous tissue infiltration in cases where an extracted vertical crack tooth extends deeply into the root.[18] Therefore, this current research explores various types of damaged PDL, modeling and simulating them for comparison with healthy PDL when a vertical crack is present in the tooth, especially one that is longer and extends beyond the healthy PDL level. This approach offers an innovative method to analyze the dynamic behaviors of dental structures, assessing their responses under the QPD tests in presence of damaged PDL along with a vertical crack in molar.
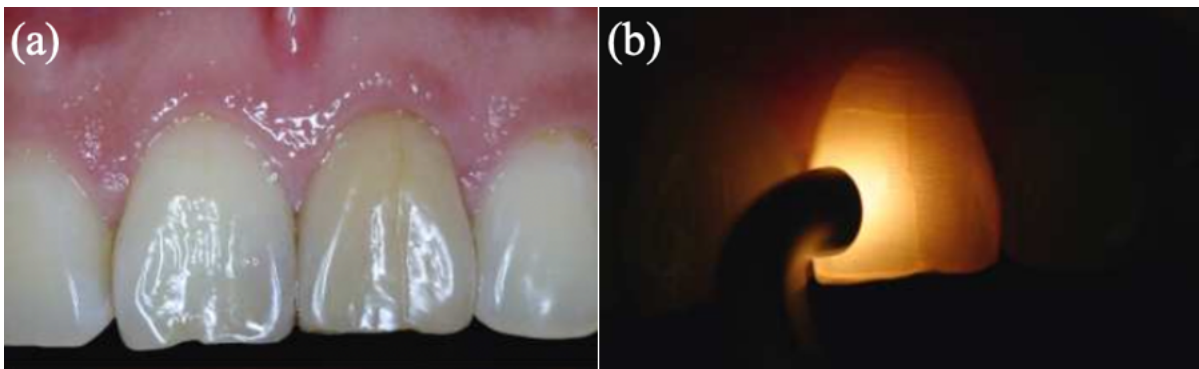
Figure 28: (a) craze lines (b) transillumination diagnosis provides further details of craze lines.[18]

Modeling Methods

Various lengths of vertical cracks were modeled and simulated, including lengths of 1 mm, 3 mm, 5 mm, and 10 mm with gap spaces between the crack faces set at 20 μm. In instances where the crack length was 1 mm, the crack had not yet penetrated the dentin, resulting in a vertical crack confined to the enamel, as shown in Figure 29. For crack lengths of 3 mm and 5 mm, the crack tips were positioned above the enamel dentin junction, and although the enamel was not fully fractured, there was a possibility of brittleness-induced fractures, as shown in Figure 30 and Figure 31. Consequently, models with fully fractured enamel vertical cracks were also created and present in Figure 33. Crack length of 10 mm were long enough for the crack tip to extend below the PDL

level, leading to full enamel fractures, as shown in Figure 32. This study compares the results of different vertical crack lengths using FEA simulations.

In addition, various damaged PDL conditions were modeled and simulated for 10 mm vertical cracks due to infections in the PDL. The modulus of the damaged PDL was reduced to 0.005 MPa from healthy PDL modulus of 0.1 MPa. Models with crack gap sizes of 20 μm were created for the 10 mm vertical crack length.

In the FEA MSC Marc setting, the PDL modulus could be easily adjusted in the material property settings. PDL moduli of 0.1 MPa, 0.05 MPa, 0.01 MPa, 0.005 MPa, 0.001 MPa and 0.0001 MPa were tested and compared in this study.
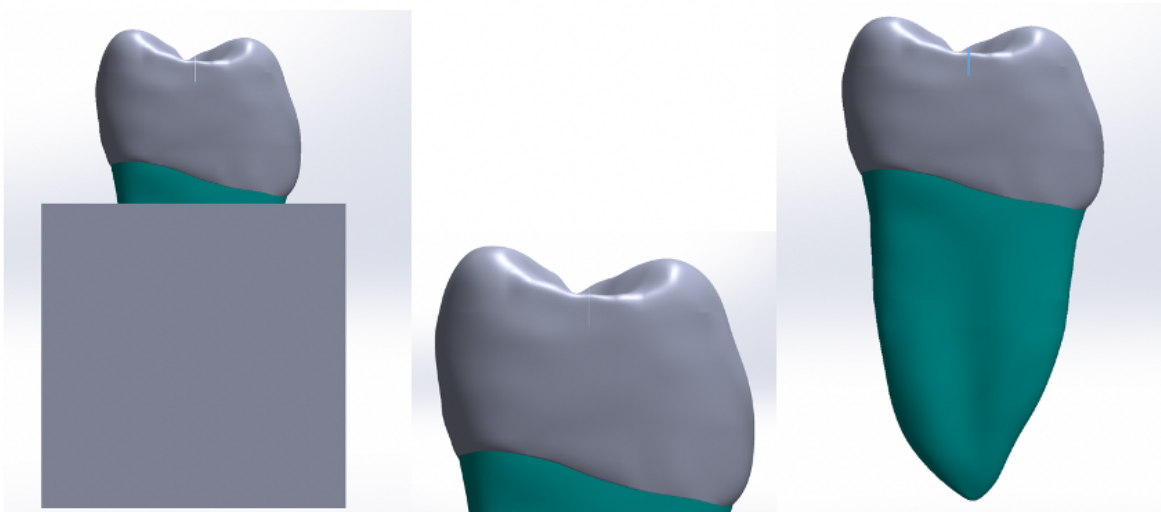
Figure 29: Mandibular second molar with 1 mm vertical crack CAD model.
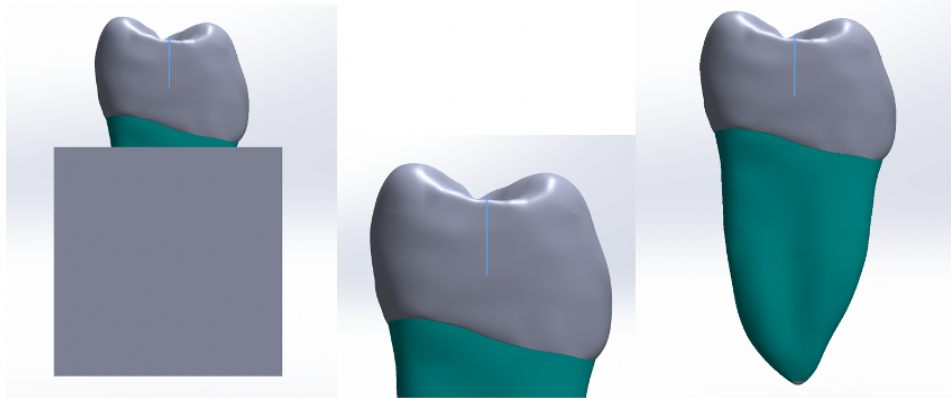
Figure 30: Mandibular second molar with 3 mm vertical crack CAD model.
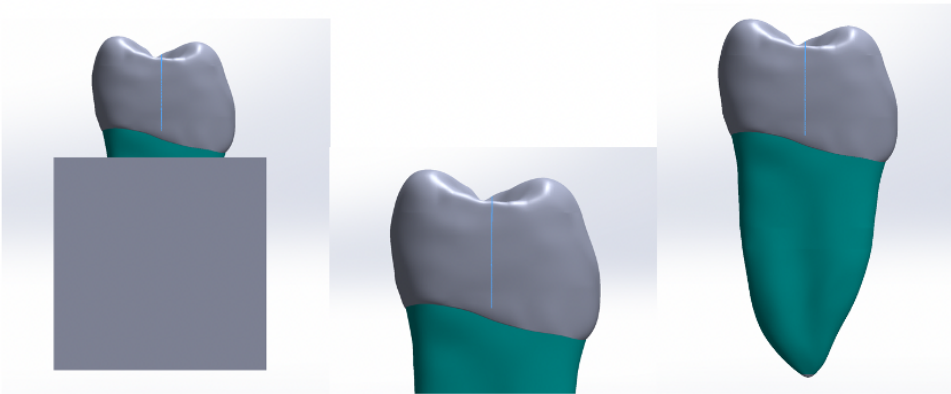
Figure 31: Mandibular second molar with 5 mm vertical crack CAD model.
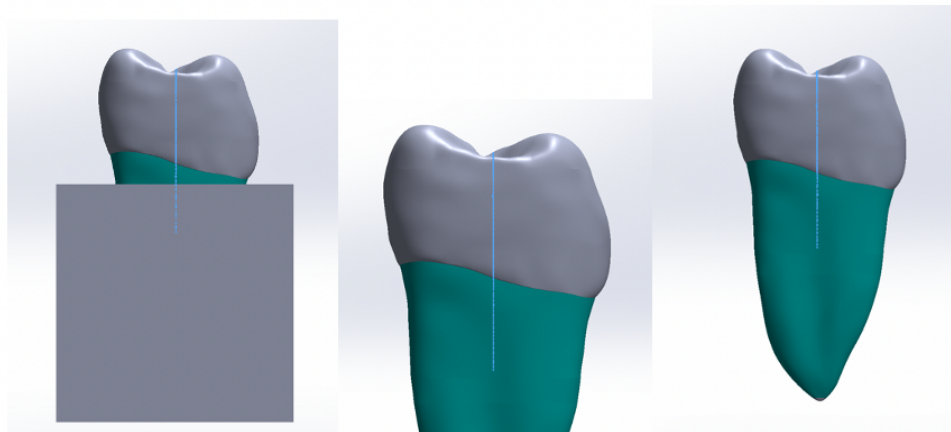
Figure 32: Mandibular second molar with 10 mm vertical crack CAD model.
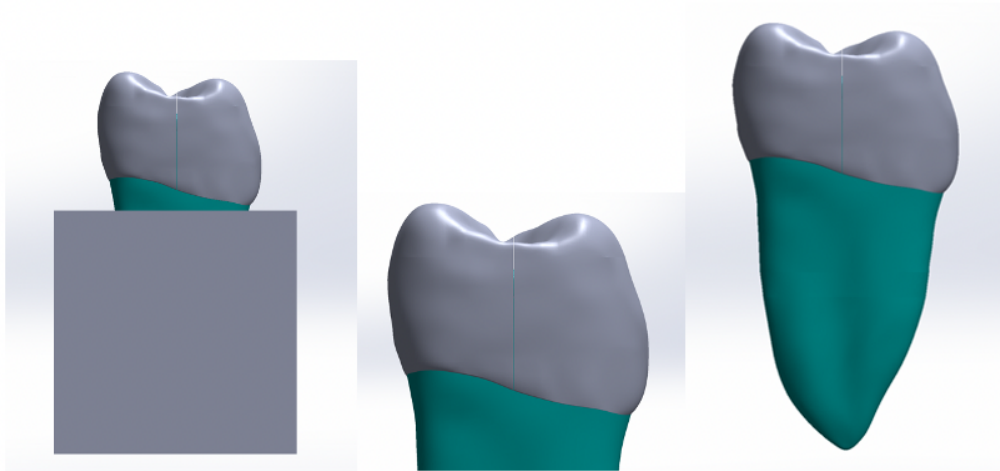
Figure 33: Mandibular second molar with complete fractured enamel.

Results and Discussion

The simulation considered scenarios of fully fractured enamel with short vertical cracks, specifically crack lengths of 1 mm, 3 mm, and 5 mm. The results from models with fully fractured enamel were compared to those without fully fractured enamel at the same crack lengths, as shown in Figure 34. For the 1 mm vertical crack in enamel, where the crack had not extended to the dentin, the blue curve illustrates the force versus time plot, while the gray curve represents fully fractured enamel with intact dentin. The comparison revealed similar maximum resultant force and curve shape, with the gray curve having a lightly longer run time, as expected due to the more severe damage of fully fractured enamel, which requires more time to dissipate the energy from percussion loading.

Moving to the 3 mm vertical crack, the orange curve represents crack in enamel and dentin, while the red curve shows the same crack length in dentin with fully fractured enamel. The orange curve shows a single peak and a bell-shaped curve, contrasting with the two peaks observed for the red curve. In addition, the fully fractured enamel in red curve resulted in a lower maximum force, indicating more substantial damage. Similar comparisons were made for the 5 mm vertical

crack, where the green curve represents the crack in both enamel and dentin, and the black curve represents the same crack length with fully fractured enamel. The green curve exhibited a bell-shaped curve with a flat peak and no second peak, while the black curve showed three peaks, signifying more severe damage when the enamel was fully fractured under the same crack length condition, because there are a greater number of peaks indicating more crack oscillation when enamel is fully fractured comparing to the same crack length without fully fractured enamel.
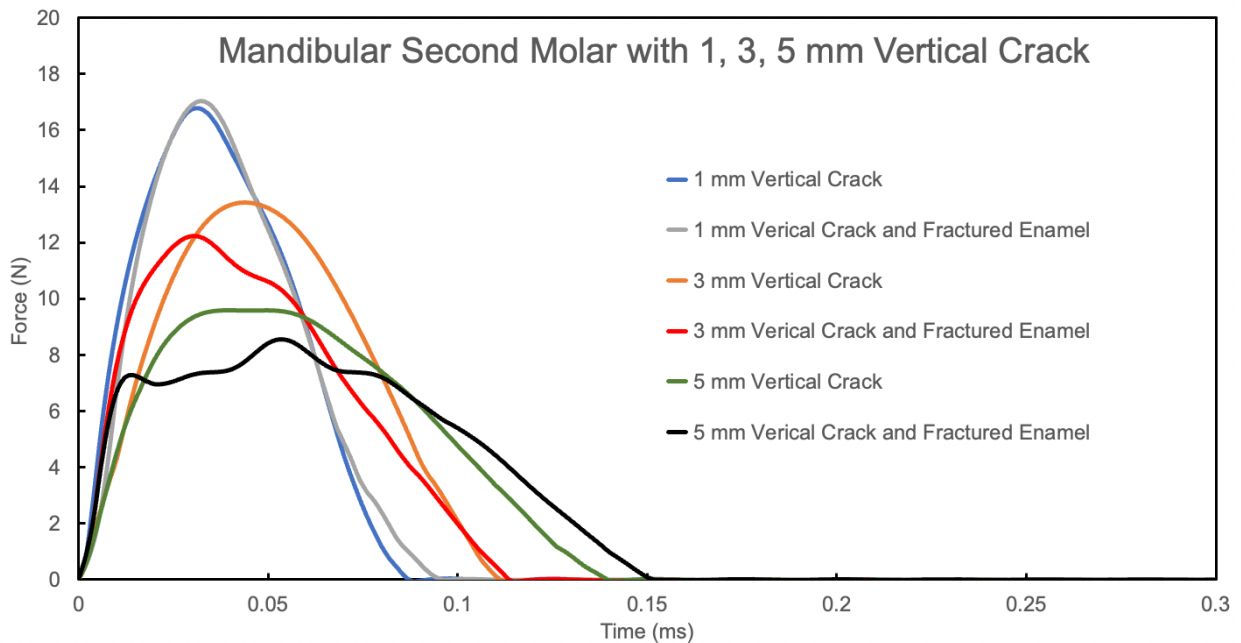
Figure 34: Force vs time plot for molar with 1 mm, 3 mm, and 5 mm vertical crack, with or without fully fractured enamel.

Overall, fully fractured enamel represents more severe damage compared to partial vertical cracks in enamel. These observations are reflected in the force versus time plot in Figure 34. Specifically, when the crack has not propagated into the dentin with a vertical crack length of 1 mm, the QPD may not be sufficient to detect a second peak, resulting in a response more akin to that of an intact tooth. However, for vertical cracks of 3 mm and 5 mm, the QPD is capable of easily detecting cracks, especially when the enamel is fully fractured.

After the various vertical crack lengths are investigated, damaged PDL is investigated along with the vertical crack condition. Since the damaged PDL often accompany with a long vertical crack when the crack tip extends below the PDL level to cause infections at PDL, so a 10 mm vertical crack molar model is picked for this study, the same tooth model used in Chapter 2. Different PDL moduli were examined to simulate different degree of damaged PDL around the tooth in the presence of a vertical fine crack in the molar. Figure 35 shows the resultant force versus time plots using various PDL moduli in FEA simulations to simulate different degree of PDL damage range from 0.0001 MPa to 0.1 MPa, representing the spectrum from extreme PDL damage to a healthy PDL. The gray curve illustrates the resultant force result when the PDL modulus is 0.1 MPa, representing healthy PDL. The green curve represents the resultant force at a PDL modulus of 0.05 MPa, the red curve at 0.01 MPa, the yellow curve at 0.005 MPa, the blue curve at 0.001 MPa and finally the orange curve at 0.0001 MPa, representing a severely damaged PDL.

In Figure 35, the plot illustrates the force versus time curves corresponding to various PDL modulus. A the PDL modulus decreases, the curve exhibits an escalating number of peaks, with a pronounced deepening of the first peak valley. Specifically, the gray and the green curves, corresponding to PDL moduli of 0.1 MPa and 0.05 MPa, respectively, showing two peaks with the time duration close to 0.2 ms. Subsequently, the red, yellow, and blue curves, reflecting PDL moduli of 0.01 MPa, 0.005 MPa, and 0.001 MPa, display three peaks. Furthermore, a substantial reduction in PDL modulus to 0.0001 MPa results in the orange curve displaying four distinct peaks. These findings highlight the influence of PDL modulus on the force versus time curve, indicating that a lower PDL modulus correlates with a greater number of peaks. Lower PDL modulus introduces more prominent first peak and deeper first peak valley. When the PDL modulus reduces

to sufficiently low value of 0.0001 MPa, peaks become distinct to each other. The overall phenomenon of a greater number of peaks and more prominent additional peaks resulting from lower PDL modulus is caused by the increased oscillation under the percussion loading, the concept discussed in previous chapters. Damaged PDL is simulated using lower modulus PDL in the model, result in decreasing the stiffness of the PDL and reducing the energy dissipation process, so that the overall time duration becomes longer.
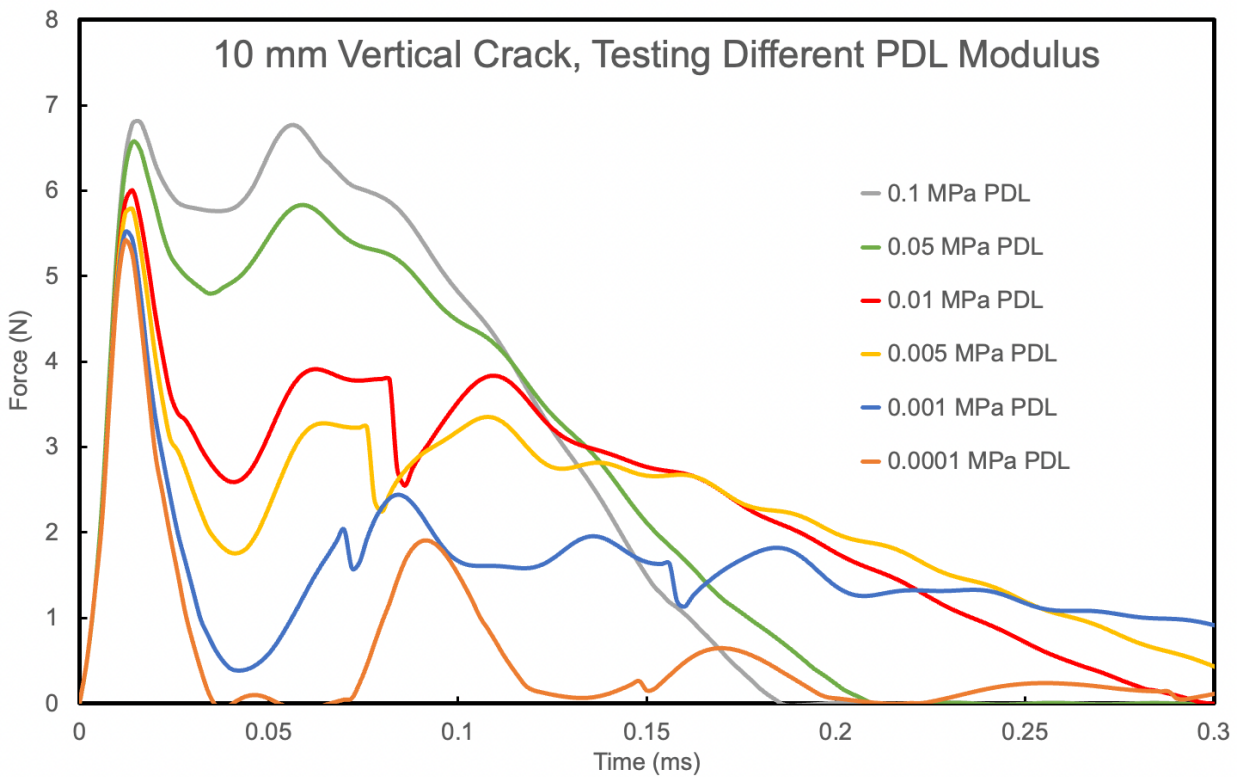
Figure 35: 10 mm vertical crack molar with damaged PDL, testing different PDL modulus in FEA simulations.

Analyzing the shapes of curve corresponding to different PDL moduli reveals distinct patterns. When a molar possesses a long vertical crack and relatively healthy PDL with moduli of 0.1 MPa and 0.05 MPa, the shape of curve feature tow connected peaks with similar amplitudes and shorter time duration of approximately 0.2 ms. Conversely, when PDL is moderately damaged with moduli of 0.01 MPa, 0.005 MPa and 0.001 MPa, the curve shapes exhibit three peaks, marked

63

by a high amplitude first peak followed by shallower and interconnected subsequent peaks. In cases of severe PDL damage with a modulus of 0.0001 MPa, the shape of the curve reveals four distinct peaks, characterized by a high amplitude peak succeeded by shallower additional peaks.

Conclusion

In conclusion, this Chapter extends the exploration initiated in Chapter 2 regarding vertical cracks in mandibular second molar. Utilizing FEA simulations, the study investigates the dynamic response of the molar under percussion loading condition, containing various vertical cracks, fully fractured enamel condition, and long vertical cracked molar with damaged PDL. Through simulations of vertical crack lengths ranging from 1 mm to 10 mm with or without fully fractured enamel, the results indicate the capability of the QPD in detecting vertical cracks beyond 3 mm, with enhanced prominence in multiple peaks when enamel is fully fractured at comparable crack lengths. The incorporation of damaged PDL alongside a 10 mm vertical crack reveals the relationship between reduced PDL moduli and an increased oscillation of peaks in the resultant force versus time plots, emphasizing the oscillation influenced by PDL stiffness. These findings contribute valuable insights for a comprehensive understanding of dental structure responses in varying clinical scenarios.

CHAPTER 4

FEA of Vertical Crack and Intact Replica Mandibular Second Molar

Introduction

The quantitative percussion diagnostics (QPD) serves as a reliable diagnostic tool detecting cracks in teeth. However, conducting controlled studies characterizing the QPD responses in cracked human teeth in vivo poses challenges due to the uncertainties associated to crack orientations, locations, and conditions. Additionally, it is challenging to diagnose and find cracked teeth in vivo. Thus, the objective of the current research is to establish a methodology using 3D printed replica teeth with biomimetic materials to simulate the QPD tests in vitro. The creation of replica teeth through 3D printing offers several advantages, primarily providing precise control over various crack types, locations, and conditions. These can be seamlessly integrated into CAD models and then 3D printed, simplifying the representation of defective teeth compared to clinical identification of natural tooth defects.

In this study, mandibular second molars with different vertical cracks were examined. Vertical cracks in replica teeth were induced through fatigue loading on the built-in notch in the tooth. The QPD tests were conducted on these simulated fatigue cracks using FEA, and the results were compared to the simulated QPD test data obtained from corresponding cracked natural teeth.

However, it is essential to acknowledge certain limitations in this study due to the 3D printing technique. One limitation arises from the crack gap space achievable in replica teeth. The minimum gap space feasible for 3D printing in the CAD model was 350 μm, while the minimum printed replica tooth gap space was 200 μm. This constraint is attributed to the resin's constraints during the 3D printing process. For example, when the crack gap space in the CAD model was set

at 300 μm, the resulting printed gap space was entirely bounded by the resin, resulting in no gap space at all.

Another limitation pertains to the material properties of the replica teeth. In a natural tooth, the enamel modulus is approximately 84 GPa, and the dentin modulus is around 15 GPa. However, the 3D printing resin material exhibits a modulus of only 10 GPa for both enamel and dentin. However, conducting FEA simulations for both natural teeth and replica teeth is imperative to discern the disparities between the force time plots of 3D printing replica teeth and natural teeth. A new 3D printing technique on dentin only model with crown delivery would achieve the most realistic tooth condition in terms of material properties.

Understanding the structures and properties of teeth is crucial for comprehending crack behaviors, and it is equally vital for accurately modeling FEA simulations. Enamel and detin components are primary sites for the occurrence of vertical cracks. Dentin being the largest structural component of human teeth, provides support to the enamel, preventing enamel fractures during occlusal loading. The dentin enamel margins play an important role in impeding crack propagation, thanks to their fracture toughness and cohesive properties.

Modeling Methods

The 3D printing CAD file of the replica teeth of mandibular second molar were made by the SOLIDWORKS (Dassault Systèmes SolidWorks Corp., Waltham, MA). The mandibular second molar tooth geometry is based on the computer tomography scan data provided by eHuman, InC. (Fremont, CA). The CAD model contains enamel and dentin with pulp chamber inside. Three different vertical notch lengths, 3 mm, 6 mm, and 9 mm were introduced to the replica teeth shown in Figure 37. These notches were implemented by extracting volumes from the intact tooth model,

resulting in 350 μm gap as shown in Figure 36 below. The vertical notches were oriented from mesial to distal.
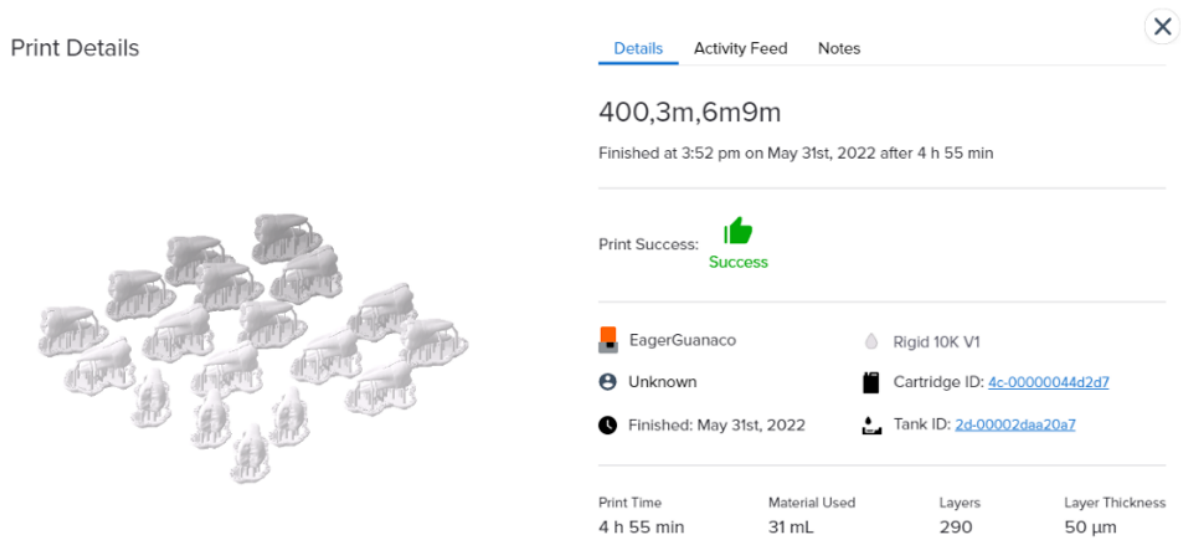
Figure 36: 3D printing details of replica teeth.
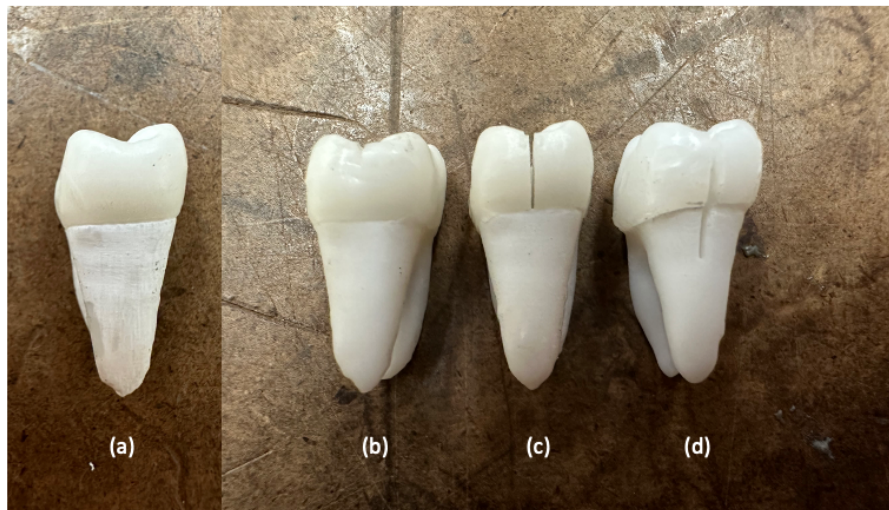
Figure 37: 3D printed replica teeth with different notch length. (a) intact, (b) 3 mm notch, (c) 6 mm notch, (d) 9 mm notch.

The CAD files of replica teeth with vertical notches were then imported into the 3D printing system as STL files to initiate the printing process. Printing was carried out using Formlabs, and the nesting process involved determining the optimal position and adding struts for printing. Upon sending the STL file to printer, the printing process took approximately 5-6 hours. After that, the

printed replica teeth were immersed in 99% isopropyl alcohol from Keystone Industry for 2 minutes with agitation to remove excess resin. The teeth were then transferred to the Form Wash (Formlabs), which also contained 99% alcohol, for a 30-minute wash to eliminate extra resin using vibration motions. Following this, the teeth were air-dried before being placed in the curing unit, Form Cure (Formlabs), for a 60-minute curing processes at 60 °C. Once complete, the struts were removed, rendering the replica teeth ready for use.

Despite the designed notch gap space is 350 μm, it was observed that the 3D printed replica teeth exhibited a gap space of only 200 μm, as measured by CT scan in Figure 38. The reduction in gap space within the vertical notch is attribute to the behavior of the 3D printing machine, which tends to close the gap before the resin is fully cured. As a result, for FEA models, the gap space for the replica teeth was adjusted to 200 μm to align with the actual measurements of replica teeth.
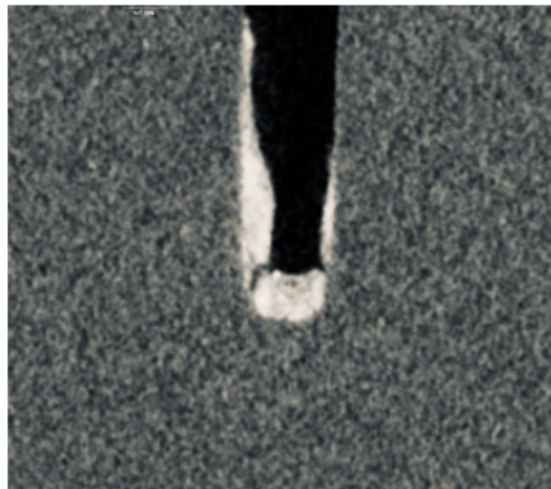
Figure 38: Micro-CT image of notch tip.

Following the 3D printing of replica teeth featuring vertical notches, fatigue testing was conducted to form fatigue crack shown in Figure 39. Once the fatigue crack is formed, NanoCT scans were employed to examine the replica teeth, revealing the formation of additional fatigue cracks at the vertical notch tips, as shown in Figure 38. The fatigue crack length measured

approximately 200 μm in length, with a crack gap space about 10 μm. Therefore, three fatigue

cracks were introduced into CAD models representing different vertical notch lengths of replica

teeth. The first model featured a 3 mm vertical notch with a 200 μm gap space and a 200 μm

fatigue crack with a 10 μm gap space. The second model had a 6 mm vertical notch with 200 μm

gap space and a 200 μm fatigue crack with a 10 μm gap space. The third model of replica tooth

had a 9 mm vertical notch with a 200 μm gap space and a 200 μm fatigue crack with a 10 μm gap

space. These CAD models containing both vertical notches and fatigue cracks, were imported into

FEA for simulations. In Figure 37, the corresponding replica teeth are printed and then fatigue

tested to generate 3 mm, 6 mm, and 9 mm vertical cracks. The FEA models included enamel and

dentin, but also contain PDL, bone and percussion rod. PDL and bone simulates the real tooth in

vivo while the percussion rod acts as the tool for measuring percussion loading. The resultant force

generated in the percussion rod was measured, and FEA generated the result of force time plot

under percussion loading conditions.
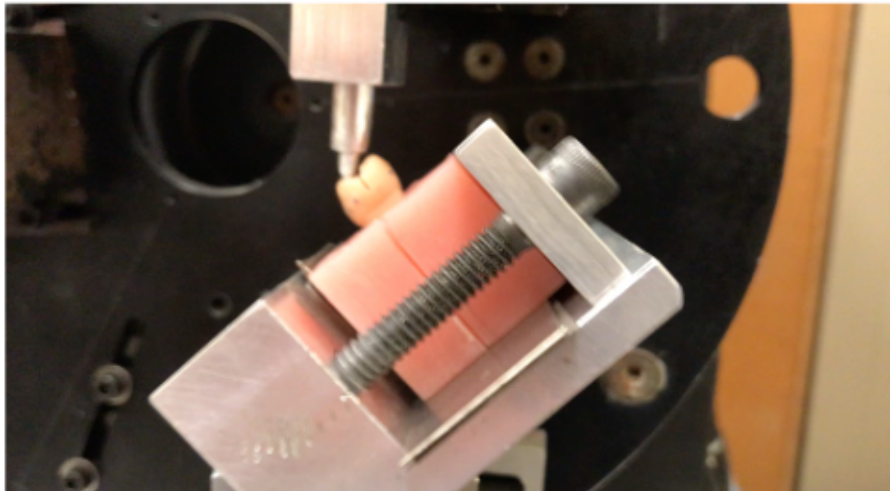
Figure 39: Fatigue testing.

The replica teeth include the enamel and dentin were 3D printed using Rigid 10K resin

from Formlabs, and each layer measuring 50 μm in thickness. This resin is rigid, strong, and glass-

filled reenforced, making it the stiffest resin in Formlab's portfolio. As per Formlabs's material property data, the modulus of the UV cured Rigid 10K resin is 10 GPa. This means that the 3D printed replica teeth have the modulus of 10 GPa for both enamel and dentin components. In contrast, natural teeth enamel possesses a modulus of 84.1 GPa, while dentin has a modulus of 10 GPa. Therefore, the dentin modulus of the 3D printed replica tooth is 4.7 GPa lower than that of natural teeth, and the enamel modulus of the 3D printed replica tooth is approximately eight times lower than that of natural teeth. These moduli are implemented to each tooth components in FEA simulations. In the FEA of replica teeth with fatigue cracks, a damage zone was implemented at the crack tip, representing 10% of Young's modulus of the undamaged region for both enamel and dentin components.

Results and Discussion

Figure 40: Percussion response of replica mandibular second molar with 3 mm vertical straight notch and 200 µm gap space, with or without fatigue crack, natural tooth property vs rigid 10K property.

The FEA models of 3 mm vertical straight notch, both with or without a 200 μm fatigue crack, were simulated using natural tooth properties and rigid 10K properties. The resulting force time plots are presented in Figure 40, where the yellow and blue curves present the performance of vertical notched FEA models utilizing natural teeth material properties. The yellow curve represents the 3 mm vertical notch with 200 μm gap without fatigue crack. The blue curve represents the 3 mm vertical notch with 200 μm fatigue crack, which the fatigue crack has 10 μm gap, and with 10% modulus in the damage zone. The black and gray curves represent force time plot of vertical notched FEA models using rigid 10K properties in the model, where both dentin and enamel moduli are set to 10 GPa. Specifically, the black curve represents the 3 mm vertical notch with 200 μm gap without fatigue crack. The gray curve represents the 3 mm vertical notch with fatigue crack.

In general, the 3 mm vertical notch without fatigue crack (yellow and black curves) show force time plot with only one peak, no additional peak detected, aligning with the FEA result of an intact molar from Chapter 2. However, model results using rigid 10K properties indicate a longer time duration of about 0.15 ms, an increase of 0.05 ms compared to the FEA model using natural tooth properties. Additionally, the maximum force of the FEA model using rigid 10K properties is approximately 10 N, which is 6 N less than the FEA model using natural tooth properties. These variations are expected due to the reduced moduli in enamel and dentin for replica teeth, resulting in a diminished overall stiffness that requires more time for the dissipation of percussion kinetic energy, leading to a longer time duration and lower peak amplitude. A comparison between models with and without a fatigue crack, represented by yellow and blue curves, reveals a lower peak amplitude in the presence of a fatigue crack. This decrease is attributed to the fatigue crack acting as a defect in the system, dissipating more energy during crack oscillation. Additionally, the fatigue

71

crack includes a damage zone at the notch tip, influencing the curve's shape with a shallow bump at the blue curve's downslope due to the crack oscillation, which is the same contact discussed in previous chapters. A similar observation of reduced peak amplitude accompanying a fatigue crack is also evident in the black and gray curves using rigid 10K properties.
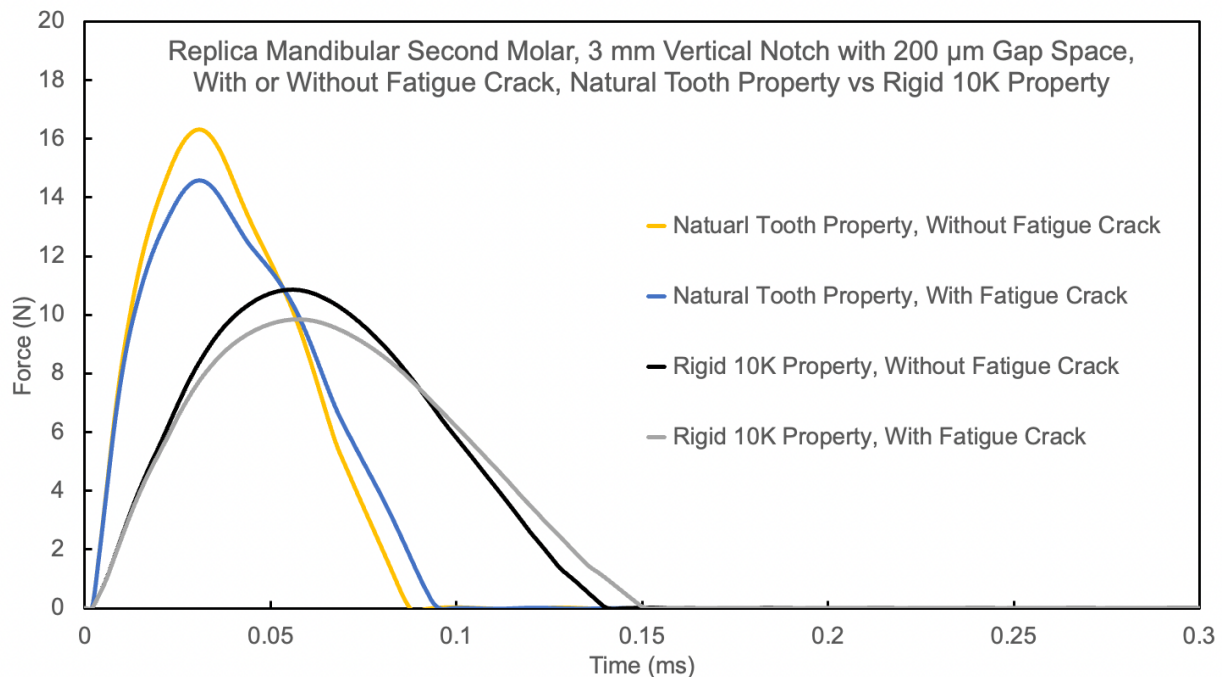

Figure 41: Percussion response of replica mandibular second molar with 6 mm vertical straight notch and 200 μm gap space, with or without fatigue crack, natural tooth property vs rigid 10K property.

The results shown in Figure 41 represents the force versus time plots for a 6 mm vertical notch, both with or without the 200 μm fatigue crack, using natural tooth properties and rigid 10K properties. The yellow and blue curves represent the FEA results incorporating natural tooth properties, where the yellow curve illustrates the 6 mm vertical notch FEA model without a fatigue crack, and the blue curve displays the result with a fatigue crack. Meanwhile, the black and gray curves represent the results using rigid 10k properties in dentin and enamel. Specifically, the black

curve corresponds to the replica tooth without a fatigue crack, while the gray curve shows the result with a fatigue crack.

Upon comparing the scenarios with or without fatigue crack while employing natural tooth properties, the yellow curve shows a peak with high amplitude and a small second peak, whereas the blue curve displays multiple peaks, similar to the results discussed in Chapter 2, where clinical data validate that the curve's shape for a vertical cracked molar aligns with this blue curve rather than the yellow curve. This comparison proves that a vertical notch in a replica tooth is insufficient to emulate the vertical crack condition; the introduction of a fatigue crack, complete with a damage zone at the crack tip, is crucial to accurately represent the most realistic vertical crack in a tooth. Furthermore, when assessing the black and gray curves using the rigid 10K properties, the gray curve demonstrates two peaks, contrasting with the black curve that exhibits only one peak. This observation further proves the crucial role of the fatigue crack and damage zone in capturing the prominent peaks in the vertical crack scenario.

Transitioning to the analysis of the 9 mm vertical cracked molar, Figure 42 provides force versus time plots expressing scenarios with or without fatigue crack, using both natural tooth and rigid 10K properties. The yellow curve corresponds to the outcome without a fatigue crack and with natural tooth properties, while the blue curve represents the result for the same model but with a fatigue crack. Furthermore, the black curve illustrates the result without a fatigue crack using rigid 10K properties, and the gray curve shows the result for the same model but with a fatigue crack.

The shapes of the curves for black and gray curves using rigid 10K properties in Figure 42 closely resemble those of the black and gray curves in Figure 41. The notable difference lies in the time duration of the 9 mm vertical crack model in Figure 42, which is approximately 0.05 ms

longer than the time duration of the 6 mm model in Figure 41. This extension in time duration aligns with expectations, considering the increased crack length, which requires a longer duration to dissipate all the energy. Despite the yellow curve representing the scenario without a fatigue crack in Figure 42 displaying multiple peaks, these additional peaks are not as prominent when compared to the blue curve. The blue curve clearly shows two prominent peaks, consistent with the results discusses in Chapter 2.
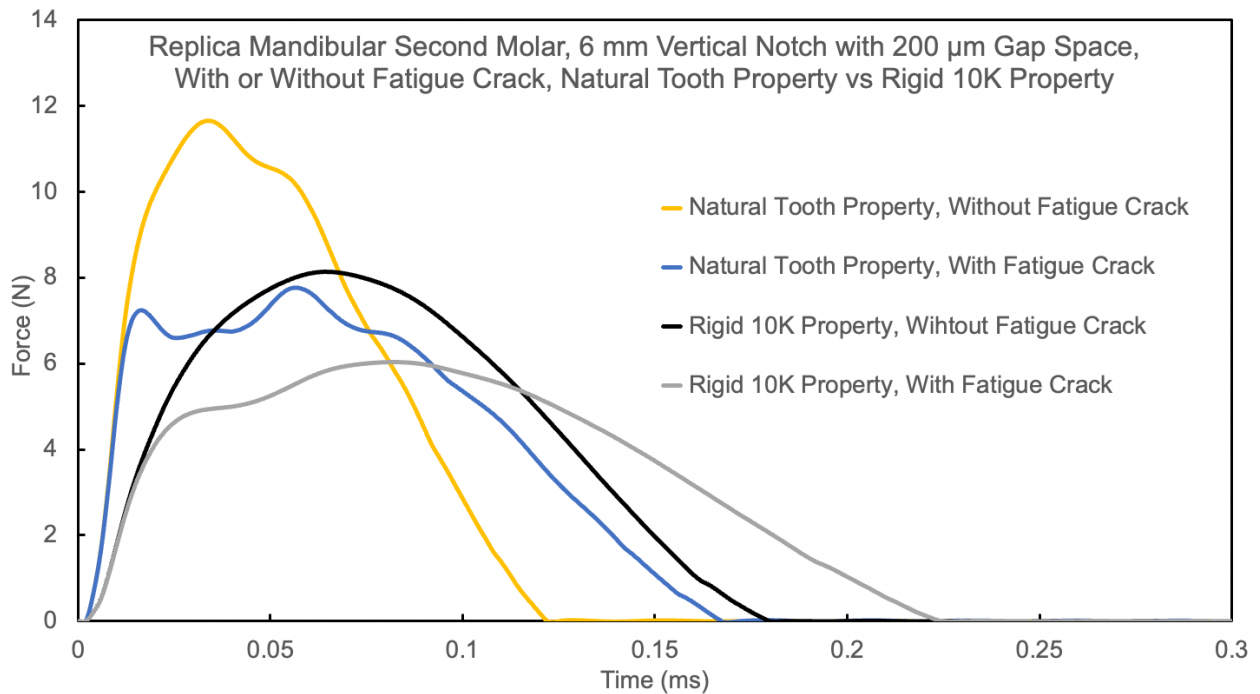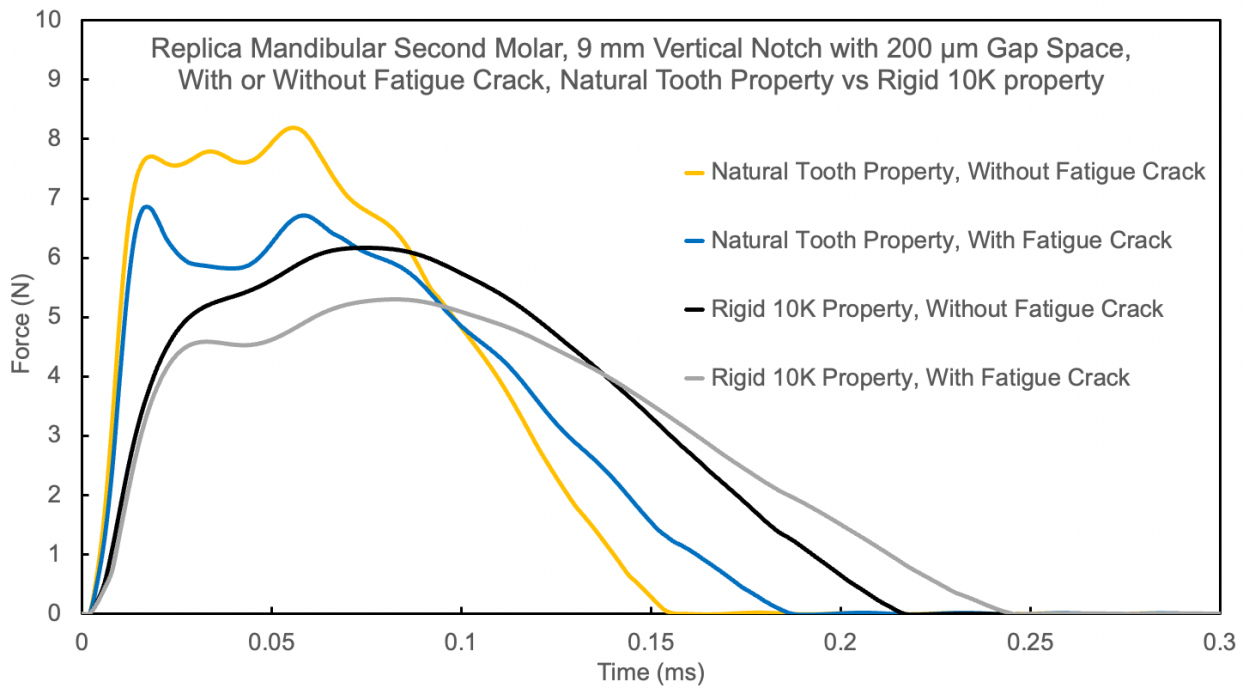

Figure 42: Percussion response of replica mandibular second molar with 9 mm vertical straight notch and 200 μm gap space, with or without fatigue crack, natural tooth property vs rigid 10K property.

Conclusion

In summary, this research introduces a novel methodology employing 3D printed replica tooth to simulate the QPD tests in vitro. Overcoming challenges associated with in vivo studies on vertical cracked teeth, 3D printing provides precise control over crack types, locations, and conditions in replica teeth. Despite inherent limitations in achieving crack gap spaces and

variations in material properties compared to natural teeth, the study contributes significantly to understanding crack behaviors and aids in accurate FEA simulations.

The modeling methods involving CAD designs, Formlabs for 3D printing, and fatigue testing allowed the creation of fatigue cracks based on the printed vertical notches in molar. Results and discussions unveiled the response of replica teeth and natural teeth to percussion loading, showing variations of shape of curves, peak amplitudes, and time durations on force time plot. Observations includes the influence of fatigue cracks on peak amplitudes and number of peaks, emphasizing the importance of introducing realistic defects in the form of fatigue cracks in replica teeth to accurately represent vertical crack scenarios. Despite challenges, this research forms a crucial step in advancing our understanding of tooth responses to percussion loading in controlled environment, contributing valuable insights to the broader field of dental diagnostics.

CHAPTER 5

FEA of Apical Root Crack for Mandibular Second Molar

Introduction

Preserving natural teeth and ensuring their health are paramount concerns in dentistry. However, diagnosing apical root cracks in teeth remains a complex and challenging task. Apical root cracks also known as vertical root fractures (VRFs) primary affect in the root region of natural teeth, often got attention from dental professionals and researchers. Accurate diagnosis of VRFs becomes crucial and this research explores the application of Finite Element Analysis (FEA) to simulate the QPD test on a mandibular second molar with a VRF. The objective is to determine if the QPD method can effectively defect VRF and to comprehend the complexity of the QPD results associated with this specific VRF condition. A comprehensive understanding of a VRF is vital for preserving dental functions and ensuring the success of endodontic treatments.

VRFs are more commonly associated with root-filled teeth. Research studies have found a significant percentage of teeth extracted due to VRF, with a substantial majority being root-filled teeth. In the study done by Yoshino et al, it was found that 31.7% of teeth (total of 736 teeth) were extracted due to apical root crack, that 93.6% were root filled teeth. [37] Another similar study conducted by Sugaya et al. found that 97% of the detected VRFs among total of 304 teeth were root filled teeth, detected clinically and/or radiographically. [38] There are many factors or combinations of factors associated with the development of VRFs, and there are many research articles out there were investigating different factors. Some common factors include biomechanical properties change, root canal morphology, occlusal force, and endodontic treatment techniques. For example, biomechanical changes resulting from dehydration within the detin matrix around the root canal and pulp chamber can lead to reduced fracture toughness, increased

susceptibility to fatigue failure, decreased microhardness, and poorer dissipation of occlusal forces.[39] Some studies found the root canal morphology that roots with two canals connected by an isthmus were more vulnerable to VRF than roots with a single root. [40] Lastly, the endodontic treatment procedures may lead to VRF, as the study found the loss of sound dentine at peri-cervical dentine during traditional accessing cavity and root canal preparation may predispose the residual tooth structure to fracture. [41]

Accurate diagnosis of VRF proves challenging due to absent of clinical signs, and conventional radiographic assessments are often inconclusive. [42] A VRF may be investigated either by surgical exploration in vivo or by careful examination after extraction in vitro. On one hand, surgical exploration is limited to visual examination of the buccal side of the tooth, missing VRF assessment to mesial and distal side of the tooth. On the other hand, post-extraction examination cannot definitively confirm VRFs during the extraction process, because VRF can be caused unintentionally during the extraction process. [42] Current clinical examination often relies on CBCT for identifying VRFs. However, due to the radiation restriction, the resolution of the CBCT is about 5 μm voxel size. [43] While CBCT results may not reliably defect VRFs, they can reveal the pattern of bone loss and damaged PDL, which typically associated with VRFs.

A few studies have shown that premolar and molar teeth are most frequently affected by VRF. [44]–[46] PradeepKumar and coworker's study found mandibular molars has 34% and maxillary premolars has 22.8%, they were most frequently affected teeth. [44] Cohen et al's research results also indicated that mandibular molars and maxillary premolars are statistically more prevalent with VRFs. [46] Karygianni and colleages showed that women (64.06%) presented VRFs more frequently than men (35.94%) at the mean age of 51.1 and 55.1 years, and majority of teeth (64.06%) with VRFs had undergone the combination of conventional root canal retreatment

and apical surgery. [45] Given these findings, this research focuses on the mandibular second molar tooth with VRF. It was modeled, meshed, and simulated using FEA.

Modeling Methods
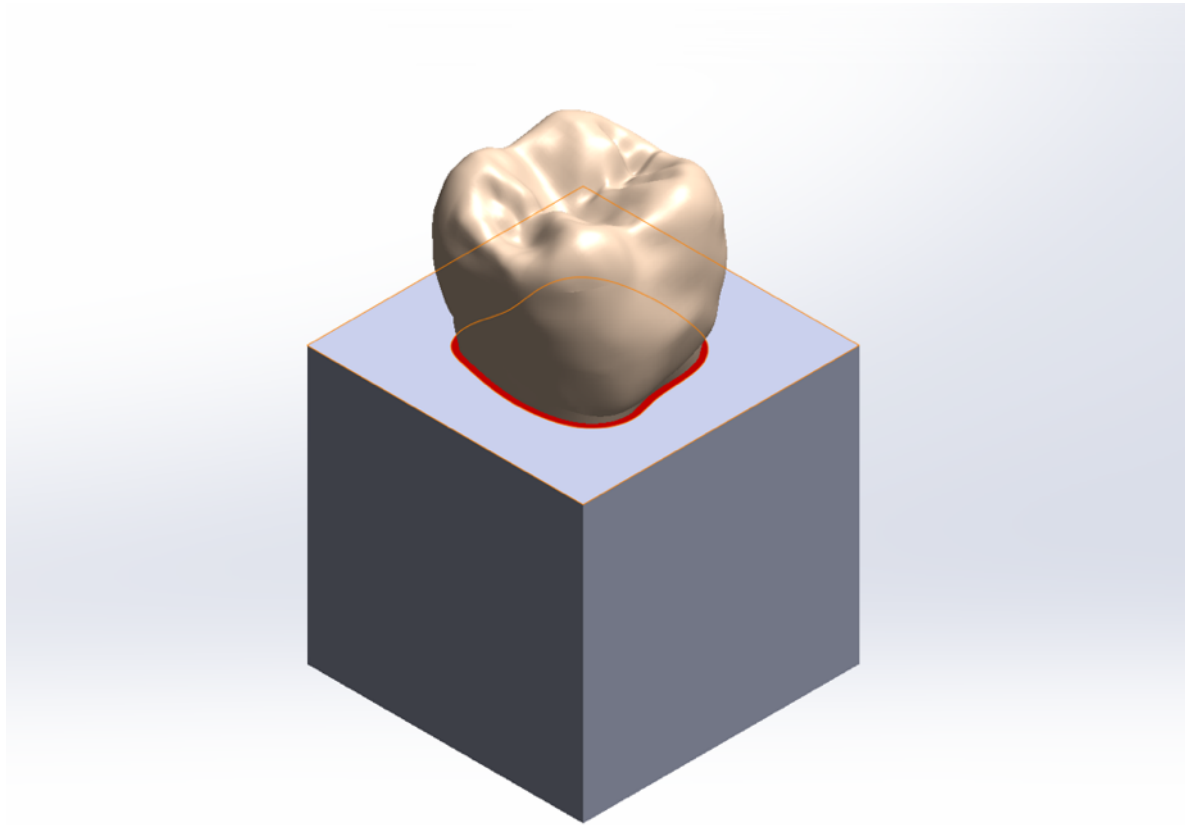
Figure 43: Mandibular second molar 3D model.

The mandibular second molar was selected for simulating VRF tested by the QPD using FEA. The tooth model is derived from the computer tomography obtained from eHuman, Inc, was constructed using Solidworks (Dassault Systemes). The comprehensive 3D model includes enamel, dentin with pulp chamber and root canal, PDL and surrounding bone. Figure 43 visually represent this 3D model of the mandibular second molar with all tooth components. The cubic shaped bone surrounds tooth's roots, with the red PDL in between the tooth and the bone. The thickness of the

PDL is 0.2mm, which is consistent with the literature published earlier. [32] The design includes

the percussion rod and tip to facilitate the QPD test simulation.
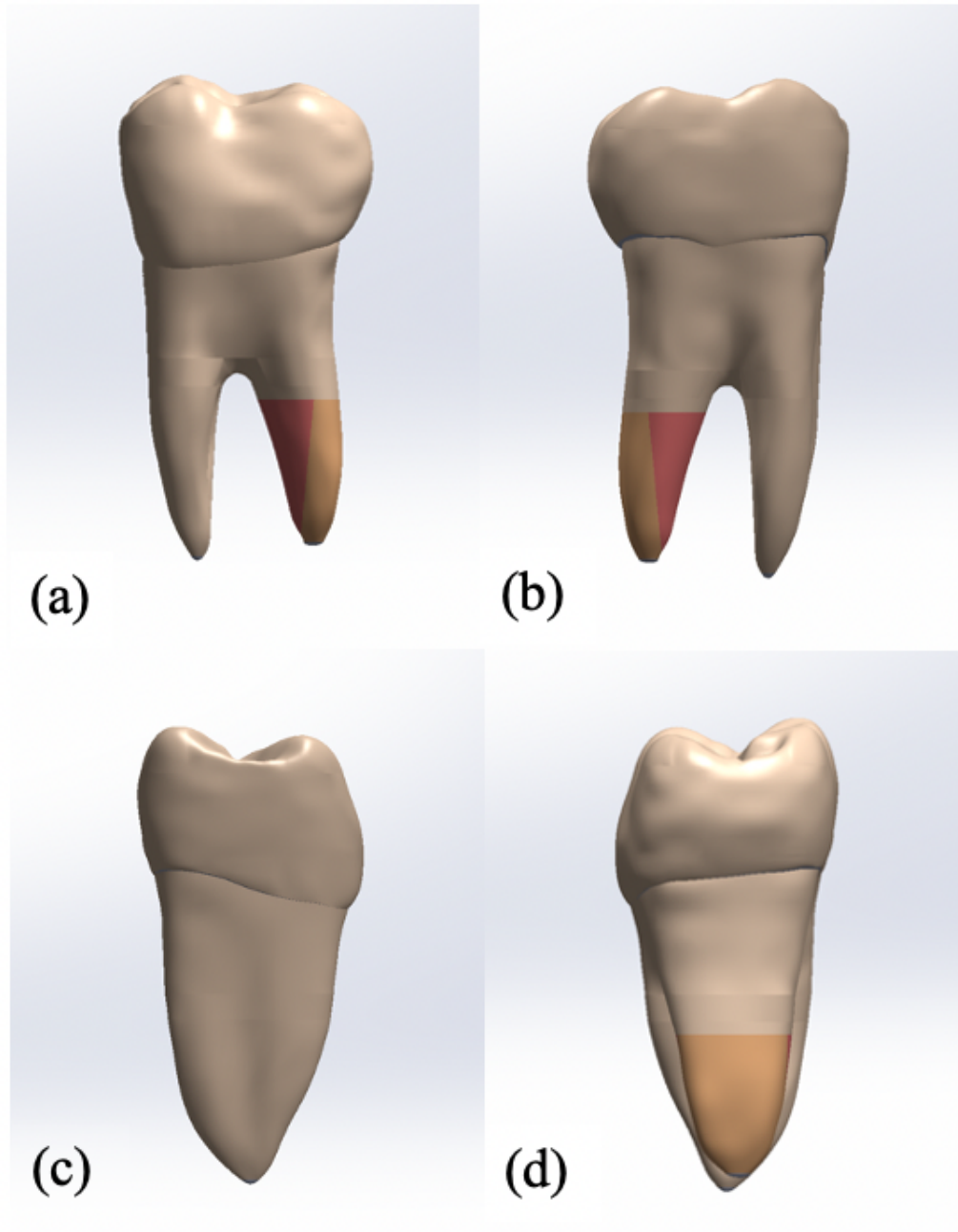
Figure 44: Mandibular second molar with 6 mm VRF. (a) Buccal view, (b) Lingual view, (c) Mesial view, (d) Distal view.

Once the tooth model is crafted based on the CT data, a VRF is intentionally created at the

root apex on the distal side of the tooth. This simulated VRF extends vertically along the root canal

toward the occlusal surface of the tooth, mirroring prevalent clinical conditions observed in various literatures. [38], [42], [47], [48] Figure 44 provides various views of the mandibular second molar, revealing the VRF's feature, including buccal view, lingual view, mesial view, and distal view. The VRF is situated on the distal side of the root, initiating from the apex and extending vertically up toward the occlusal surface of the tooth. The length of the VRF in this model is 6mm, as indicated between the red and yellow cracked body. The completed molar model undergoes meshing using MSC Apex, generating finite elements with nodes. Lastly, FEA simulations are executed using MSC Marc software.

Material properties are consistent with the previous study, [32] are imported into MSEC Marc for both tooth components and percussion system. Damping properties applied the same as the previous study and detailed explanation of using Rayleigh damping can be found in previous study. [32] Specific adjustments are made to material properties in this study due to the VRF condition. For instance, the PDL modulus is reduced to simulate damaged PDL accompanying the VRF condition. Additionally, the reduced modulus of dentin is implemented at the crack tip region to replicate the damage zone.

Results and Discussion

The teeth clinically examined exhibited a vertical distal pulpal root crack, as depicted in Figure 45, and underwent the QPD testing in 2012. The same tooth underwent a follow-up QPD examination in 2014, with the normalized energy results presented in Figure 46. Both clinical assessments comprise ten taps on the same cusp of the tooth, and the results are graphed in normalized energy, focusing on the curve's shape. The normalized energy is derived from the square of resultant percussion force, measured by the force sensor in the percussion rod when tapping the tooth's buccal surface.

In both Figure 45 and Figure 46, the curve exhibits high frequency peaks with a peak width of approximately 0.05 milliseconds. Notably, the 2014 results show a slightly wider peak width than the 2012 results. The total time duration is also longer in the 2014 results compared to the 2012 results. Moreover, the amplitude in Figure 46 surpasses that of Figure 45. A discernible difference between two clinical tests lies in the distinct peaks observed in the 2012 test, while the 2014 test displays connected peaks. In addition, it appears that the 2014 test introduces a fifth peak at 0.35 milliseconds.

Figure 47 illustrates the FEA result. The FEA normalized energy return plot based on the resultant force is collected by the percussion rod system, similar to the clinical findings. It depicts high frequency peaks with peak width of around 0.05 milliseconds, featuring a total of five peaks. The FEA results align closely with the clinical observation, providing valuable insights into the tooth's dynamic response under percussion loading conditions.
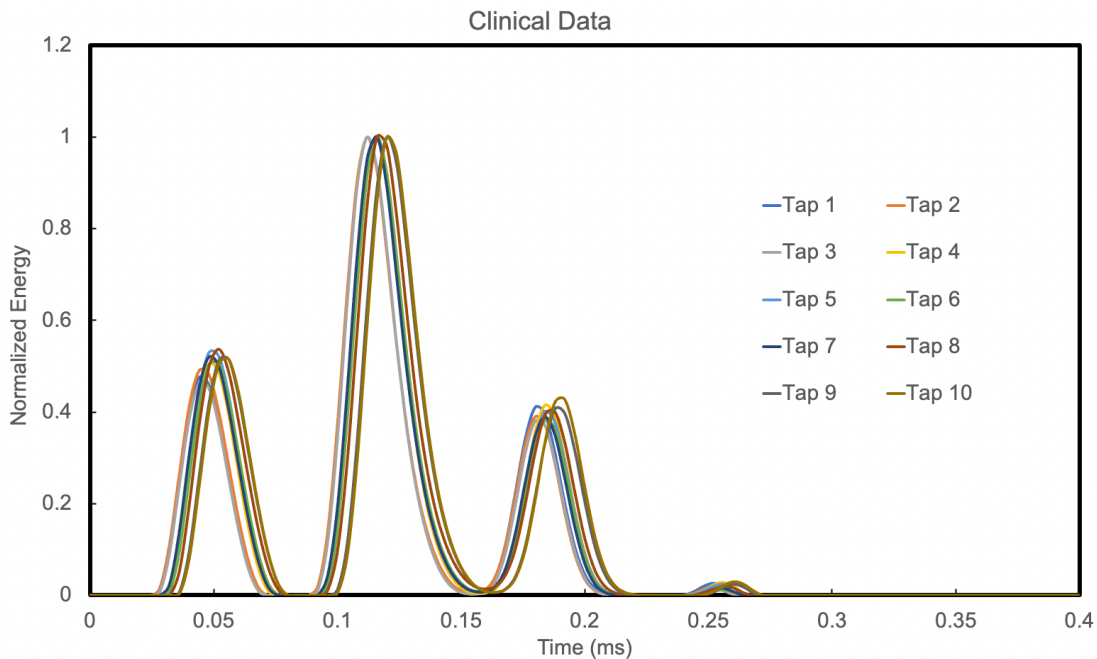
Figure 45: Normalized energy plot of a clinical tested tooth with VRF, tested in 2012 with 10 QPD taps.
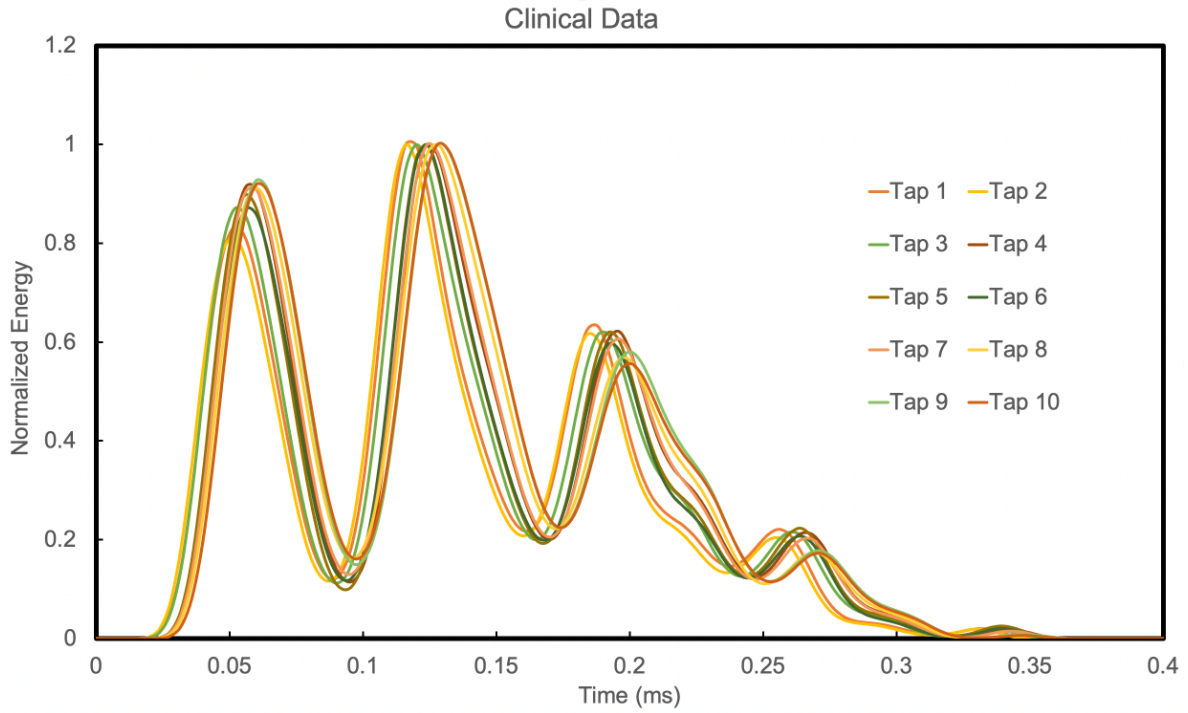
Figure 46: Normalized energy plot of a clinical tested tooth with VRF, tested in 2014 with 10 QPD taps.
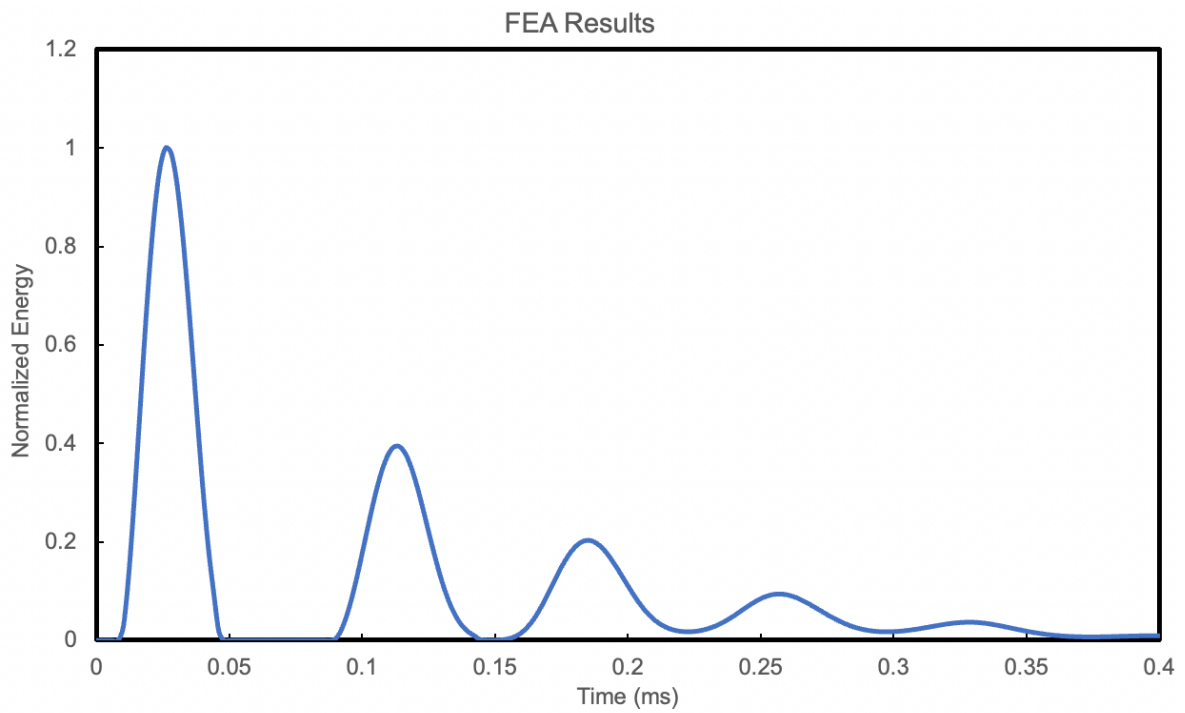
Figure 47: Normalized energy plot of a FEA result for a molar with VRF.

Conclusion

In conclusion, the comprehensive examination of mandibular second molar with VRF was conducted through both clinical tests and FEA. This research provided valuable insights into the response under percussion loading conditions. The clinical tests in 2012 and 2014 revealed high frequency peaks on the plot. The FEA simulations, designed to replicate the clinical QPD, closely match the clinical observations. The FEA normalized energy plot also displayed multiple high frequency peaks. This study demonstrates the significance of employing FEA to conduct clinical assessments. The ability of FEA to replicate this clinical QPD test scenarios, considering factors like biomechanical material properties, the presence of micro gap defects, damage zone at the crack tip and damaged PDL by adjusting the material properties in tooth components. Furthermore, this study proves the accurate detection of VRF by the QPD, so that future clinical QPD diagnosis can be optimized and refined.

CHAPTER 6

FEA of Damaged PDL for Mandibular Second Molar

Introduction
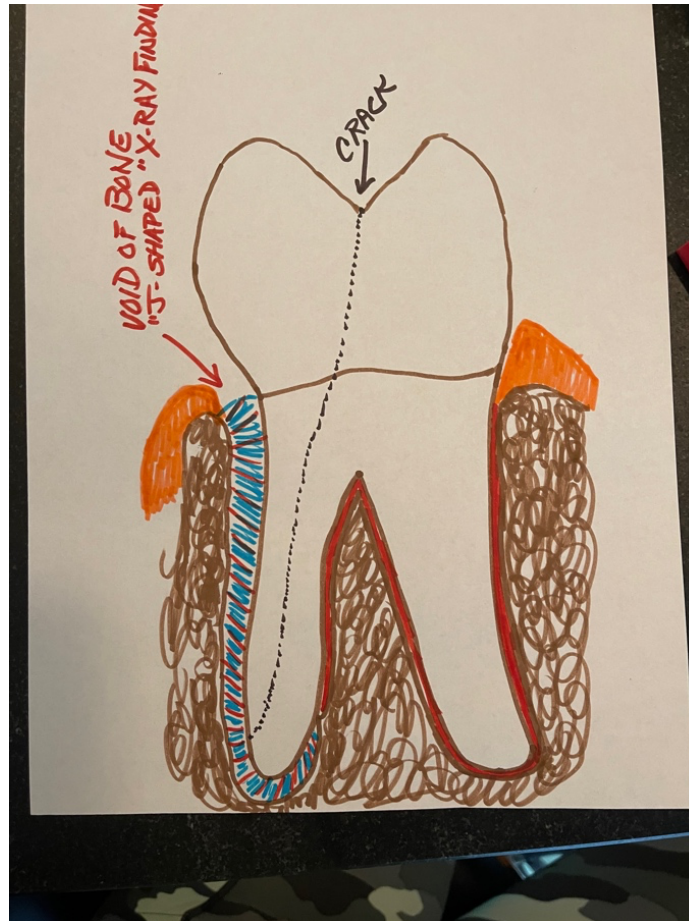
Figure 48: Drawing of J shape PDL damage due to the periodontal and endodontic lesions, which is commonly seen in cracked tooth or intact tooth.

Periodontal diseases are frequently identified in dentistry, often detected as J shape damage

on the periodontal ligament (PDL) as illustrated in Figure 48. Such damage is typically caused by

the periodontal and endodontic lesions. Simon and coworkers classified periodontal lesions based

on the pathology of origin. [49] Based on their classification of lesions shown in Figure 49 in

instances where the tooth is still intact, the J shape PDL damage associated with primary

periodontal lesions, originates from the marginal periodontium. These lesions evolve due to unchecked progression of periodontal disease along the root surface until researching the apical region. [49] Diagnosis relies on standard periodontal tests, often detecting periodontal attachment loss through X-ray radiographs and identifying wide periodontal pockets. Apical pathology is typically not radiographically visible in these cases. [50]
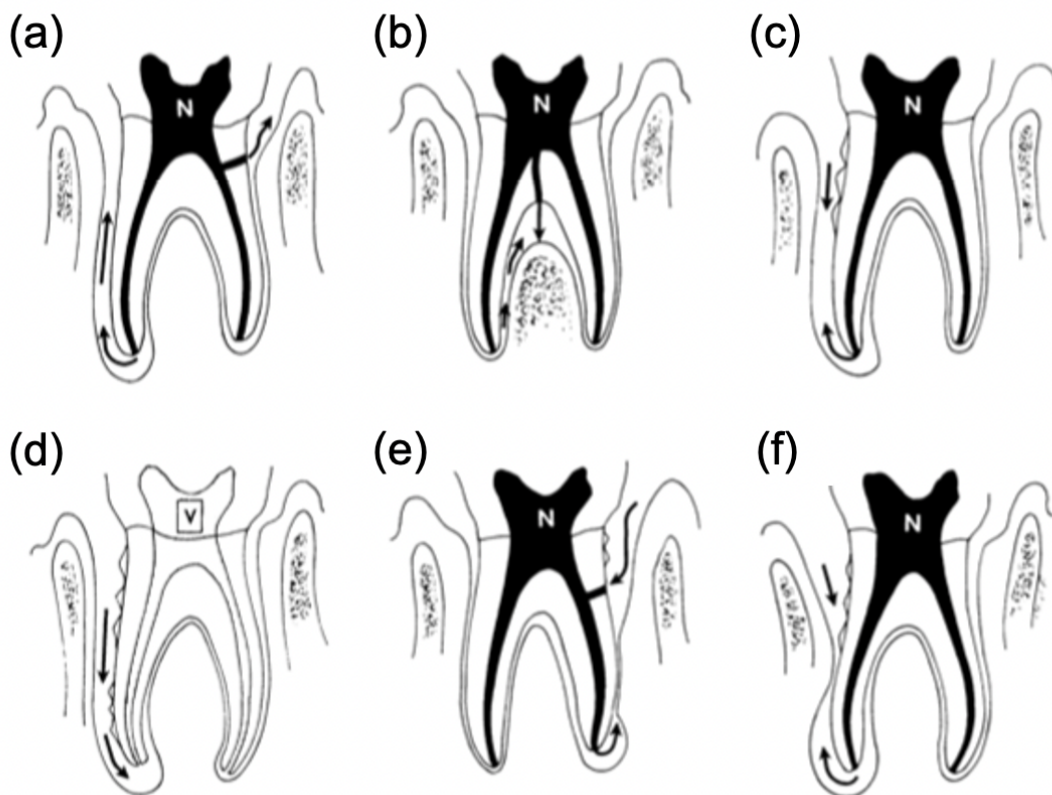
Figure 49: (a) Endodontic lesions. The pathway of fistulation is evident through the periodontal ligament from the apex or a lateral canal. (b) Fistulation through the apex or a lateral canal may cause bifurcation involvement. (c) Primary endodontic lesion with secondary periodontic involvement. The existing pathway as in a is shown but with the passage of time periodontitis with calculus formation begins at the cervical area. (d) Periodontic lesions. This is the progression of periodontitis to apical involvement. Note the vital pulp. (e) Primary periodontic lesion with secondary endodontic involvement. The primary periodontic involvement at the cervical margin and the resultant pulpal necrosis once the lateral canal is exposed to the oral environment result in this picture. (f) "True" combined lesions. The two separate lesions are heading to a coalescence which forms the "true" combined lesion.[49]

Clinical findings of primary periodontic lesions, as shown in Figure 50, indicate J shape damaged PDL detected through X-ray results.[49] The research focuses on FEA simulations of the QPD when J shape damaged PDL is present around a defect free mandibular second molar. It is shown by the dark region around the left side of the tooth in Figure 50. This research topic studies the FEA simulations of the QPD when the J shape PDL damage is present around the defect free mandibular second bicuspid. While primary periodontal lesions in Figure 49, closely resemble the clinical cause for the modeled J shape damaged PDL in FEA, other causes in Figure 49 can also result in similar damage. Examples include endodontic lesions, primary endodontic lesions with secondary periodontic involvement, and true combined lesions. However, this research does not delve into the causes of J shape damaged PDL. Instead, it discusses the FEA QPD simulation results for this condition, comparing them with the clinical QPD results of J shape damaged PDL.
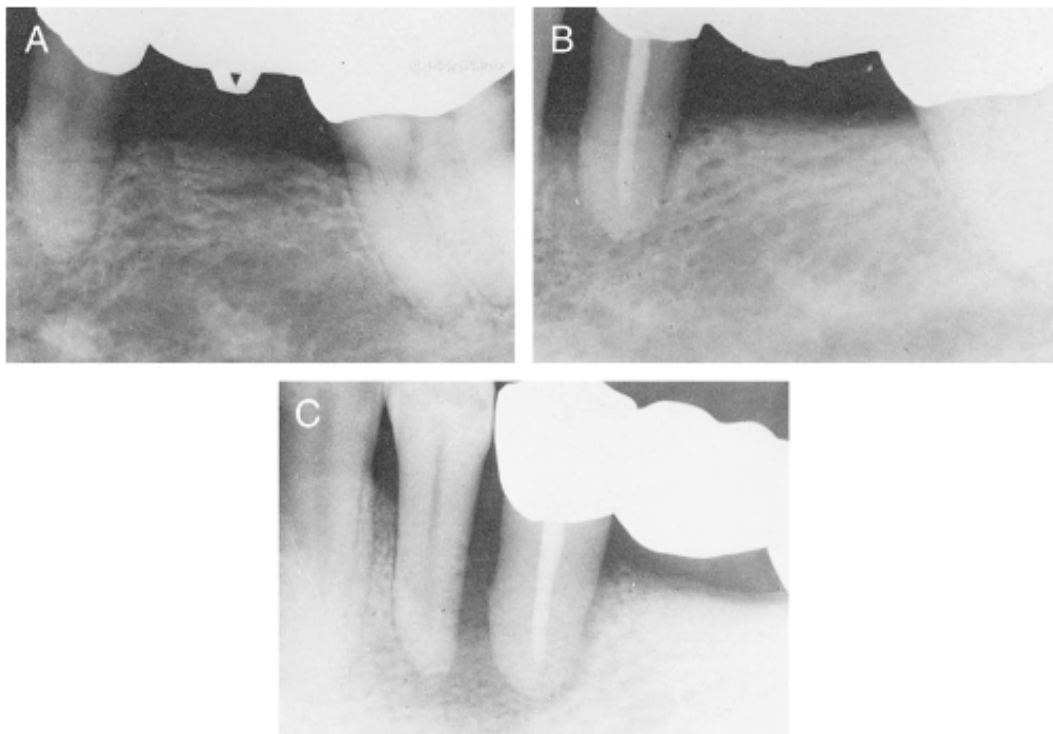
Figure 50: Clinical X-ray findings of primary periodontic lesions.

Figure 51: X-ray of mandibular molar with PDL lesion at one the root's apex.
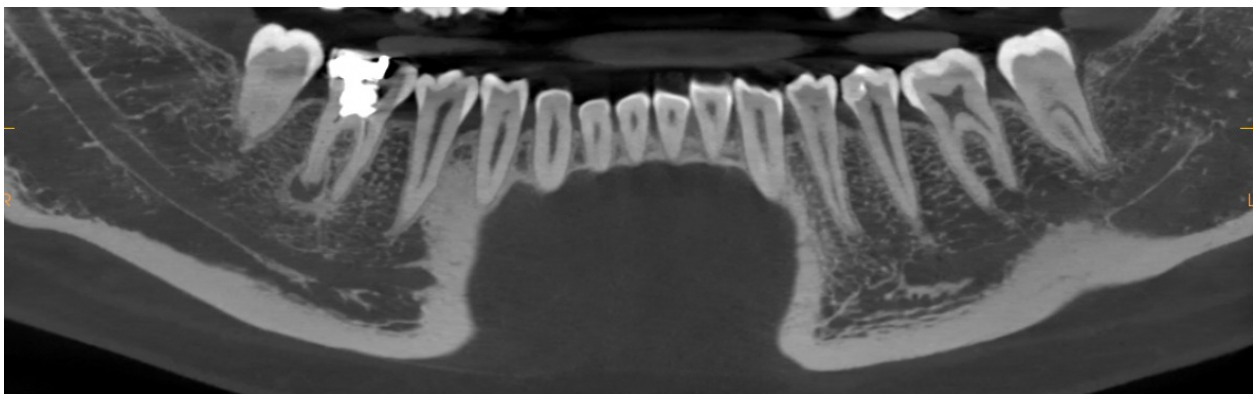
Figure 52: CBCT test result of mandibular second molar which indicated periodontic and endodontic lesion at tooth apex.

Beyond the J shape damaged PDL clinical condition, another PDL lesion condition associated to tooth number 30 (mandibular molar) was clinically discovered through X-ray shown in Figure 51 and Cone Beam Computed Tomography (CBCT) shown in Figure 52 at Sheets, Paquette & Wu Dental Practice Newport Beach. The tooth is then tested by the QPD. The x-ray image reveals an empty chamber underneath the distal side of the root's apex, indicative of a periodontal and endodontic lesion. The CBCT scan provided a three-dimensional perspective, showing a dark, empty spherical space at the tooth apex, which is shown in Figure 52. The distal-

mesial view in the second figure of Figure 52 of the CBCT scan shows the additional perspective of the lesion condition at the tooth apex. Patient history indicated endodontic treatment performed over two years ago, without the delivery of a crown. The root canal buildup became loose and defective, leading to bacterial infiltrations and subsequent PDL damage and bone absorption. Although asymptomatic, this lesion could potentially worsen and cause significant pain in the future. As a result, the dentist recommended redoing the endodontic treatment and placing a crown. This periodontal and endodontic lesion condition was implemented into the CAD model for FEA simulations, and the results will be discussed later and compared with the clinical QPD results for validation.

Modeling Methods

In this study, intact mandibular second molar models were utilized. During the CAD modeling phase, the J shape damaged PDL was generated by selectively removing portions of the PDL, creating a J shaped pattern, and absorbing it from the surrounding healthy intact PDL. The modeling and simulation of the J shape damaged PDL were conducted on four different sides of the tooth, buccal, lingual, mesial, and distal sides referring in Figure 53. This approach accounts for the possibility of periodontal diseases affecting various aspects of the tooth.

The color scheme in model represents enamel (blue), dentin (green), and J shape damaged PDL (orange). To enhance the realism of the damaged PDL simulation, reduced PDL Young's moduli were implemented in FEA models, specifically using values of 0.005 MPa, 0.01MPa. Additionally, a model with a healthy PDL modulus of 0.1 MPa was included for comparative analysis with the reduced modulus models.
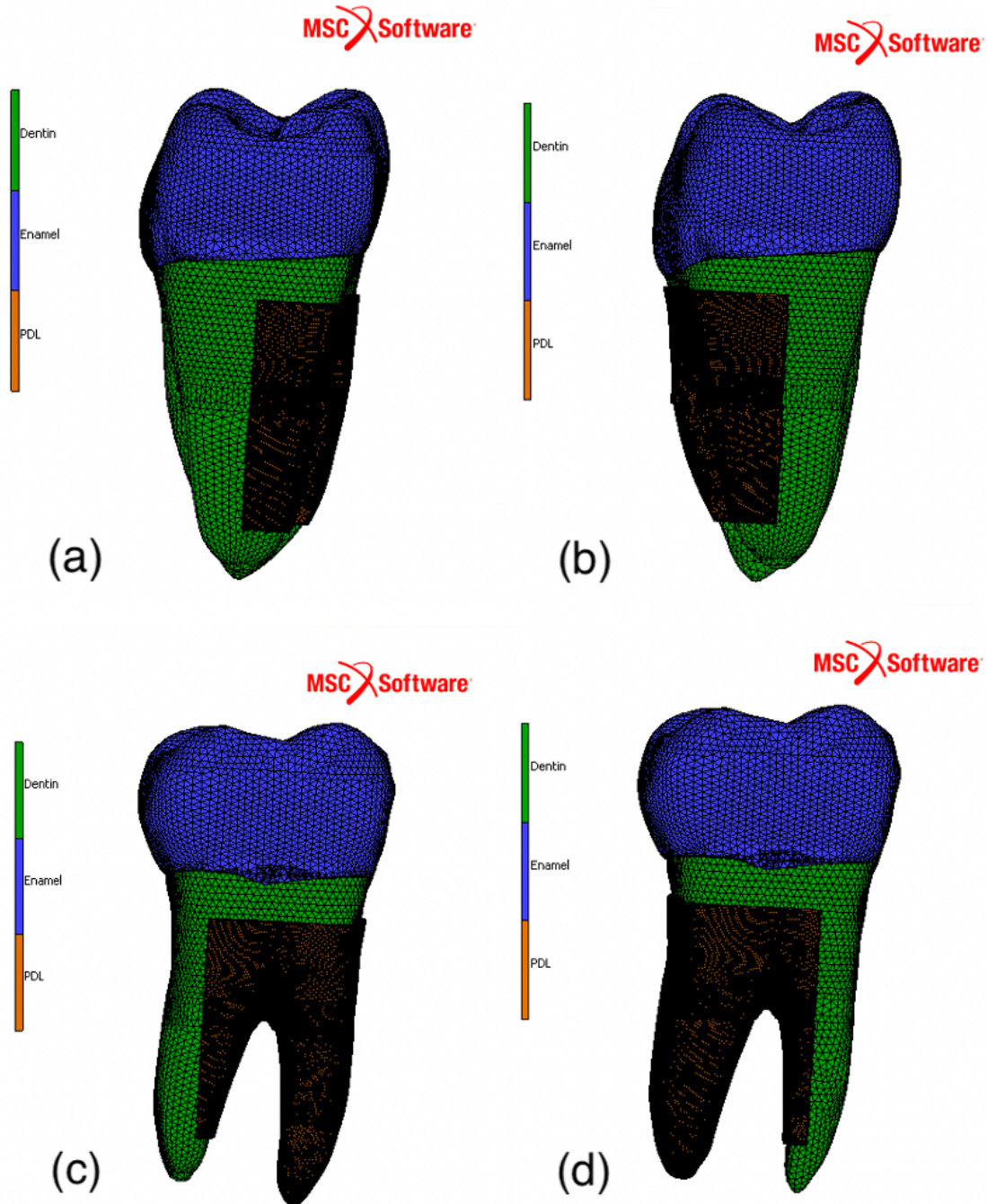
Figure 53: Pictures of intact mandibular second molar with four different J shape damaged PDL on each side of the tooth. (a) J shape damaged PDL on buccal side of the mandibular second molar. (b) J shape damaged PDL on the lingual side of the same tooth. (c) J shape damaged PDL on the distal side of the same tooth. (d) J shape damaged PDL on the mesial side of the same tooth.
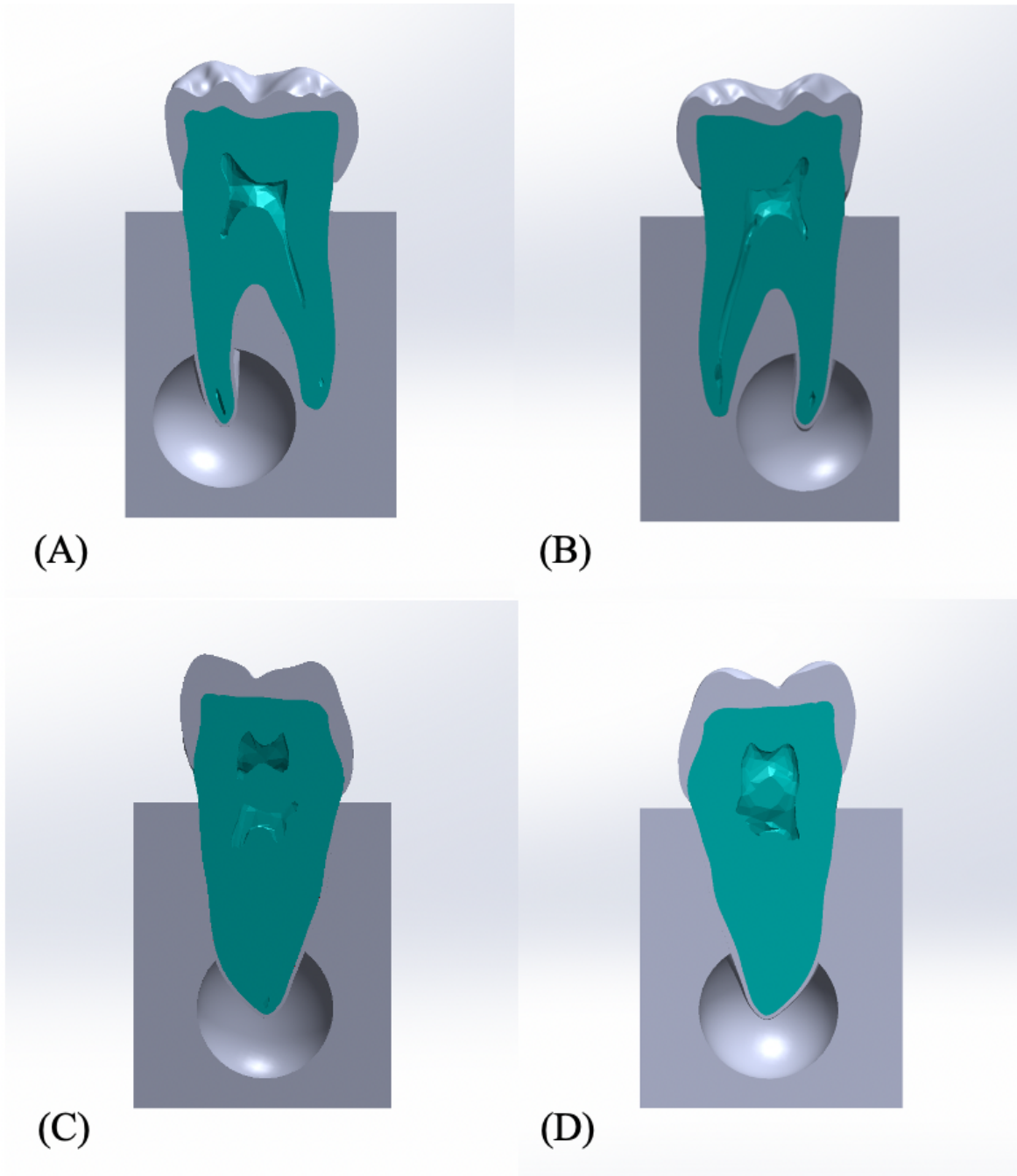
Figure 54: (A) Buccal view of PDL lesion (B) Lingual view of PDL lesion (C) Distal view of PDL lesion (D) Mesial view of PDL lesion.

The identical intact mandibular second molar CAD model served as the basis for replicating the periodontal lesion condition illustrated in Figure 51 and Figure 52. In this scenario, a spherical empty infection space was introduced at the distal side of the molar's apex. To achieve

this, a partial volume was subtracted from the original bone, creating the desired empty space beneath the root's apex. Figure 54 (A) provides a buccal side intersection view of the CAD model, revealing the PDL lesion on the left side (distal side). On the other hand, the Figure 54 (B) shows the opposite lingual side of the CAD model. Further insights into the PDL lesion are presented in Figure 54 (C) and Figure 54 (D) offering distal and mesial side views. The size of the PDL lesion was determined based on X-ray images in Figure 51 and CBCT scan in Figure 52.

Due to uncertainties regarding the previous endodontic treatment procedure, this study did not model damage to the enamel, dentin, and root canal. Nevertheless, material properties reflecting damaged enamel and dentin were proposed and tested in FEA simulations to align with the clinical condition resulting from prior endodontic treatment. Different percentages of the elastic modulus of healthy enamel and dentin were employed for testing. Additionally, the material property of PDL underwent testing with a lower modulus than that of healthy PDL. In the FEA software, an additional touching contact interaction was defined between the dentin and bone to account for the presence of the PDL lesion.

Following the PDL lesion diagnosis, the patient underwent endodontic retreatment, leading to subsequent CBCT and the QPD performed eight months post-treatment. Figure 55 Illustrates the CBCT results after treatment, allowing for a comparison with the pre-treatment CBCT result in Figure 52. The CBCT outcomes confirmed complete recovery of the PDL lesion around the apex. Subsequently, the QPD test conducted on this tooth after the CBCT. The results of the QPD after treatment are elaborated upon in the results section. To simulate the post-treatment tooth in FEA, an intact molar with a healthy, intact PDL and bone was utilized, omitting the spherical shaped empty chamber soured the apex. Various moduli for enamel, dentin and PDL were tested to accurately simulate the tooth condition following endodontic retreatment.
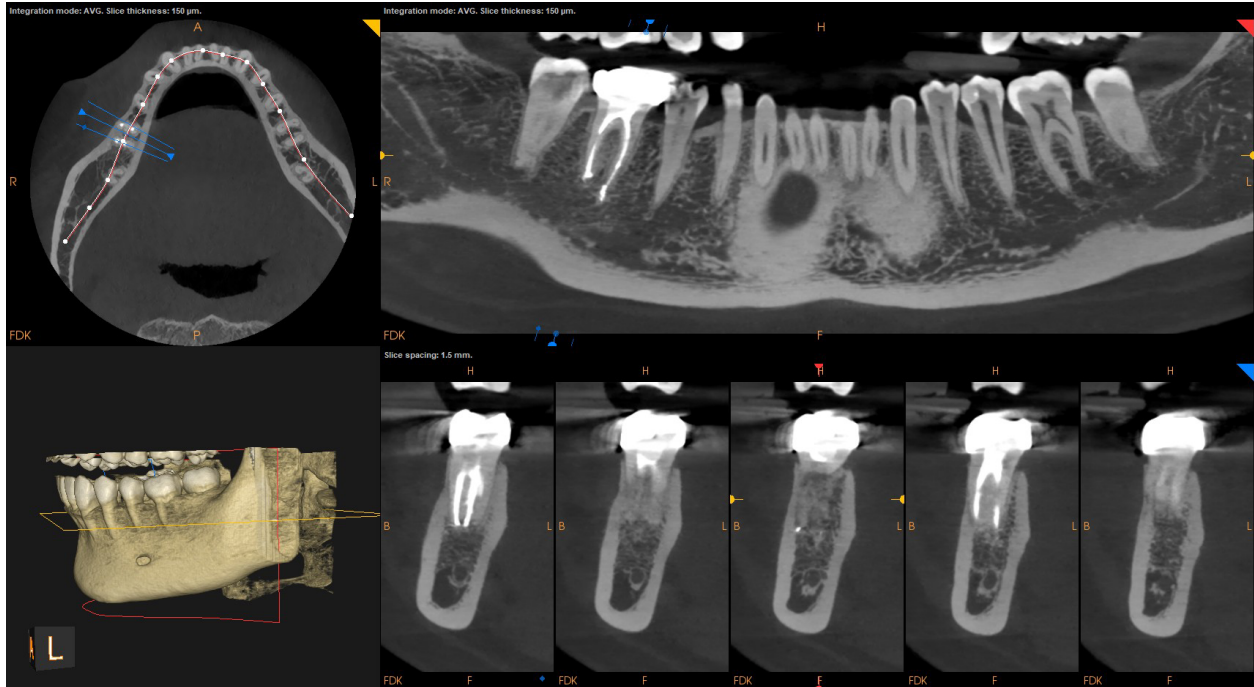
Figure 55: CBCT on the same molar tooth after treatment.

Results and Discussion

Figure 56 depicts the result of force versus time outcomes for a J shape damaged PDL with PDL modulus of 0.1 MPa, assuming the residual PDL remains undamaged. The black curve signifies the resultant force when the J shape damaged PDL is on distal side, while the yellow curve represents the result for the mesial side. The blue curve represents the result when the J shape damaged PDL is on buccal side and the red curve represents the result when the J shape damaged PDL is on lingual side.

Notably, when J shape damaged PDL is situated on the buccal and lingual sides, a slight bump appears on the peak slope during the descent, and the overall runtime is prolonged compared to scenarios where the damaged PDL is on the mesial and signal sides. Moreover, the amplitude of the blue and red curves is lower than that of the black and yellow curves. This. Disparity is attributed to the absence of damming resistance to dissipate forces due to the missing PDL. Given that the percussion direction is oriented in buccal-lingual direction, the J shape damaged PDL

induces a micro-gap defect between the dentin and bone, resulting in the absence of PDL and increased tooth mobility under percussion loading. This increased mobility leads to more pronounces oscillations when the damage is on the buccal and lingual sides. The force lacks damping resistance due to the absent of PDL, contributing to the observed differences in amplitude and runtime.
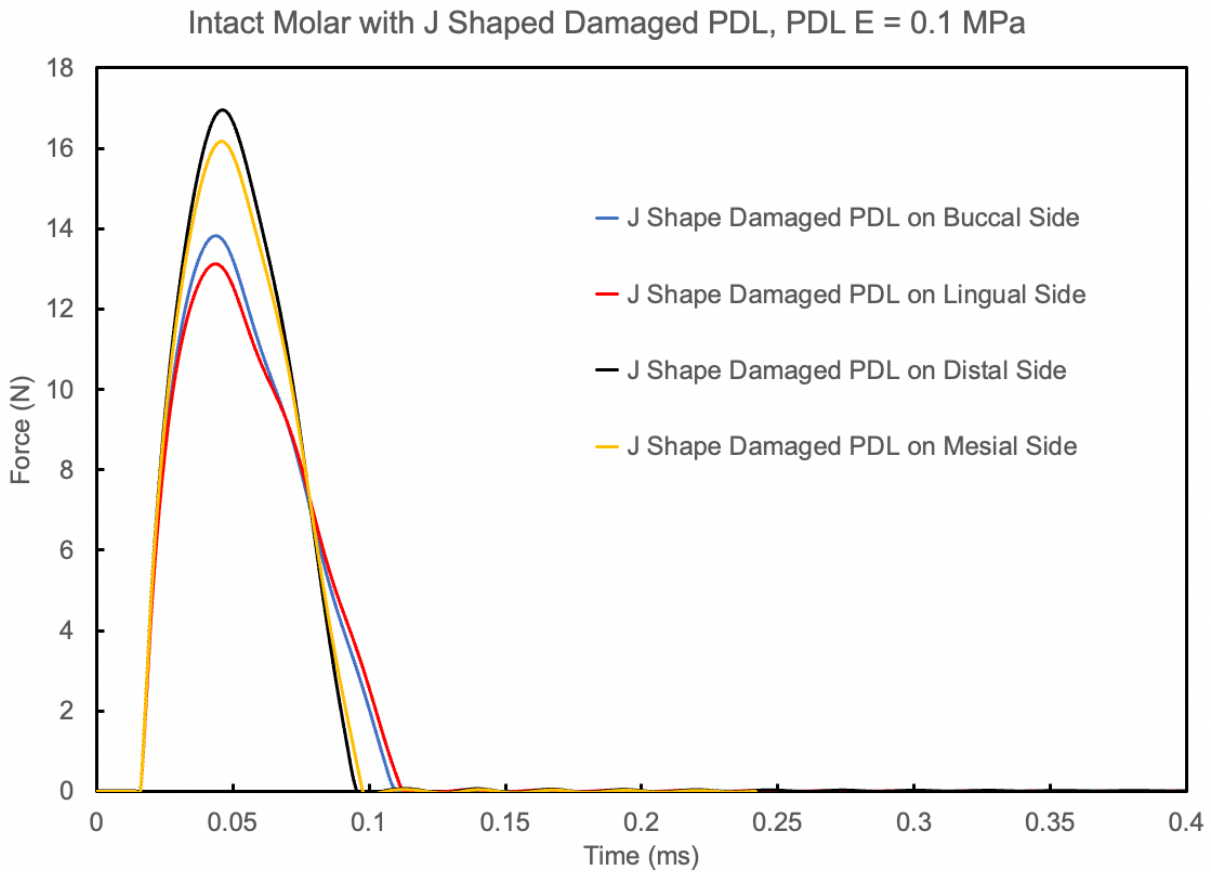
Figure 56: Force vs time for the J shape damaged PDL with PDL modulus of 0.1 MPa.

The force peaks in Figure 56 exhibit a characteristic single bell-shaped curve, reminiscent of intact teeth without microgap defects. However, this shape inadequately represents micro-gap defects, suggesting that the remaining PDL modulus of 0.1 MPa is too high. When a J shape damaged PDL is present, it is plausible that the remaining PDL also incurs damage. Therefore, reducing the remaining PDL modulus is essential to accurately simulate damaged PDL conditions.
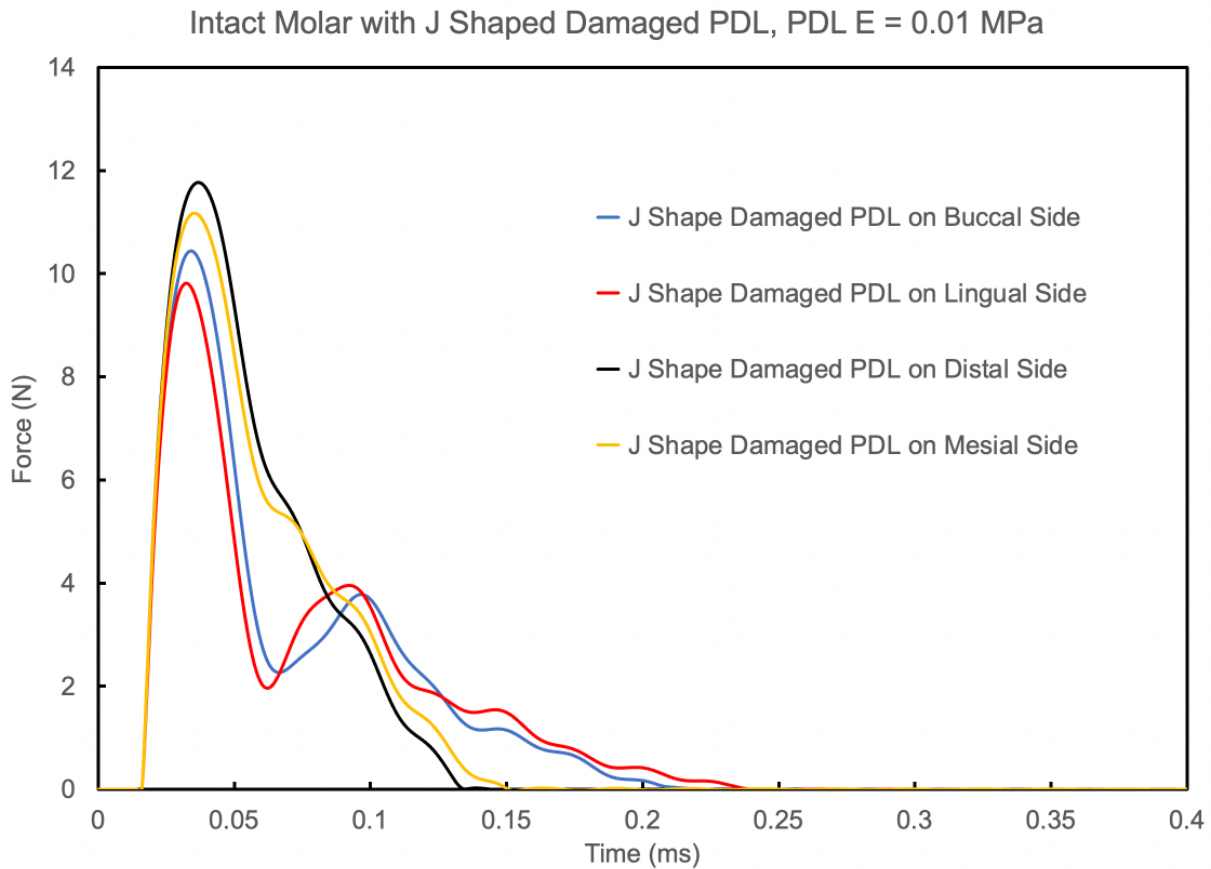
Figure 57: Force vs time for J shape damaged PDL with modulus of 0.01 MPa.

The plot above illustrates the result of force versus time for J shape damaged PDL with modulus of 0.01 MPa, simulating damage to the remaining PDL. The blue curve signifies the resultant force when the J shape damaged PDL is on the buccal side and the red curve represents the J shape damaged PDL is on lingual side. The black curve illustrates the resultant force when the damaged PDL is on the distal side, while the yellow curve represents the resultant force when the J shape damaged PDL is on the mesial side.

When the J shaped damaged PDL is on buccal and lingual sides, the blue and red curves exhibit two peaks. In contrast, the black and yellow curve do not display an obvious second peak when the J shape damaged PDL is on the distal and mesial side. In addition, the second peak on all curves when PDL modulus is 0.01 MPa, are more pronounced than the previous results obtained

with a PDL modulus is 0.1 MPa. This heightened prominence is attribute to the reduced PDL modulus, which renders the PDL less stiff in these models, leading to increased energy dissipation and the creation of high frequency peaks due to oscillation. Consistent with prior findings, the second peak is more pronounced when the J shaped damage PDL is on the buccal and lingual sides, aligning with the percussion loading direction in the buccal lingual orientation.
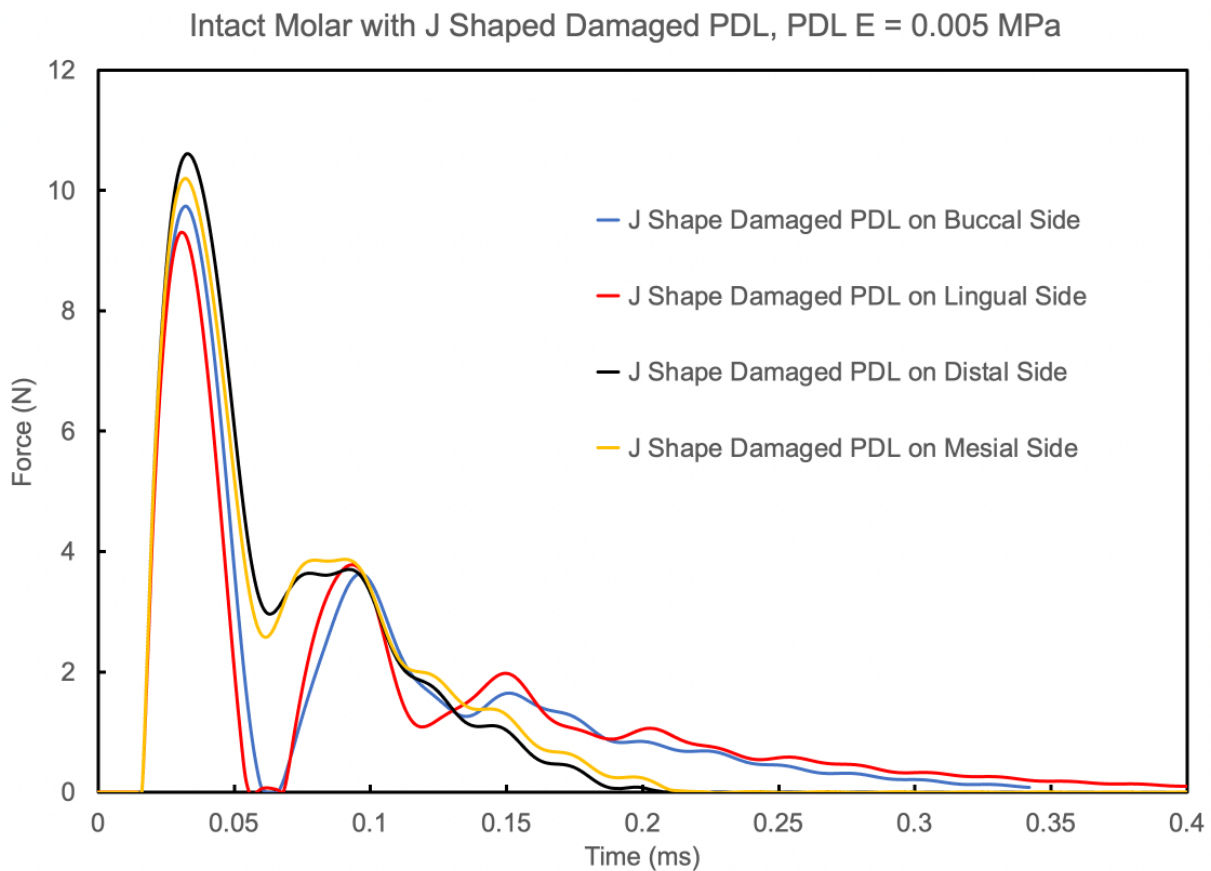
Figure 58: Force vs time for J shape damaged PDL with modulus of 0.005 MPa.

The presented plot above displays the result of force versus time for J shape damaged PDL with modulus of 0.005 MPa. The blue curve illustrates the resultant force when the J shape damaged PDL is on the buccal side and the red curve represents the resultant force for the lingual side. The black curve denotes the resultant force when the damaged PDL is on the distal side, and

lastly the yellow curve represents the resultant force when the J shape damaged PDL is on the mesial side.

All four curves exhibit multiple high-frequency peaks, regardless of the location of the J shape damaged PDL when the PDL modulus is 0.005 MPa. This phenomenon is attributed to the lower modulus in the PDL is this model compared to the previous one. The reduced stiffness of PDL leads to increased oscillations, resulting in a greater number of peaks. Furthermore, notable distinctions were observed that the second peak of the blue and red curves (buccal and lingual sides) are further delayed compared to the blue and orange curve (mesial and distal sides), and the blue and red curves have distinct first peaks. When the buccal or lingual J shape damaged PDL is present, there is less PDL on the buccal or lingual to dissipate the energy from the percussion loading, causing the second peak to occur at a later time. In addition, the total time duration of the red curve (J shaped damaged PDL on lingual) is even further delayed compared to the blue curve second peak (J shaped damaged PDL on buccal). This is influenced by the percussion location being on the buccal side of the tooth. When the J shape damaged PDL is on the lingual side, the PDL on the opposite side of the percussion loading is missing, resulting in reduced energy dissipation capabilities and a delayed total time duration.

Figure 59 illustrates the normalized energy return as a function of time. The goal is comparing FEA results with clinical data to achieve a matching plot shape. The green dashed line represents clinical QPD data, derived from the force response during the QPD test were picking up by force sensor in percussion rod. The QPD test comprises four taps, each generating a distinct curve. The results of these taps generally overlap. The clinical QPD result as shown in Figure 59, displays two peaks, the first being tall and wide, while the second peak is shallower in comparison. The total time duration of the QPD test is approximately 0.2 ms, indicating a relatively brief

duration compared to results from previous chapters involving vertical and oblique cracks in the same tooth. This suggests that the tooth damage is less severe, likely existing solely as a PDL lesion at the tooth apex.

Mandibular Second Molar with PDL Lesion
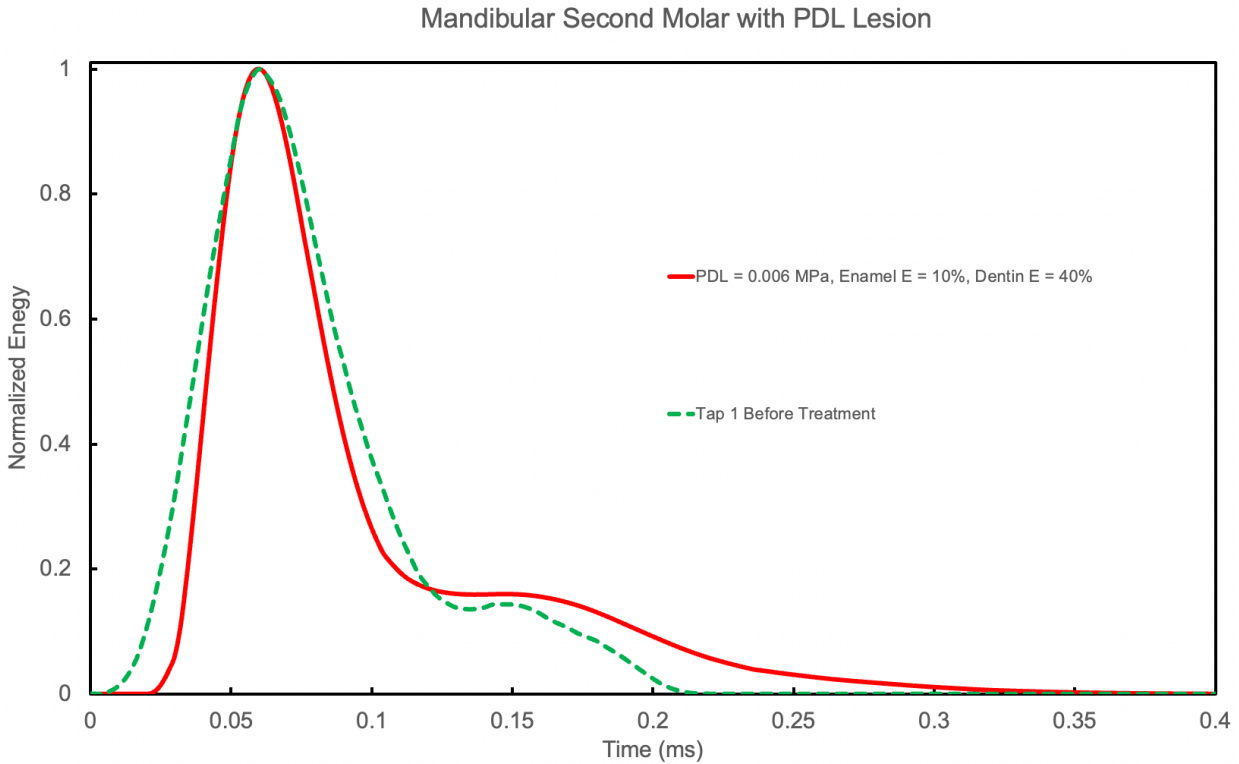
Figure 59: Normalized energy return vs time for PDL lesion at apex before treatment.

Following FEA simulations with various PDL moduli, the results are plotted and analyzed in Figure 59 for comparison with clinical data. The red solid line represents the FEA result, utilizing a PDL modulus of 0.006 MPa, 10% modulus of healthy enamel (8410 MPa) for enamel, and 40% modulus of healthy dentin (5880 MPa) for dentin. In comparison to the green dashed line representing QPD clinical results, the FEA features closely match fit. The red curve of FEA result also exhibits the same shape with two peaks, mirroring the clinical result's peak valley and width. The second peak's amplitude on the FEA result is also similar to the clinical data. While the total time duration is longer in the FEA results compared to clinical data, the overall match between the

FEA and clinical data is evident in terms of curve shape, number of peaks, peak amplitudes, and peak widths. This substantiates FEA's capability to simulate the QPD tests on PDL lesions in molar teeth, with the QPD proving effective in clinically detecting PDL lesions.
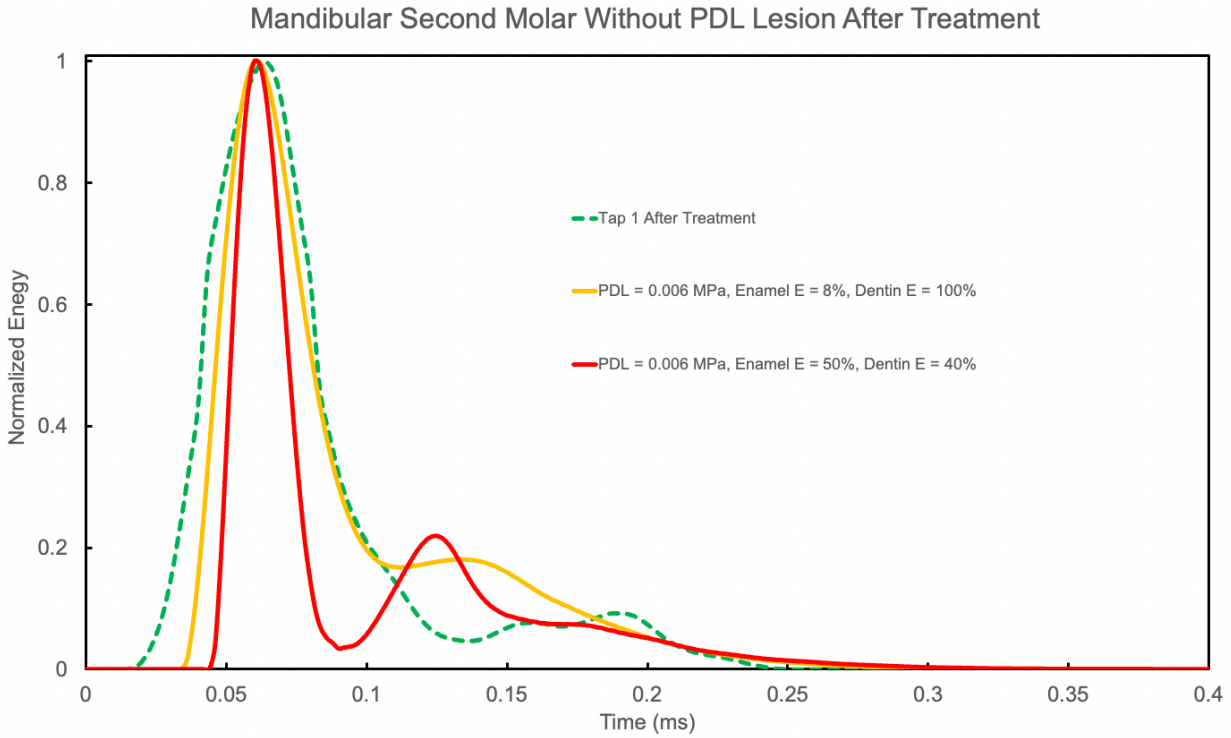
Figure 60: Normalized Energy return vs time for the same Molar without lesion after treatment.

After the endodontic retreatment and the placement of a new crown, another QPD test was conducted on the same molar. The result of this post-treatment analysis is given in Figure 60. In Figure 60, the clinical QPD data are depicted as a dashed green curve, revealing a single high amplitude first peak followed by additional high frequency smaller peaks. To align with the clinical results, various material properties were tested in simulated FEA models. The yellow curve represents the FEA result utilizing a PDL modulus of 0.006 MPa, enamel modulus at 8% of intact enamel (6728 MPa) and dentin modulus at intact dentin (14700 MPa). The yellow curve closely matches the clinical result, with a first peak width similar to the green curve and a total time duration close to 0.25 milliseconds. However, the second peak frequency and amplitude did not

align perfectly with the clinical result. The red curve signifies the FEA result with the same PDL modulus as the yellow curve (0.006 MPa), enamel modulus at 50% (42050 MPa), and dentin modulus at 40% of intact dentin (5880 MPa). While the red curve aligns well with the clinical result in terms of peak shape and number of peaks, the additional peaks are high frequency but not as pronounced as in the clinical data. Furthermore, the first peak width is narrower compared to the clinical result. Numerous material property settings were explored in FEA simulations, attempting to closely match the high frequency additional peaks observed clinically. However, no exact match was achieved. There is suspicion that undiscovered micro gap defects, such as micro cracks introduced during the endodontic retreatment (known as root crack), might be present within the tooth.

Conclusion

In conclusion, the QPD proves effective in detecting micro gap defects like J shape damaged PDL and PDL lesions. The force vs. time curve tends to exhibit a distinctive pattern which a first high amplitude peak followed by high frequency multiple little peaks in the presence of J shape damaged PDL. The modulus of the remaining PDL plays a crucial role, with lower PDL modulus resulting in distinct peaks and higher frequency.

FEA models, when tested with the QPD on PDL lesion conditions, successfully validate the clinical QPD results. The FEA results align well with clinical findings for molars with PDL lesion conditions, considering peak amplitude, number of peaks, peak valley depth, time duration, and peak width. Various material properties were explored during FEA simulations to closely match clinical results, confirming that enamel and dentin modulus should be reduced to accurately simulate the post-endodontic treatment conditions of enamel and dentin.

CONCLUSION

In this study, we utilized FEA models to simulate the QPD tests on various tooth types, each implementing different MGD types and conditions. These conditions included scenarios such as single rooted bicuspid with different oblique crack lengths, single rooted bicuspid with different vertical crack lengths, double rooted molar with different vertical crack gap spaces, vertical cracked molar with damaged PDL, 3D printed replica molar with fatigue cracks, molar with apical root crack, molar with J shape damaged PDL and molar with PDL lesion. The primary goal was to employ FEA to gain insights into the complexities of the QPD corresponding to MGD types and their conditions.

The FEA simulation results unveiled three consistent observations in line with previous experimental QPD findings. First, intact teeth displayed a single bell shaped curve on the force versus time plot, a pattern consistent across FEA models of both intact bicuspid and molar. Second, the presence of MGDs resulted in multiple peaks on the force versus time plots. This pattern was evident in all FEA models featuring oblique cracks, vertical cracks, apical root cracks and damaged PDL, contrasting with the single bell shaped curved observed in intact teeth. FEA results for teeth with MGDs are also validated with clinical data of corresponding MGDs in natural teeth. Lastly, as increase in the number of peaks was associated with longer cracks or larger crack gap spaces, a trend supported by the FEA results presented in the first two Chapters.

In addition to these consistent findings, the study uncovered three new observations. First, peaks on the force versus time plots were found to be correlated with crack oscillation and crack closure. FEA models facilitated an in-depth examination of the tooth's response to percussion loading with tools like contact status contour and relative acceleration between crack surfaces, indicating that peaks were formed due to oscillation of cracks. In addition, more severe MGDs led

to increased crack oscillation and a greater number of peaks. Second, it was demonstrated that the QPD could effectively detect MGDs in root regions, including apical root cracks and damaged PDL. Current dentistry faces limitation in diagnosing MGDs in invisible root regions, but the FEA models successfully simulated distinct peak trends consistent with the clinical QPD results, indicating the presence of apical root cracks which is illustrated in Chapter 5. Additionally, the simulation of PDL lesions showed shallower second peak, aligning with the clinical QPD results. Lastly, FEA results demonstrated the capability to predict the behaviors of MGDs in teeth under the QPD test.

FUTURE WORK

As this dissertation lays the groundwork for understanding the QPD response in diverse dental defect scenarios through FEA simulations with various MGDs in single rooted bicuspid and double rooted molar, several ideas open up for future exploration and research. The integration of advanced techniques holds the potential to improve the practical applicability of the QPD in dental diagnostics. The following points are key directions for future work.

1. Expansion of MGD Types

   To broaden the scope of the research, future work should incorporate additional defect types beyond those explored in this current dissertation. For example, investigating the impact of loose crowns, commonly associated with microleakage, on the QPD responses would contribute valuable insights. Expansion in MGD types aim to provide a comprehensive understanding of how the QPD performs across a spectrum of dental issues.

2. Integration of Artificial Intelligence (AI)

   The idea of utilizing AI into QPD results analysis represents a promising method for enhancing diagnostic capabilities. Future work could focus on using AI to predict MGD conditions, such as defect types and crack conditions based on the real-world QPD results. Training AI modles using extensive datasets derived from current FEA simulations would provide dentists with predictive tools, enabling accurate diagnoses during clinical QPD tests, so proper treatments could be given.

3. Validation using 3D Printed Replica Teeth

   Given the challenges of obtaining in vivo research samples with specific defect types, future research should emphasize on the validation of FEA simulation results using 3D printed replica teeth with corresponding MGDs. Printing replica teeth with MGDs discussed in this

dissertation would help to validate the present FEA results. This validation process would confirm the reliability and credibility of FEA simulations across various MGDs, strengthening their practical relevance in dental diagnostics.

4. Optimization of Replica Tooth Printing

Continuing improvements in 3D printing techniques can be pursed to optimize the 3D printed replica teeth. Using better printer which capable of higher resolution would enable finer details, such as minimizing notch gap space. The refinement contributes to the crafting replica teeth would closely emulate actual tooth condition, further validating FEA simulation result accurately.

In conclusion, the future work above not only extends the current dissertation's findings, but also further validating and proving the capabilities of the QPD diagnostics in clinical settings, gaining more insights about the QPD results corresponding to unknown defects in tooth.

REFERENCES

[1]   Blausen, "Medical gallery of Blausen Medical 2014," WikiJournal of Medicine, vol. 1, no. 2, 2014, doi: 10.15347/wjm/2014.010.

[2]   C. G. Sheets, D. L. Stewart, J. C. Wu, and J. C. Earthman, "An in vitro comparison of quantitative percussion diagnostics with a standard technique for determining the presence of cracks in natural teeth," Journal of Prosthetic Dentistry, vol. 112, no. 2, pp. 267–275, 2014, doi: 10.1016/j.prosdent.2014.02.020.

[3]   D. Bs. Glenn A. van As, "Evaluation of Enamel and Dentinal Cracks Using Methylene Blue Dye and the Operating Microscope," Inside Dentistry, vol. 3, no. 7, 2007.

[4]   S. H. Lee, J. J. Lee, H. J. Chung, J. T. Park, and H. J. Kim, "Dental optical coherence tomography: new potential diagnostic system for cracked-tooth syndrome," Surgical and Radiologic Anatomy, vol. 38, no. 1, pp. 49–54, Jan. 2016, doi: 10.1007/s00276-015-1514-8.

[5]   C. G. Sheets, [Co-, D. Hui, V. Bajaj, J. C. Earthman, and [Biomedical, "Quantitative Percussion Diagnostics and Bone Density Analysis of the Implant-Bone Interface in a Pre- and Postmortem Human Subject HHS Public Access," 2013.

[6]   L. R. VanSchoiack, J. C. Wu, C. G. Sheets, and J. C. Earthman, "Effect of bone density on the damping behavior of dental implants: An in vitro method," Materials Science and Engineering C, vol. 26, no. 8, pp. 1307–1311, Sep. 2006, doi: 10.1016/j.msec.2005.08.019.

[7]   "Sheets et al 17 JPD + Cover".

[8]   A. Dinh, C. G. Sheets, and J. C. Earthman, "Analysis of percussion response of dental implants: An in vitro study," Materials Science and Engineering C, vol. 33, no. 5, pp. 2657–2663, Jul. 2013, doi: 10.1016/j.msec.2013.02.033.

[9]   P. Shabeel, "Diagnosis and Treatment Planning," Slide Share.

[10]   D. Roylance, "Finite Element Analysis," 2001. [Online]. Available: http://ocw.mit.edu/courses/materials-science-and-engineering/3-11-mechanics-of-materials-fall-1999/modules/

[11]   M. Seo, W. Shon, W. Lee, H.-M. Yoo, B.-H. Cho, and S.-H. Baek, "FINITE ELEMENT ANALYSIS OF MAXILLARY CENTRAL INCISORS RESTORED WITH VARIOUS POST-AND-CORE APPLICATIONS," 2009.

[12]   R. E. Campos et al., "In vitro study of fracture load and fracture pattern of ceramic crowns: A finite element and fractography analysis," Journal of Prosthodontics, vol. 20, no. 6, pp. 447–455, Aug. 2011, doi: 10.1111/j.1532-849X.2011.00744.x.

[13]   I. A. Sioustis et al., "Finite element analysis of mandibular anterior teeth with healthy, but reduced periodontium," Applied Sciences (Switzerland), vol. 11, no. 9, May 2021, doi: 10.3390/app11093824.

[14]   A. Mapar, N. Taheri-Nassaj, J. Shen, O. Komari, C. G. Sheets, and J. C. Earthman, "Finite Element Study of Periodontal Ligament Properties for a Maxillary Central Incisor and a Mandibular Second Molar Under Percussion Conditions," J Med Biol Eng, Oct. 2022, doi: 10.1007/s40846-022-00724-5.

[15]   M. Poppe, C. Bourauel, and A. Jäger, "Determination of the elasticity parameters of the human periodontal ligament and the location of the center of resistance of single-rooted teeth. A study of autopsy specimens and their conversion into finite element models," Journal of Orofacial Orthopedics, vol. 63, no. 5, pp. 358–370, Sep. 2002, doi: 10.1007/s00056-002-0067-8.

[16] D. W. Richardson, "Dental materials—properties," J Prosthet Dent, vol. 63, no. 4, p. 492, Apr. 1990, doi: 10.1016/0022-3913(90)90250-G.

[17] T. S. Fill, J. P. Carey, R. W. Toogood, and P. W. Major, "Experimentally determined mechanical properties of, and models for, the periodontal ligament: Critical review of current literature," Journal of Dental Biomechanics, vol. 2, no. 1. SAGE Publications Inc., pp. 1–10, 2011. doi: 10.4061/2011/312980.

[18] E. M. Rivera and R. E. Walton, "Longitudinal tooth fractures: findings that contribute to complex endodontic diagnoses."

[19] J. H. S. Simon, D. D. S. Dudley, H. Glick, D. D. S. Alfred, and L. Frank, "The Relationship of Endodontic-Periodontic Lesions by."

[20] A. N. Natali, Ed., Dental Biomechanics. CRC Press, 2003. doi: 10.1201/9780203514849.

[21] J. Meaud and G. M. Hulbert, "Dependence of the dynamic properties of Voigt and Reuss composites on the Poisson's ratios and bulk loss factors of the constituent materials," J Compos Mater, vol. 47, no. 26, pp. 3237–3247, Dec. 2013, doi: 10.1177/0021998312463456.

[22] William Joseph O'Brien, Dental Materials and Their Selection, 2nd ed. Quintessence Publishing Company, 1997.

[23] "[ASHBY99] - Materials Selection In Mechanical Design 2Ed".

[24] M. Poppe, C. Bourauel, and A. Jäger, "Determination of the Elasticity Parameters of the Human Periodontal Ligament and the Location of the Center of Resistance of Single-rooted Teeth," Journal of Orofacial Orthopedics/Fortschritte der Kieferorthop die, vol. 63, no. 5, pp. 358–370, Sep. 2002, doi: 10.1007/s00056-002-0067-8.

[25] E. B. Lubisich, T. J. Hilton, and J. Ferracane, "Cracked teeth: A review of the literature," Journal of Esthetic and Restorative Dentistry, vol. 22, no. 3, pp. 158–167, Jun. 2010, doi: 10.1111/j.1708-8240.2010.00330.x.

[26] S. T. Talim and K. S. Gohil, "Management of coronal fractures of permanent posterior teeth."

[27] C. G. Sheets, D. L. Stewart, J. C. Wu, and J. C. Earthman, "An in vitro comparison of quantitative percussion diagnostics with a standard technique for determining the presence of cracks in natural teeth," Journal of Prosthetic Dentistry, vol. 112, no. 2, pp. 267–275, 2014, doi: 10.1016/j.prosdent.2014.02.020.

[28] A. Dinh, C. G. Sheets, and J. C. Earthman, "Analysis of percussion response of dental implants: An in vitro study," Materials Science and Engineering: C, vol. 33, no. 5, pp. 2657–2663, Jul. 2013, doi: 10.1016/j.msec.2013.02.033.

[29] C. G. Sheets, J. C. Wu, S. Rashad, M. Phelan, and J. C. Earthman, "In vivo study of the effectiveness of quantitative percussion diagnostics as an indicator of the level of the structural pathology of teeth," J Prosthet Dent, vol. 116, no. 2, pp. 191-199.e1, Aug. 2016, doi: 10.1016/j.prosdent.2016.01.015.

[30] I. Dumbryte, L. Linkeviciene, T. Linkevicius, and M. Malinauskas, "Enamel microcracks in terms of orthodontic treatment: A novel method for their detection and evaluation," Dent Mater J, vol. 36, no. 4, pp. 438–446, 2017, doi: 10.4012/dmj.2016-264.

[31] M. Matsushita-Tokugawa et al., "Detection of dentinal microcracks using infrared thermography," J Endod, vol. 39, no. 1, pp. 88–91, Jan. 2013, doi: 10.1016/j.joen.2012.06.033.

[32] A. Mapar, N. Taheri-Nassaj, J. Shen, O. Komari, C. G. Sheets, and J. C. Earthman, "Finite Element Study of Periodontal Ligament Properties for a Maxillary Central Incisor and a

Mandibular Second Molar Under Percussion Conditions," J Med Biol Eng, vol. 42, no. 5, pp. 681–691, Oct. 2022, doi: 10.1007/s40846-022-00724-5.

[33] L. R. VanSchoiack, J. C. Wu, C. G. Sheets, and J. C. Earthman, "Effect of bone density on the damping behavior of dental implants: An in vitro method," Materials Science and Engineering: C, vol. 26, no. 8, pp. 1307–1311, Sep. 2006, doi: 10.1016/j.msec.2005.08.019.

[34] W. Goldsmith and J. T. Frasier, "Impact: The Theory and Physical Behavior of Colliding Solids," J Appl Mech, vol. 28, no. 4, pp. 639–639, Dec. 1961, doi: 10.1115/1.3641808.

[35] E. B. Lubisich, T. J. Hilton, and J. Ferracane, "Cracked teeth: A review of the literature," Journal of Esthetic and Restorative Dentistry, vol. 22, no. 3, pp. 158–167, Jun. 2010, doi: 10.1111/j.1708-8240.2010.00330.x.

[36] Rickne C. Scheid and Julian B. Woelfel, Woelfel's Dental Anatomy: Its Relevance to Dentistry, 7th ed. Maryland: Lippincott Williams & Wilkins, 2007.

[37] K. Yoshino, K. Ito, M. Kuroda, and N. Sugihara, "Prevalence of vertical root fracture as the reason for tooth extraction in dental clinics," Clin Oral Investig, vol. 19, no. 6, pp. 1405–1409, Nov. 2015, doi: 10.1007/s00784-014-1357-4.

[38] T. Sugaya et al., "Comparison of fracture sites and post lengths in longitudinal root fractures," J Endod, vol. 41, no. 2, pp. 159–163, Feb. 2015, doi: 10.1016/j.joen.2014.09.017.

[39] D. Arola and R. K. Reprogel, "Effects of aging on the mechanical behavior of human dentin," Biomaterials, vol. 26, no. 18, pp. 4051–4061, Jun. 2005, doi: 10.1016/j.biomaterials.2004.10.029.

[40] H. Chai and A. Tamse, "The Effect of Isthmus on Vertical Root Fracture in Endodontically Treated Teeth," J Endod, vol. 41, no. 9, pp. 1515–1519, Sep. 2015, doi: 10.1016/j.joen.2015.04.003.

[41] D. Clark and J. A. Khademi, "Case Studies in Modern Molar Endodontic Access and Directed Dentin Conservation," Dental Clinics of North America, vol. 54, no. 2. pp. 275–289, Apr. 2010. doi: 10.1016/j.cden.2010.01.003.

[42] S. Patel, B. Bhuva, and R. Bose, "Present status and future directions: vertical root fractures in root filled teeth," International Endodontic Journal, vol. 55, no. S3. John Wiley and Sons Inc, pp. 804–826, May 01, 2022. doi: 10.1111/iej.13737.

[43] J. C. Pinto et al., "Influence of voxel size on dentinal microcrack detection by micro-CT after root canal preparation," Braz Oral Res, vol. 35, pp. 1–8, 2021, doi: 10.1590/1807-3107BOR-2021.VOL35.0074.

[44] A. R. PradeepKumar, H. Shemesh, S. Jothilatha, R. Vijayabharathi, S. Jayalakshmi, and A. Kishen, "Diagnosis of Vertical Root Fractures in Restored Endodontically Treated Teeth: A Time-dependent Retrospective Cohort Study," J Endod, vol. 42, no. 8, pp. 1175–1180, Aug. 2016, doi: 10.1016/j.joen.2016.04.012.

[45] L. Karygianni, M. Krengel, M. Winter, S. Stampf, and K. T. Wrbas, "Comparative assessment of the incidence of vertical root fractures between conventional versus surgical endodontic retreatment," Clin Oral Investig, vol. 18, no. 8, pp. 2015–2021, Nov. 2014, doi: 10.1007/s00784-013-1182-1.

[46] S. Cohen, L. H. Berman, L. Blanco, L. Bakland, and J. S. Kim, "A Demographic Analysis of Vertical Root Fractures," J Endod, vol. 32, no. 12, pp. 1160–1163, 2006, doi: 10.1016/j.joen.2006.07.008.

[47] H. Chai and A. Tamse, "Vertical Root Fracture in Buccal Roots of Bifurcated Maxillary Premolars from Condensation of Gutta-percha," J Endod, vol. 44, no. 7, pp. 1159–1163, Jul. 2018, doi: 10.1016/j.joen.2018.03.017.

[48] A. Gao, D. Cao, and Z. Lin, "Diagnosis of cracked teeth using cone-beam computed tomography: Literature review and clinical experience," Dentomaxillofacial Radiology, vol. 50, no. 5. British Institute of Radiology, 2021. doi: 10.1259/dmfr.20200407.

[49] J. H. S. Simon, D. D. S. Dudley, H. Glick, D. D. S. Alfred, and L. Frank, "The Relationship of Endodontic-Periodontic Lesions by."

[50] Yi-Chu Wu, Brooke Blicher, Rebekah Pryles, and Jarshen Lin, "Understanding Periodontal-Endodontic Infections," Inside Dentristry, vol. 14, no. 4, Apr. 2018.